# Paleomagnetism and paleogeographic reconstructions of the North China Craton in the Late Carboniferous - Early Permian and the South China Craton in the Late Ediacaran - Early Cambrian

by

Ekaterina Kozmina

A thesis submitted in partial fulfillment of the requirements for the degree of

Doctor of Philosophy
in
Geophysics

Department of Physics
University of Alberta

**Abstract**

The robustness of paleogeographic reconstructions of the North China Craton (NCC) and South China Craton (SCC) in the Ediacaran - Paleozoic is greatly affected by a small number of high-reliability paleomagnetic poles. Reduced reliability of available paleomagnetic data is attributed to weak magnetizations of the sediments, absence of up-to-date stepwise demagnetization analysis, field tests, and rock-magnetics studies.

This study reports the first reliable paleomagnetic poles from the Late Carboniferous - Early Permian sediments of the NCC and the Ediacaran - Early Cambrian sediments of the SCC. The new paleomagnetic poles meet all seven paleomagnetic reliability criteria and their ages are supported by our own zircon data. We sampled fine-grained sandstones, limestones, and red stones (only from the SCC). Our stepwise demagnetization analysis shows the presence of two magnetic components in the samples and the great circle directed towards the high-temperature component direction. The fold and polarity tests indicate the primary character of the high-temperature component.

Our new paleomagnetic poles for the NCC show that the craton moved from 26.9°N ± 5.2° to 32.5°N ± 7.1° during the Late Carboniferous - Early Permian (after the application of the flattening factor of 0.7). These are higher latitudes than it was considered before. We show that the width of the Paleo Asian Ocean between the NCC and Inner Mongolian arc accretionary complexes was ~860 km in the Late Carboniferous - Early Permian, which was three times narrower than the previous studies suggested.

We completed the new paleomagnetic analysis of the Early Cambrian and Early and Late Ediacaran directions from the SCC. It should be noted that the Late Ediacaran and Early Cambrian

of the SCC have never been studied paleomagnetically. In this study, the Early and Late Ediacaran paleomagnetic poles yielded a paleolatitude around 15°N that resembles the paleolatitudes obtained from the coeval paleomagnetic poles for Australia. This favors a hypothesis that the SCC could be attached or in close proximity to Australia in the Neoproterozoic or at least be at a similar paleolatitude. However, it contradicts the paleogeography reconstructions that placed the SCC at ~33°S. The Early Cambrian paleolatitude was 8.2°N ± 3.6° which corresponds to the Middle Cambrian paleolatitudes from the other studies. At the same time, the affinity between the new Early Cambrian pole and Late Permian - Early Triassic poles for the SCC does not rule out a possibility of overprinting. Future additional measurements will enable us to provide a more statistically reliable interpretation. However, we were able to show that high temperature components for Ediacaran and Cambrian are all distributed along the great circle with the Euler pole at the sampling locality. Such scatter was already reported for Laurentia, Australia, and Siberia. There are a few different hypotheses that explain such a scatter and adding our new reliable South China paleomagnetic data sets will be a step forward in constraining these hypotheses.

**Preface**

Chapter 2 is going to be submitted as a manuscript around a thesis defense date (E. Kozmina, V. A. Kravchinsky, S. T. Johnston, M. Domeier, and R. Zhang, "Paleomagnetism of the Late Carboniferous and Early Permian sediments and paleogeographic reconstructions of the North China Craton"). This study was funded by the Natural Sciences and Engineering Research Council of Canada (NSERC grant RGPIN-2019-04780 of V.A.K.). I participated in the fieldwork in China in 2018 to collect the Late Carboniferous and Early Permian rock samples from the North China Craton for laboratory measurements. This fieldwork was a part of an ongoing collaboration between the University of Alberta and Northwest University (Xi'an, China) led by V. A. Kravchinsky and R. Zhang. The fieldwork was partially supported by the Mitacs Globalink Research Award - China Scholarship Council in 2018 (grant FR27478). V. A. Kravchinsky, S. T. Johnston and M. Domeier (University of Oslo, Norway) guided and assisted me during the fieldwork. L. P. Koukhar (University of Alberta) and Minghao Ma (Northwest University, Xi'an, China) assisted me in rock sampling during this fieldwork. L. P. Koukhar, also, guided and assisted me in the laboratory measurements of remanence magnetization at the Paleomagnetic Laboratory of the University of Alberta. I conducted thermal and alternating field demagnetizations and Isothermal Remanence Magnetization (IRM) measurements. Minghao Ma conducted the temperature-dependent magnetic susceptibility (k-T) measurements at the Paleomagnetic Laboratory of the Northwest University (Xi'an, China). The U-Pb zircon measurements were performed by A. DuFrane at the ICPMS Laboratory of the University of Alberta. Data analysis of zircon results was performed by me. I performed data processing, analysis, and interpretation of paleomagnetic results under the guidance of V. A. Kravchinsky. V. A. Kravchinsky, S. T. Johnston, and M. Domeier contributed significantly to the data interpretation and writing of this Chapter.

Chapter 3 is a basis of a future paper as “Paleomagnetism of the Ediacaran - Early Cambrian sediments for the South China Craton”. Since the obtained data revealed a need to conduct additional measurements, this paper will be completed and submitted after the thesis defense. This Chapter is based on a project that is, also, a continuation of the collaboration between the University of Alberta and Northwest University (Xi’an, China) led by V. A. Kravchinsky and R. Zhang. Samples were collected in China (2017 and 2018) by V. A. Kravchinsky, M. Domeier, L. P. Koukhar, M. Ma, X. Zhang, R. Zhang, and X. Cheng (Northwest University, Xi’an, China). Thermal and alternating field demagnetizations were carried out by Ben Lysak and L. P. Koukhar at the Paleomagnetic Laboratory of the University of Alberta. Rock magnetic studies were performed by Ben Lysak with the guidance of M. Domeier at the University of Oslo. Ben Lysak processed, analyzed, and interpreted the first set of data. I performed data processing and analysis of the previous set of data and additional data combined, and interpretation of paleomagnetic results with assistance from V. A. Kravchinsky. V. A. Kravchinsky and S. T. Johnston contributed significantly to the data interpretation and writing of this Chapter.

**Acknowledgments**

This Doctorate Program became one of the toughest but fateful periods in my life followed by constant learning of new things and persistent hard work with ups and downs. All of this would not have happened without people leading, helping, and supporting me on this path. First, I would like to thank my supervisors Dr. V. A. Kravchinsky and Dr. S. T. Johnston for their teaching, and patience, for not giving up on me during the difficult times, for their strict but fair comments, and for their push to gain better performance in research. I would like to thank L. P. Koukhar for her constant help in our Paleomagnetic Laboratory with equipment and measuring samples, and for invaluable support throughout the Program. I would like to express my gratitude and thanks to Dr. M. Domeier for his guidance in paleomagnetic analysis and during fieldwork in China, and for his significant contribution to the interpretation of the paleomagnetic results. I would also like to thank Dr. R. Zhang for his organization and assistance in the fieldwork in China and his help with the geological papers from China. I would like to thank Minghao Ma for his assistance with sampling in the fieldwork, k-T measurements, and for providing geological papers from China required for my research. I would like to thank Greg Popowich for his great help in installing the lab equipment (VFTB) used for the rock-magnetic studies. I thank Benjamin Lysak for his tremendous help in courses during my study and for being a supportive and thoughtful colleague.

Special thanks to my friends: Olga Fomenko, Aleksandra Stoinova, Anna Morozova, Tagir Farkhutdinov, and Anna and Daniel Tendera for constant help and 24/7 support, and encouragement in difficult times. I would like to thank Andrey Tretiakov and Hennadii Yerzhakov for their help in my study and research.

Lastly, I thank my brother, M. Kozmin, for his belief in me and his wise advice that helped me to keep going on this way and complete this Program.

# Contents

**List of tables**

**List of Figures**

**Abbreviations**

AGZ - Altai - Gobi Zone

APWP - Apparent polar wander paths

COB - Central Orogenic Belt

CRM – Chemical Remanent Magnetization

DRM – Detrital Remanence Magnetization

GAD - Geocentric Axial Dipole

HTC - High Temperature Component

ICPMS - Mass Spectrometry that uses an Inductively Coupled Plasma

IRM - Isothermal Remanence Measurements

LTC - Low Temperature Component

MOB - Mongol-Okhotsk Belt

MSWD - Mean Square of Weighted Deviates

NCC - North China Craton

NRM - Natural Remanent Magnetization

NUT - Nuhetdavaa-Uliastai fore/backarc terrane

PAO - Paleo Asian Ocean

PCA - Principal Component Analysis

pDRM – Post-Detrital Remanent Magnetization

SCC - South China Craton

SQUID - Superconducting Quantum Interference Device

TRM - Thermal Remanent Magnetization

VGP - Virtual Geomagnetic Pole

VFTB - Variable Field Translation Balance

# Chapter 1: Introduction

## 1.1. Basic principles of paleomagnetic method

Plate tectonic reconstructions are essential for studying complex geodynamic processes of Earth. Plate tectonic reconstruction of continents or paleogeographic reconstruction is a restoration of a position of a tectonic unit in the geological past using paleomagnetic, geophysical, geological, geochemical, and geochronological data.

Two main concepts of paleomagnetism are applied in plate tectonic reconstructions. The first concept addresses the property of ferromagnetic minerals composing rocks to record the ambient magnetic field during the rock formation and maintain it over time. A phenomenon of recording the magnetic field is related to the magnetic moment in ferromagnetic particles tending to be aligned with the orientation of the geomagnetic field during rock crystallization or sediment accumulation. In other words, a rock acquires magnetization which is called natural remanent magnetization (NRM) at the time of formation. NRM ($Am^{-1}$) can be defined as a sum of all interacted magnetic moments in a sample carried by electrons per a volume of mineral lattice in the following formula (1.1):

$$NRM = \frac{\sum Mi}{volume} \qquad (1.1)$$

where Mi is a magnetic moment ($Am^2$) of individual magnetic dipoles with a pair of bipolar charges (Butler, 1992). A phenomenon of the magnetic moment is related to a precession of the electron around its rotation axis (Butler, 1992).

NRM is a superimposed vector of the acquired primary and secondary magnetizations by a rock acquired over time. The primary NRM component contains information about the geomagnetic field during a rock formation while the secondary NRM component is acquired under exposure to

the exothermic and chemical processes or to the acting geomagnetic field rock is subjected to throughout its geological history (Butler, 1992).

There exist a number of NRM types depending on an acquisition mechanism. NRM acquired during the cooling of igneous rocks in the temperature range of the Curie to blocking temperatures is called thermal remanent magnetization (TRM) (Butler, 1992). During a cooling process magnetic moments of ferromagnetic grains align to the ambient geomagnetic field. However, magnetic moments may experience resistance to this alignment because of the shape and size of the magnetic grains (Butler, 1992).

Magnetic grains can be constituted of either an elementary single domain or an assemblage of single domains. The magnetization within one domain is uniform and characterized by a certain orientation. In assemblage, every single domain is separated by walls. The magnetization within a domain is temperature-dependent, i.e., at the Curie temperature, the magnetization tends to zero. The orientation of the magnetization can be changed in the temperature range between the Curie and blocking temperatures. Below the blocking temperature, the intensity of the magnetization increases but the orientation of the magnetization remains stable (Butler, 1992).

The blocking temperature is related to the relaxation time required for magnetization to decay after the removal of the magnetic field. The relaxation time depends on a ratio between blocking and thermal energies. The blocking energy defines an energy barrier within a domain after which the orientation of magnetization can be changed. In the temperature range between Curie and blocking temperatures the relaxation time for magnetization is extremely short (about first orders of microseconds depending on the grain size), but below the blocking temperature, the relaxation time rapidly increases and becomes comparable to geological time (Butler, 1992).

Since TRM can be removed only at temperatures higher than the Curie temperatures, it can endure exposure to the external chemical and detrital processes and maintain the recorded orientation of the magnetic field over geological time (Butler, 1992). That is why igneous rocks are assumed to have the most reliable NRM and they are the main target for paleomagnetologists.

The Curie temperatures of magnetic minerals vary depending on the type of magnetic mineral composing a rock, i.e., in the case of magnetite or hematite the Curie temperature is ~580 or ~690°C respectively. The Curie temperature of magnetic minerals consisting of iron oxides with a fraction of, for example, titanium such as titanomagnetite or titanomagnetite varies around 450 - 525°C (Butler, 1992).

With regard to sedimentary rocks there are two most common types of NRM: 1) detrital remanence magnetization (DRM) and 2) chemical remanence magnetization (CRM). DRM is a resulting magnetization within a sediment matrix composed of already magnetized grains. During settling down on a sediment surface magnetic moment of grains tends to become aligned along the ambient geomagnetic field (Butler, 1992). However, it has been established that elongated grains tend to settle down in accordance with their longest axis parallel to a sediment surface (King, 1955). This produces inclination errors resulting in the lowering of DRM inclinations in sedimentary rocks relative to the inclination of the geomagnetic field. The relationship between the shallowed inclination of DRM and geomagnetic field inclination is defined by the following equation (1.2):

$$\tan(I_{observed}) = f \tan(I_{field}) \qquad (1.2)$$

where $I_{observed}$ is the observed inclination (°) in measured rock samples, $I_{field}$ is the inclination (°) of the applied field, $f$ is an empirical coefficient experimentally estimated to be around 0.55 which further will be called as a flattening factor (King, 1955).

It has been found that grains can be rotated or displaced within a sediment matrix after deposition. This occurs either due to a bottom relief or bottom water flow or bioturbation that disrupts the acquired orientation of the preexisting geomagnetic field. Rotated magnetic grains become realigned along the current geomagnetic field and acquire post-detrital remanence magnetization (pDRM) (Butler, 1992).

It is worth noting that the typical range of NRM for TRM and DRM is about 1 and 0.001 A/m which supports the advantage of the igneous rock with much higher magnetization values over sedimentary rocks for paleomagnetic studies (Butler, 1992).

CRM attributes to the alteration in the mineral composition of rock under external chemical conditions caused by weathering or contact of sedimentary rocks with magmatic or fluid activity (Butler, 1992). The chemical reaction changes the mineral composition of rock that follows by changes in crystal mineral structure and grain volumes. Alternation in grain volumes involves changes in blocking energies and destroys the primary magnetization orientations. Newly obtained directions and intensities of magnetic minerals overprint the preexisting orientation of the geomagnetic field (Butler, 1992).

The primary NRM can be isolated using stepwise thermal or alternating field demagnetization (Butler, 1992). Methods employ a gradual exposure of a rock sample to heating in a special furnace (for example, up to 690°C) or to the alternating magnetic field (for example, up to 100 mT) and subsequent measurement of the magnetization in a magnetometer. The magnetometer we use in our laboratory for magnetization measurement is a horizontal 2G Enterprises DC-SQUID cryogenic magnetometer (model 755-1.65). A basic operating principle of such a magnetometer is based on the detection of changes in the magnetic flux in pick-up coils of the SQUID system at

ultra-low temperatures induced by a magnetic moment carried by the magnetic grains of a rock sample (Butler, 1992).

Stepwise demagnetization procedure provides a set of magnetization vectors described by a coercivity force and directions with a corresponding blocking temperature which can be plotted on a so-called Zijderveld vector diagram (Fig. 1.1a) and an equal-area projection (Fig. 1.1b) (Butler, 1992).

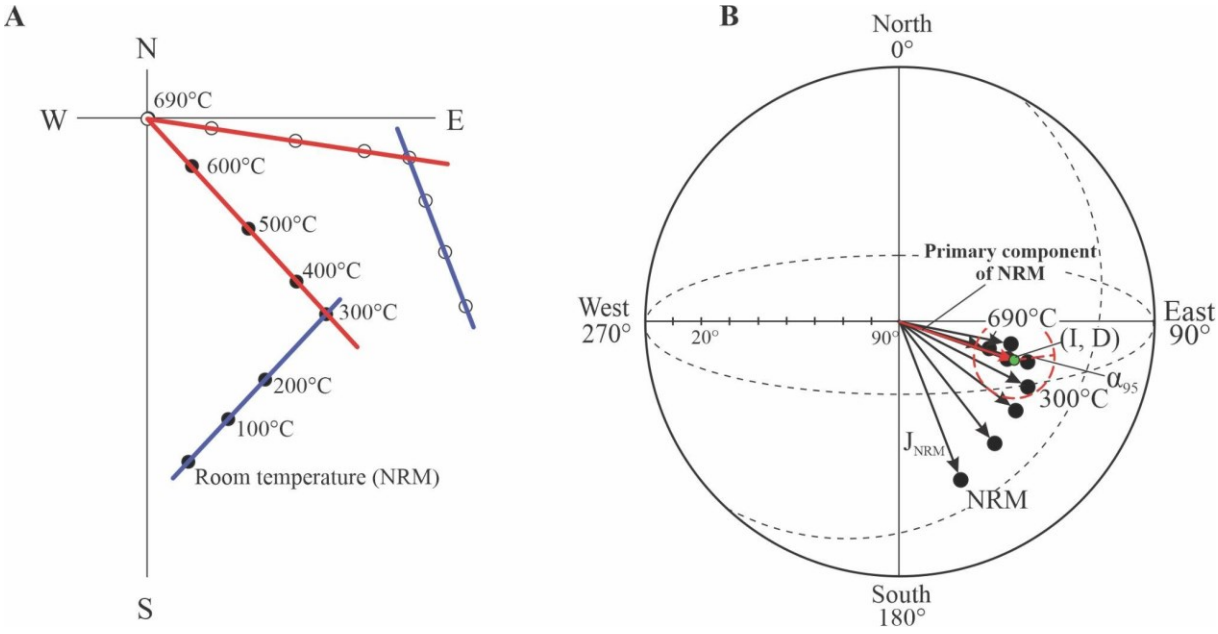


Figure 1.1. Simplified schemes of Zijderveld vector diagram (A) and equal-area projection (B). Blue line – secondary component of NRM, red line – the primary component of NRM; $\alpha_{95}$ - the radius of 95% cone confidence for a direction distribution; green circle – imaginary mean direction for the primary component of magnetization; I - inclination, D - declination; $J_{NRM}$ - the vector of the natural remanent magnetization (NRM).

A Zijderveld vector diagram is a plot of vector components of measured magnetization projected on orthogonal vertical and horizontal planes for each temperature step. The direction of the magnetization vector can be defined by inclination *(I)* and declination *(D)* in degrees (Fig. 1.1b). The mean direction of magnetization vectors on a sphere can be computed as a weighted mean

using the approach described in Fisher (1953) (Fig. 1.1b). The red dashed circle in Figure 1.1b corresponds to the 95% confidence interval of magnetization vector distribution.

The second major concept in paleomagnetism is that the Earth's magnetic field is approximated as a geocentric axial dipole (GAD) that is stable in time. The GAD represents a time-averaged geomagnetic field. An axis of the GAD coincides with the axis of the Earth's rotation. The geomagnetic field can be described by the following parameters: the total magnetic vector *(H)*, inclination *(I)*, and declination *(D)* (Kravchinsky, 2015). Within the GAD hypothesis, all these parameters are assumed to be stable over time for each point on the Earth's sphere (Fig. 1.2).

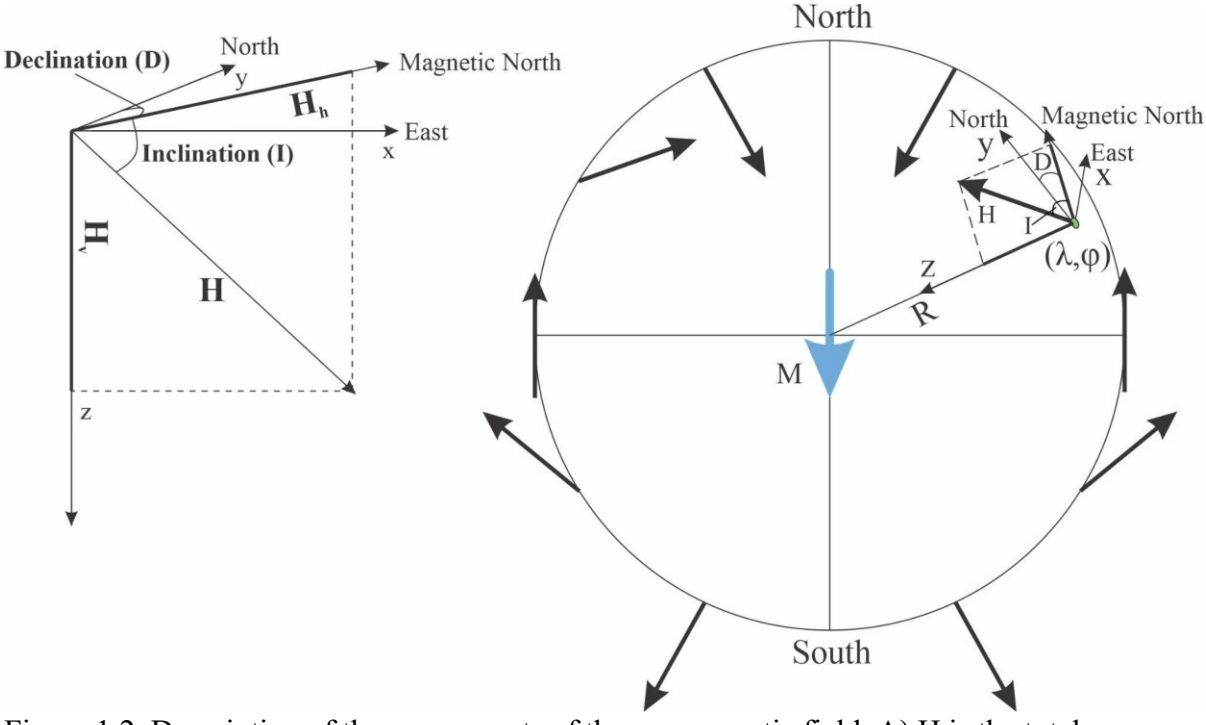


Figure 1.2. Description of the components of the geomagnetic field. A) H is the total geomagnetic vector; I is the vertical angle between the horizontal and total components of the geomagnetic field, D is the azimuthal angle between the horizontal component and geographic north; $H_v = H_{sin}(I)$ and $H_h = H_{cos}(I)$ are the vertical and horizontal components of the geomagnetic field; x - the direction pointing towards geographic north, y - the direction pointing towards the east, and z - the vertical direction. B) M (blue arrow) - the direction of the magnetic moment of the geomagnetic field, R - Earth's radius, λ – latitude, φ – longitude, black arrows - the direction of the total vector of the geomagnetic field depending on latitudes, green circle - imaginary observation site on the sphere. The figures are modified after Butler (1992).

The horizontal component of the magnetic field *($H_h$)* that is a projection of the total geomagnetic vector on the horizontal plane can be expressed by a formula (1.3):

$$H_h = \frac{M\cos\lambda}{R^3} \quad (1.3)$$

where M – the moment of the geomagnetic dipole field ($Am^2$), λ – latitude (°), R – Earth's radius (km). The vertical component of the geomagnetic field *($H_v$)* that is a projection of the total geomagnetic vector on the horizontal plane can be expressed by a formula (1.4):

$$H_v = \frac{2M\sin\lambda}{R^3} \quad (1.4)$$

There is a relation between latitude and inclination which can be computed from the mean direction of magnetization vectors using the following formula (1.5):

$$tan\ I = \frac{Hv}{Hh} = \frac{2sin\ \lambda}{cos\lambda} = 2tan\ (\lambda) \quad (1.5)$$

Here it should be noted that the inclination shallowing, that was discussed above, can be attributed not only to the sedimentation process but also to the non-GAD components, in particular, to the axial octupolar component of the geomagnetic field (Tauxe and Kent, 2004). The distribution of observed directions is hypothetically assumed to be nearly circularly symmetric, however, the non-GAD components of the geomagnetic field may cause the north-south elongation of distribution at lower latitudes. This is a principal difference between the inclination shallowing caused by the non-GAD component and inclination shallowing resulting from the sedimentary inclination error which, in contrast, is characterized by the west-east elongation of distribution of directions (Tauxe and Kent, 2004). Tauxe and Kent (2004) suggested an Elongation/Inclination method to find an optimal flattening factor. The major idea of this method implies the estimation of an elongation degree of observed directions and the finding of a flattening factor that converts the observed direction distribution from the elongated to a nearly circularly symmetric shape. However, this method requires a large dataset that includes more than 100 observed directions that is difficult to

implement in practice, especially for weakly magnetized rocks where a significant amount of samples can be analyzed only using the great circles.

A set of latitudes for a discrete-time range is used to reconstruct a path of a tectonic unit in the past. In paleomagnetism, a restoration of a path of a tectonic unit addresses not the actual movement of this unit but a path of an axis of the geomagnetic dipole (Fig. 1.3).

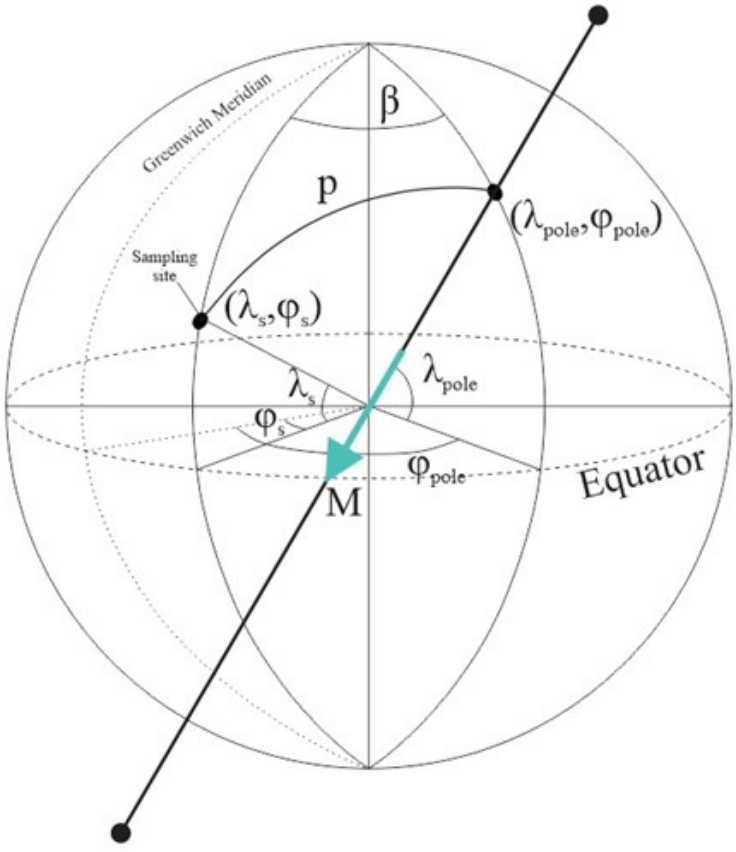


Figure 1.3. A geocentric axial dipole model with a description of the paleomagnetic pole's parameters derived from inclination and declination (adapted from Butler (1992)). M (blue arrow) - the direction of the magnetic moment of the geomagnetic field, p is the magnetic colatitude, β is the longitudinal difference between pole and site, λ is the latitude, and φ is the longitude for the sampling site (s) and pole.

In other words, paleomagnetism assumes that a tectonic unit is fixed to the axis of the geomagnetic dipole. And the wandered dipole axis can be traced in time using the position of the imaginary or

virtual geomagnetic pole (VGP). A position of VGP on the sphere can be computed using inclination and declination obtained from a mean direction of the primary component of NRM, and coordinates of a sampling site by the following formula for the spherical triangle (1.6) (Butler, 1992):

$$\lambda_{pole} = \sin^{-1} (\sin \lambda_s \cos p + \cos \lambda_s \sin \lambda_s \cos D) \quad (1.6)$$

where $\lambda_{pole}$ is a pole latitude, $\lambda_s$ is a latitude of a sampling site where a rock sample was collected, D is a declination of the mean direction, p is the magnetic colatitude determined in formula (1.7):

$$p = cot^{-1}(\frac{tanI}{2}) = tan^{-1}(\frac{2}{tanI}) \quad (1.7)$$

where I is the inclination of a mean direction of HTC.

A set of VGPs for a discrete-time range can be used to calculate an apparent polar wander path (APWP). APWP is usually a spline or running average interpolated between available poles that reflects the motion of a tectonic block for a certain geological interval (Fig. 1.4). Thus, APWP provides a quantitative estimation of a position of a tectonic block in the past, but it lacks information regarding longitudes. It was shown that reconstructing an absolution motion of a tectonic block requires an accurate continuous APWP (Wu and Kravchinsky, 2014).

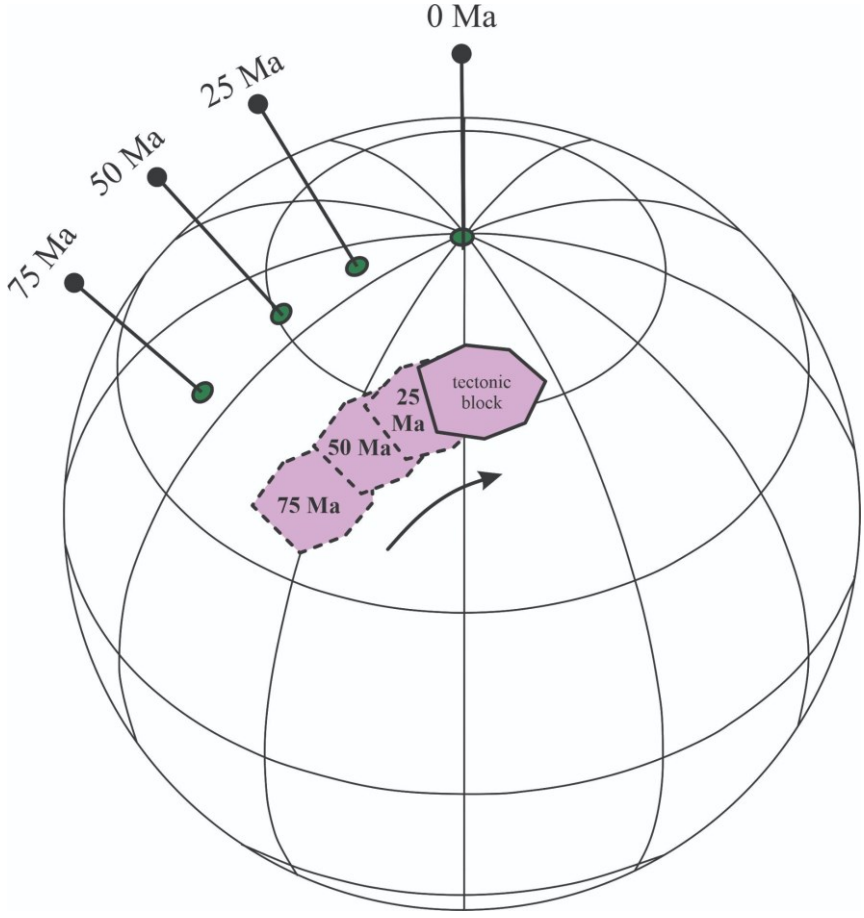


Figure 1.4. Simplified scheme of APWP and tectonic motion for the time range of 75 - 0 Ma. The Figure was modified after Butler (1992). The purple shape corresponds to a tectonic block moving during 75 - 0 Ma. The dashed outline of the tectonic block describes its position in the past. The black arrow shows the direction of motion of the tectonic block.

Therefore, new paleomagnetic data with a high reliability index is in high demand to improve the time resolution of available paleomagnetic datasets hence better constraint polarity intervals as well as to improve the accuracy of existing APWPs. This became one of the major motivations for this work in terms of the reconstruction of East Asia.

### 1.2. Thesis objectives

This thesis deals with paleomagnetic results and paleogeographic reconstructions of the North China Craton (NCC) in the Late Carboniferous - Early Permian and the South China Craton (SCC) in the Ediacaran - Early Cambrian. Paleogeographic reconstructions are usually based on

paleomagnetic studies, geological, geochemical, geochronological, paleontological, and tectonic mode analysis.

The main objective of Chapter 2 is to obtain the first reliable paleomagnetic poles for the NCC in the Late Carboniferous - Early Permian. One of the major tectonic events in Eastern Asia was the closure of the Paleo Asian Ocean (PAO) surrounded by Siberia, NCC, Tarim, and terranes of Inner Mongolia and Amuria. A number of recent studies suggested on the basis of geochronology and geochemistry that the final closure of PAO occurred sometime in the Late Paleozoic - Early Mesozoic (Chai et al., 2020; Lu et al., 2020, Xiao et al., 2018). However, the accurate timing and locality of closure are not known because of poor paleomagnetic data availability in the Late Paleozoic, especially in the Late Carboniferous - Early Permian (Huang et al., 2018). The Late Paleozoic framework of PAO is also not constrained. Our sampling target was sediments of different types in the center of the NCC, where folding took place in the Central Orogenic Belt separating the western and eastern parts of the NCC.

Chapter 3 is dedicated to paleomagnetism and paleoposition of the SCC in the Ediacaran - Early Cambrian. The tectonic evolution of Rodinia and its successor Gondwana is one of the central issues in the Neoproterozoic - Early Cambrian period (Cawood et al., 2018; Li et al., 2008). There exist great disagreements in reconstructions of Rodinia, Gondwana, and the tectonic setting drove a break-up of Rodinia and the formation of Gondwana in the Neoproterozoic - Early Cambrian period (Meert, 2014). The SCC is often not included in the Ediacaran - Cambrian reconstructions because of the absence of reliable or just any paleomagnetic data for these time intervals. Therefore, we sampled one of the best described and published sedimentary formations in the SCC where well-described biota and geochemical data were already used for building the global paleogeographic reconstructions (Li et al., 2019).

The interpretation of the global paleomagnetic data is, however, very complex for the Ediacaran and Cambrian because of ambiguity and poor time resolution of paleomagnetic data (Meert, 2019, Shatsillo et al., 2020). To explain the unusual scatter of paleomagnetic poles for Laurentia, Europe, Australia, and Siberia it has been proposed a number of different models. Meert et al. (2014) suggested that continents were subjected to unusually rapid plate motions. Kirschvink et al. (1997) and Evans (1998) suggested true polar wander. Meert and Tamrat (2004) suggested the influence of superplume interaction. Abrajevitch and Van der Voo (2010), Pavlov et al. (2018), and Shatsillo et al. (2020) suggested the co-existence of a dominant axial dipole field and a weaker equatorial dipole field. The main goal of Chapter 3 is to demonstrate the potential for success of the paleomagnetic method to obtain reliable paleomagnetic poles from the SCC that can be used for paleogeographic reconstructions. This data can be used to explain the paleomagnetic data scatter revealed in the Ediacaran - Early Cambrian deposits.

# Chapter 2: Paleomagnetism of the Late Carboniferous - Early Permian sediments and paleogeography reconstruction of the North China Craton

## 2.1. Introduction

One of the major events in the Late Paleozoic tectonic history of East Asia is the closure of the Paleo-Asian Ocean (PAO) involving the successive accretion of Siberia, North China Craton (NCC), Tarim, Inner Mongolia, Amuria, and adjacent arc accretionary complexes. In our study, Amuria is defined as a composite tectonic block that includes the Mongol-Okhotsk Belt (MOB) and adjacent accreted Precambrian terranes, passive continental margins, and Late Paleozoic - Mesozoic arc islands (Fig. 2.1). Inner Mongolia consists of the Hegenshan, Baolidao, Erdaojing, Ondor Sum accretionary complexes (Fig. 2.1).

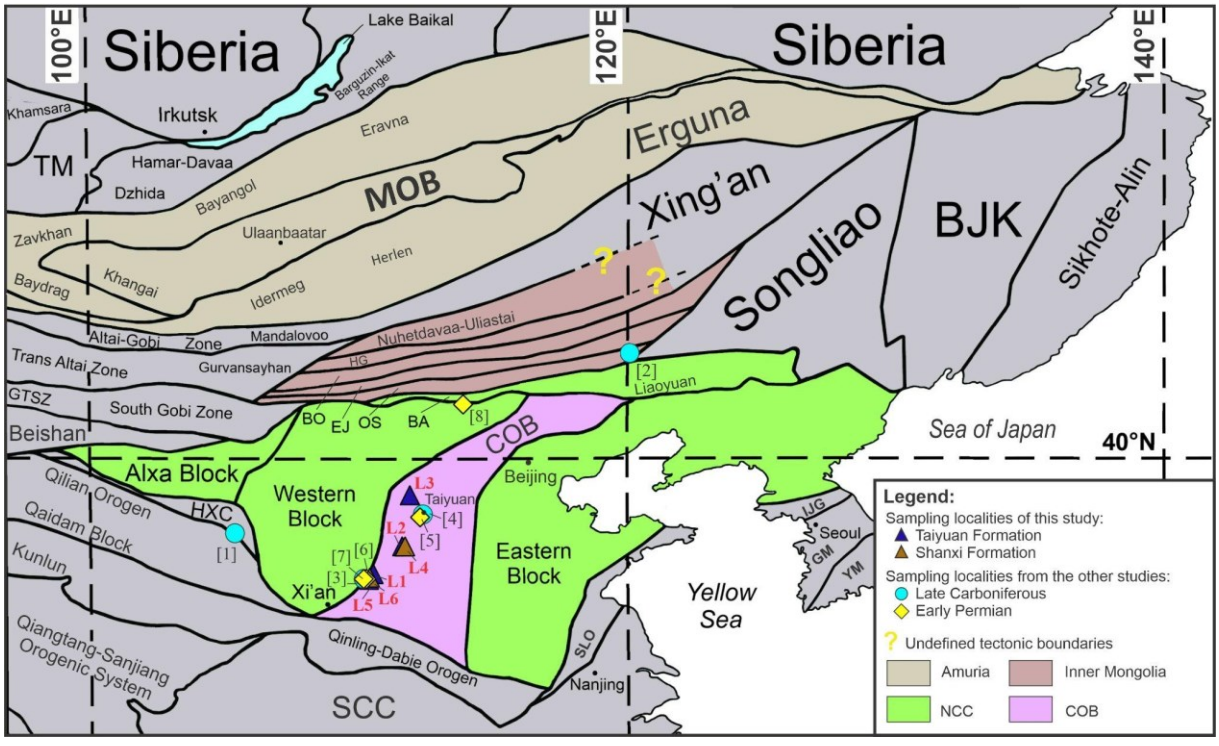


Figure 2.1. Simplified tectonic map of East Asia with sampling localities. Tectonic boundaries used for this map were borrowed and modified from Badarch et al. (2002), Dong and Santosh (2016), Guy et al. (2014), Han et al. (2012), Jiang et al. (2017), Mao et al. (2012), Pan et al. (2012), Şengör et al. (2018), Xiao et al. (2018), Zhao et al. (2005), Zhao et al. (2017). HG - Hegenshan Accretion Complex, BO - Baolidao Accretion Complex, EJ - Erdaojing Accretion Complex, OS -

Ondor Sum Accretion Complex, BA - Bainaimiao Arc Complex (Xiao et al., 2018); TM - Tuva-Mongolia Block (Jiang et al., 2017), BJK - BureyaJiamusi-Khanka (Han et al., 2012), COB - Central Orogenic Belt (Zhao et al., 2005), GTSZ - Gobi-Tian Shan Zone (Guy et al., 2014), HXC - Hexi Corridor Belt (Zhao et al., 2017), MOB - Mongol-Okhotsk Belt, SCB - South China Block. Sampling localities: blue triangles – Taiyuan Formation; brown triangles – Shanxi Formation, blue circles – previous Late Carboniferous paleomagnetic studies; yellow squares – previous Early Permian paleomagnetic studies. Previous studies: [1] – Huang et al. (2001), [2] – Zhao et al. (1990), [3] – Wu (1990), [4] – Lin et al. (1984), [5] – Embleton et al. (1996), [6] – Ma et al. (1993), [7] – Wu (1990), [8] – Zhang et al. (2018).

Numerous tectonic models have been suggested to describe the history of PAO closure (Chai et al., 2020; Lu et al., 2020, Şengör et al., 2018; Xiao et al., 2018, and reference therein). But the tectonic setting, location, and timing of the final PAO closure remain debatable. It is commonly accepted that the PAO consisted of multiple branches separated by a series of island arc terranes including the Erguna, Xing'an, Songliao Blocks, Amuria, and Inner Mongolian. All these tectonic units were welded to the northern margin of the NCC by prolonged subduction and closure of paleo ocean plates (Badarch et al., 2002; Chen et al., 2020; Fu et al., 2021; Ji et al., 2020; Lu et al., 2020; Xiao et al., 2018; and the references therein). Thus, the NCC takes a key position in paleogeographic reconstructions of PAO closure. Recent geochronological and geochemical studies suggest that the final closure of PAO occurred in the Late Paleozoic - Early Mesozoic (Chai et al., 2020; Lu et al., 2020, Xiao et al., 2018, and the references therein). Therefore, the main target for paleomagnetic studies of the tectonic units involved in the PAO closure is the Late Paleozoic strata. However, the Late Carboniferous - Early Permian sedimentary rocks of the NCC are characterized by a weak magnetic remanence which has made it difficult to obtain reliable paleomagnetic data (Embleton et al., 1996; Huang et al., 2001).

Paleogeographic reconstructions of PAO (Huang et al., 2018; Ren et al., 2020, 2021; Zhang et al., 2021b) assume that the NCC was located close to the equator at 10 - 15°N in the Late

Carboniferous - Early Permian based on a paleomagnetic pole from the Taiyuan limestones (Huang et al., 2001). This pole, however, is calculated from 11 samples and does not meet important criteria of paleomagnetic pole reliability (Meert et al., 2020; Van der Voo, 1990). The Early-Middle Permian paleoposition of the NCC is based on a paleomagnetic pole calculated from a mean of two poles corresponding to a large time interval (~283 – 266 Ma) (Zhang et al., 2018). In addition, the Early-Middle Permian pole in Zhang et al. (2018) was obtained from volcanic rocks sampled along the northern margin of the NCC. This margin was subjected to local tectonic rotations during the collision between the NCC and Inner Mongolia. Thus, there is no paleomagnetic pole of the required reliability index constraining the Early Permian paleolatitude of the NCC.

Therefore, there exists a need for reliable Late Carboniferous - Early Permian paleomagnetic data from the NCC. The main goal of our study is to obtain high reliability index paleomagnetic poles that can be used to reconstruct the closure of PAO and determine the paleolatitude of the NCC during the Late Carboniferous and Early Permian. We sampled paleontologically well-dated sedimentary sequences in the central part of the craton that could provide positive reversal and fold tests.

In this chapter, we present a brief review of the Late Paleozoic geology of the NCC, detrital zircon U-Pb ages to constrain the time interval of the study sequences, and rock magnetic study to explore magnetic mineral composition. We report two new paleomagnetic poles from the Taiyuan (Late Carboniferous) and Shanxi Formations (Early Permian) and their tectonic implications within the Late Paleozoic tectonic framework of PAO. On the basis of the new results, the NCC was located

at higher latitudes around 30°N, which implies that the width of PAO was likely less than it was proposed in the previous works.

## 2.2. Geological background

### 2.2.1. Regional tectonic settings

The NCC is one of the oldest cratons comprising the Eastern Asian collage. The NCC is commonly divided into the Western and Eastern Blocks separated by the Central Orogenic Belt (COB) (Zhao et al., 2001, 2005) (Fig. 2.1a). The COB was formed during a multi-stage collision between the Western and Eastern Blocks that took place in the Precambrian (Kusky et al., 2016; Zhao et al., 2005). The metamorphosed Precambrian basement of the COB is unconformably overlain by the Lower Paleozoic carbonates and Upper Paleozoic - Mesozoic clastic rocks (Kusky et al., 2016; Zhao et al., 2005).

Our study area is located within the Lüliangshan Orogenic System which forms the western flank of the central part of the COB (Fig. 2.1, 2.2).

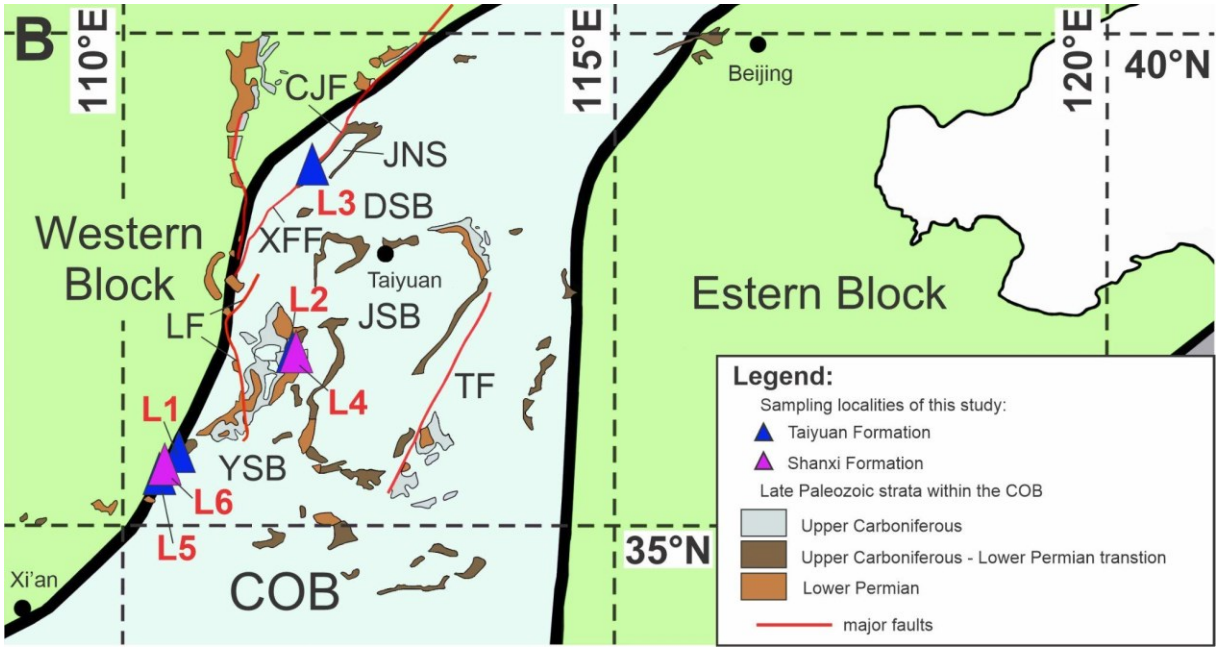


Figure 2.2. Simplified geological map of the Late Carboniferous – Early Permian deposits of the Central Orogenic Belt, NCC with these study sampling localities (modified after Chen (2004)). Blue triangles – Taiyuan sampling localities, yellow triangles – Shanxi sampling localities. L1 – number of a locality, red solid lines – faults (Zhang et al., 2020). CJF - Chunjingwa Fault, DSB - Datong Subbasin, JNS - Jingle-Ningwu Syncline, JSB - Jinzhong Subbasin, LF - Lishi Faultz, LLSM - Luliangshan Mountains, TF – Taihangshan Fault, XFF - Ximafang Fault, YSB - Yuncheng Subbasin (Zhang et al., 2020). The Shanxi Graben System incorporates Yuncheng, Jinzhong, and Datong subbasins.

The Lüliangshan Orogenic System incorporates a series of faults including the Lishi, Luoyunshan, Ximafang, and Chunjingwa faults, and is separated from the Taihangshan Fault by the Cenozoic Shanxi Graben System composed of Yuncheng, Jinzhong and Datong sedimentary subbasins (Fig. 2.2). Folding of the Paleozoic-Early Mesozoic strata of the Luliangshan and Taihangshan indicates that these orogens formed no earlier than the Late Triassic (Zhang et al., 2020; Zhao et al., 2020; reference therein). The tectonic setting of the Late Triassic - Cretaceous deformation remains debatable. It has been proposed that the amalgamation of the NCC and SCC and the west-dipping subduction of the Paleo Pacific plate beneath the NCC reactivated basement structures within the COB (Zhang et al., 2020; Zhao et al., 2020; reference therein).

A cornerstone in the Paleozoic tectonic framework of the NCC is the relationship between the NCC and Alxa Block (Fig. 2.1). It is a crucial aspect in the reconstruction of the Paleozoic position of the NCC because all available paleomagnetic data referring to the Silurian, Devonian, and Early Carboniferous were obtained from rocks collected in the Alxa Block. There is still no solid evidence that the Alxa Block was a part of the NCC throughout its Paleozoic history. Recent geochronological and sedimentological studies suggested that the Alxa Block collided with the NCC between the Late Devonian and Early Carboniferous (Zhang et al., 2016). On the contrary, Yuan and Yang (2015) and Wang et al. (2020) proposed that the Alxa Block was not amalgamated with the NCC until the Late Permian - Early Mesozoic. In our further discussion, we assume that the Alxa Block was a part of the NCC by the Late Carboniferous as it is suggested by the majority of studies (Huang et al., 1999, 2000; Dan et al., 2016; Zhang et al., 2016).

The tectonic framework of PAO could not be accomplished without considering the relationship of the NCC with the Inner Mongolia and Amuria composite terranes, Songliao Block, and adjacent accretionary complexes (Fig. 2.1). Most of East Asia consists of multiple accreted cratonal blocks, terranes, and island arcs. Boundaries between most of them are still not well-defined therefore we depicted only the major tectonic units that compose the Inner Mongolia, Amuria, and Altai-Gobi Zone (Figure 2.1). The Inner Mongolia consists of Bainaimiao, Ondor Sum, Erdaojing, Baolidao, and Hegenshan arc complexes successively welded together during the Paleozoic Era due to the closure of PAO branches (Fig. 2.1). In the north, the Inner Mongolia's neighbors the Nuhetdavaa fore/backarc terrane and Uliastai active continental margin. Since the Uliastai is thought to be a continuation of the Nuhetdavaa (Xiao et al., 2003), we combined these tectonic units into a consolidated tectonic unit NUT (Nuhetdavaa-Uliastai terrane). The Nuhetdavaa consists of Neoproterozoic metamorphosed sedimentary strata covered by the Paleozoic sedimentary and

volcanic units (Badarch et al., 2002). The Uliastai continental margin is composed of the Proterozoic metamorphosed sedimentary rocks overlain by the Paleozoic volcanic and sedimentary successions (Xiao et al., 2003).

In our study, Amuria includes the Mongol-Okhotsk Belt (MOB) bounded by the cratonal blocks such as Erguna, Herlen, Baydrag, Zavkhan, passive continental margin terrane Idermeg, and island arcs (Fig. 2.1). In the Late Paleozoic, the southern part of Amuria developed as a composite accretionary arc complex composed of the Precambrian continental crust in a core with the joined Early Paleozoic accretionary complexes. The northern part of Amuria evolved as the island arcs in the Late Paleozoic (Badarch et al., 2002).

The Erguna Block consists of a Meso-Neoproterozoic basement covered by the Paleozoic-Mesozoic sedimentary and volcanic strata (Han et al., 2015). To the southeast, the Erguna Block borders the Xing'an Block (Fig. 2.1). The Xing'an Block predominantly consists of Mesozoic volcanic rocks with minor Paleozoic sedimentary units (Han et al., 2015). Based on geochronological and geochemical studies Han et al. (2015) suggested that the Erguna and Xing'an Blocks collided in the Middle Cambrian. The Xing'an Block connects to the Songliao Block in the southeast (Fig. 2.1). The Songliao Block is composed of mostly Paleozoic-Mesozoic metamorphosed volcanic and sedimentary units (Han et al., 2015).

In the south, the Amuria borders the Mandalovoo island arc terrane consisting of the Paleozoic sedimentary and volcanic units (Badarch et al., 2002). During the Paleozoic Era, the Mandalovoo terrane evolved as an island arc on the southern margin of the accretionary complex constituting the Amuria (Badarch et al., 2002). The Mandalovoo terrane borders the Altai-Gobi Zone on the west and south. The Altai-Gobi Zone represents a complicated system of the back/forearc basins

composed of the Paleozoic metamorphosed sedimentary and volcanic strata (Badarch et al., 2002). The Mandalovoo terrane and Gobi-Altai Zone are attributed to the Paleozoic subduction of an oceanic plate beneath the arc accretionary complex (Badarch et al., 2002; Şengör et al., 2018).

In the south, the Altai-Gobi Zone connects to the Beishan Orogenic complex (BOC) formed in multiple stages of accretion and subduction of PAO during the Paleozoic Era (Wang et al., 2020; Xiao et al., 2018; Xu et al., 2019, and the references therein; Zheng et al., 2018) (Fig. 2.1). The timing and tectonic settings of the final stage of the BOC formation are poorly constrained to the Late Paleozoic (Wang et al., 2020; Xu et al., 2019; and the references therein; Zheng et al., 2018).

### 2.2.2. Geological background of the study area

The Late Paleozoic strata of the study localities include the Benxi (Early Carboniferous), Taiyuan (Late Carboniferous), and Shanxi (Early Permian) formations (Fig. 2.3).

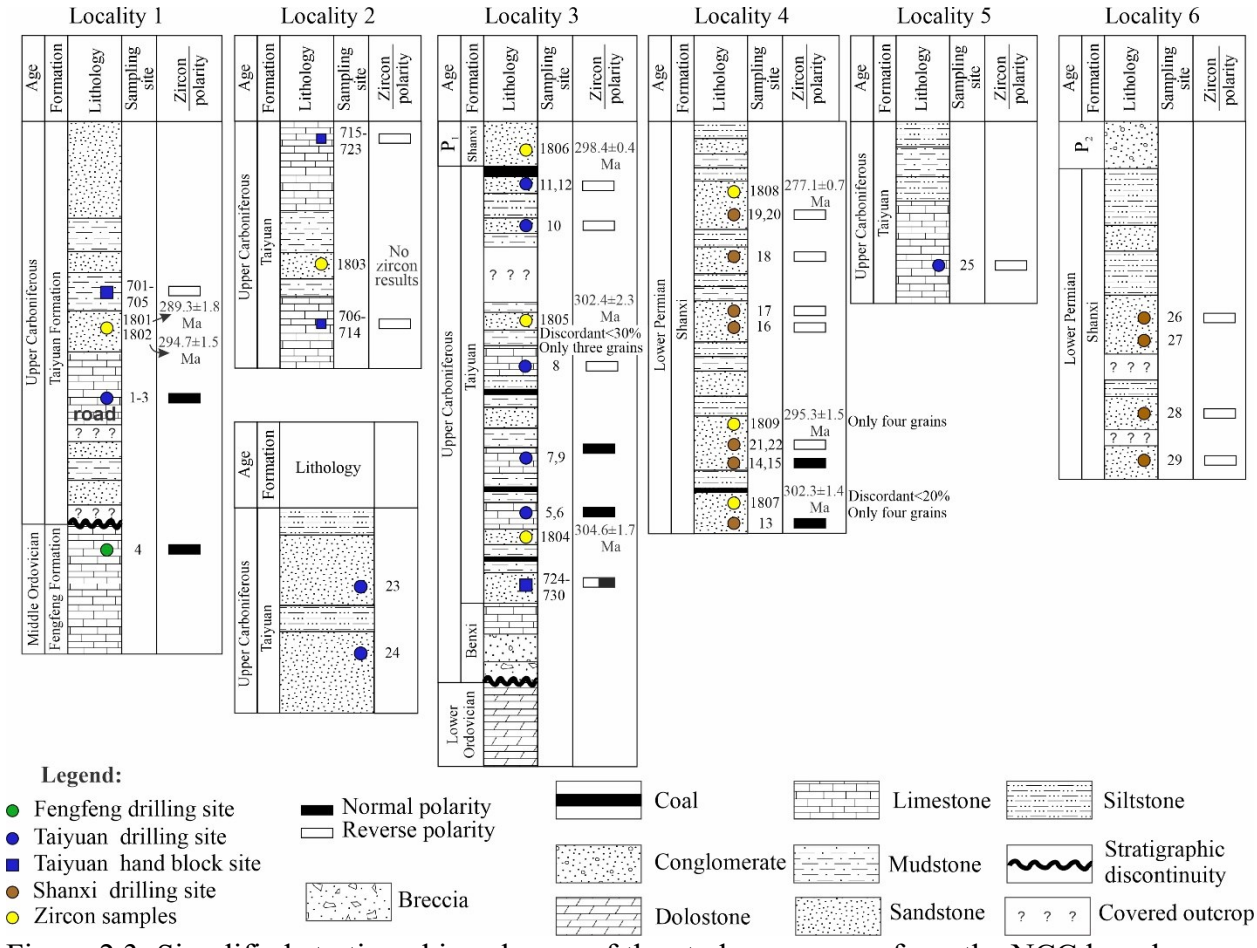


Figure 2.3. Simplified stratigraphic columns of the study sequences from the NCC based on our study.

The Late Paleozoic strata within the study area unconformably overlie the Early - Middle Ordovician strata. The Middle Ordovician strata, consisting of the Fengfeng Formation, were observed only in the south (locality 1). In the northern areas, the Late Paleozoic strata overlie Early Ordovician dolostones (Zhen et al., 2016).

We describe the exposed formations from the oldest to the youngest. The Middle Ordovician Fengfeng Formation consists of brecciated, karstified yellowish limestones with fractured calcite and gray micritic limestone (Yu et al., 2005; Fu et al., 2010). The Fengfeng Formation is unconformably overlain by the Middle Carboniferous Benxi Formation (Lv and Chen, 2014; Zhen et al., 2016). The unconformity is characterized by a bauxite layer with pebble conglomerate

overlain by a coarse-grained quartz sandstone and carbonate (Cleal and Ziqiang, 2002). The Benxi Formation was accumulated in lagoons, swamps, and fluvial plains during a northwest to southeast marine transgression (Liu, 1990; Li et al., 1998). Paleontological studies indicate a Westphalian depositional age for the Benxi Formation age (Li et al., 1999; Cleal and Ziqiang, 2002). Liu (1990) suggested that the lower Benxi Formation may be in part Namurian.

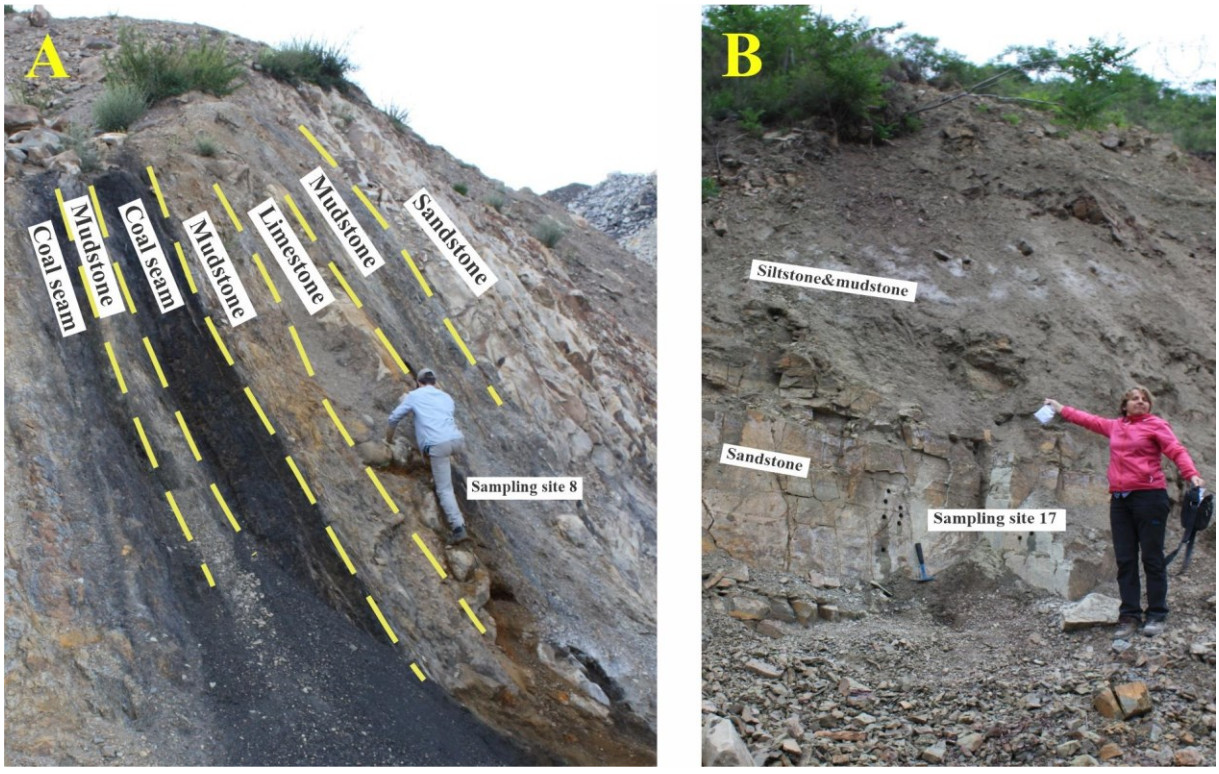

Figure 2.4. Field photographs of the study formations. A) Locality 3, Taiyuan Formation. B) Locality 4, Shanxi Formation.

The Taiyuan Formation conformably overlies the Benxi Formation and consists of interbedded carbonate and terrigenous clastic rocks (Li et al., 1998; Li et al., 1999) including dark gray and gray micritic and bioclastic limestones (Fig. 2.4a). Siliciclastic deposits of the Taiyuan Formation include black and gray mudstones, siltstones, and gray sandstones with thin coalbeds. Deposition occurred within a fluvial to the epicontinental marine environment (Li et al., 1998). Marine fossils include fusulinid, rugose corals, and crinoids (Wang et al., 2019) and indicate a humid and warm tropical and subtropical climate (Lv and Chen, 2014; Wang and Pfefferkorn, 2013).

The Taiyuan Formation is conformably overlain by light grey, white, greenish medium-fine sandstone interbedded with sandy mudstone, siltstone, and thin coal seams of the Shanxi Formation (Li et al., 1999; Wang et al., 2010; Zhang et al., 2019) (Fig. 2.4b). Coalbeds of the Shanxi Formations accumulated in marshes and peat bogs alongside delta channels and were observed in the lower part of the outcrop at locality 4 (Jin et al., 2015).

Disagreements remain over the age of the Taiyuan and Shanxi Formations boundary (Fig. 2.5).

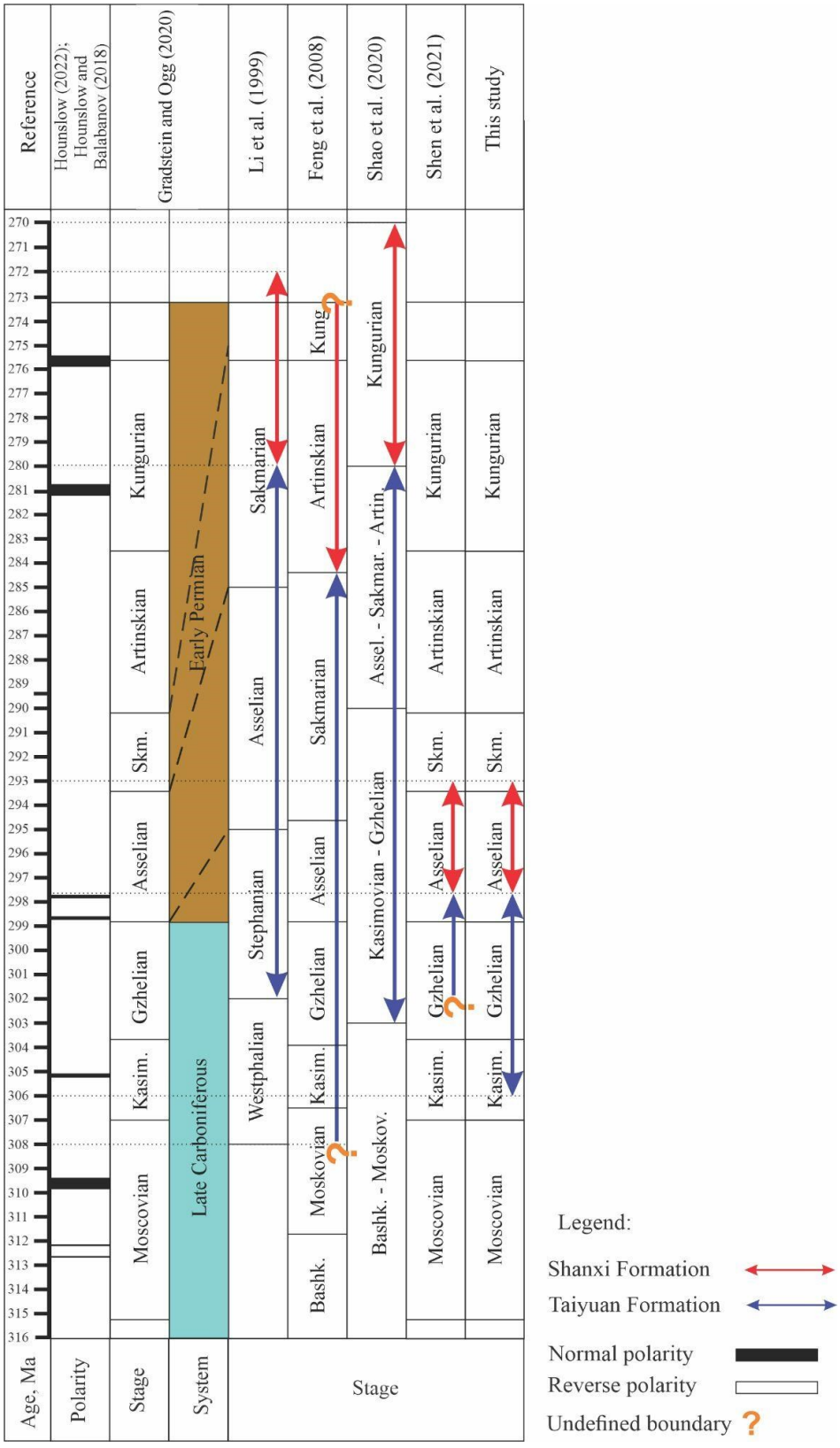


Figure 2.5. Magnetostratigraphic scale showing the magnetic polarity and chronostratigraphic subdivisions of the Taiyuan and Shanxi Formations in different studies.

Subdivisions for the Taiyuan and Shanxi Formations proposed in Li et al. (1999) and Shao et al. (2020) and based on a coal seams correlation suggested age ranges ~303 - 280 Ma and ~280 - 270 Ma respectively. In contrast, Feng et al. (2008) using palynological data, defined the Taiyuan and Shanxi formations age ranges as ~308 - 284 Ma and ~284 - 273 Ma, respectively. Shen et al. (2021), based on biostratigraphical and coal seams correlations, constrained the Shanxi Formation deposition to between 297.6 to 293 Ma. These ages are older, and the period of deposition is shorter than in previous studies (Fig. 2.5). Yang et al. (2020) reported zircon ages of 301 Ma and 296 Ma from the bottom and top of the Taiyuan sequence implying that the top of the formation is younger than 296 Ma (Fig. 2.5). However, Yang et al. (2020) collected their samples from the southern NCC where the Taiyuan Formation sequences are thinner compared to sequences in the central and north parts of the NCC. Based on the brief review of the proposed stratigraphical subdivisions of the Taiyuan and Shanxi Formations, we define the Taiyuan Formation deposition as extending from 306 to 298 Ma. The Shanxi Formation deposition is from 298 to 293 Ma based on Shen et al. (2021) (Fig. 2.5).

## 2.3. Sampling and Methods

### 2.3.1. Sampling

Our study area included six localities. We describe the sampling localities from the south toward the north (Fig. 2.2). Localities 1, 5, and 6 were situated on the southwest boundary of COB near the Yuncheng subbasin. The Upper Paleozoic strata in locality 1 strike ~290° NW and dip up to 20° to the north-northeast. Localities 5 and 6 were situated 10 km to the south of locality 1. There the Upper Paleozoic strata strike ~220°SW and dip NW 20 - 40°. Localities 2 and 4 are situated 180 km from locality 1 to the north along the western flank of the COB. Bedding dips shallowly

(~10°) to the SE and strikes to the north (Fig. 2.4b). Locality 3 was situated in the western limb of the Jingle-Ningwu syncline 200 km to the north of localities 2 and 4. Bedding strikes between 350° NW and 020° NE with dips 50° to the east (Fig. 2.4a).

One drilling sampling site was collected from the Fengfeng Formation (Middle Ordovician), 14 drilling and 4 hand block sampling sites were collected from the Taiyuan Formation, and 14 drilling sites from the Shanxi Formation. We cut 784 samples from all drilling cores and hand blocks for laboratory measurements. The samples include limestones, sandstones, and mudstones.

Drilling samples were collected using a portable gasoline drilling machine and were oriented in place by an ASC Scientific Pomeroy orienting fixture. The top of the fixture accommodated a clear plastic sun compass which was used for sun azimuth measurements (weather permitting). Solar and magnetic azimuths proved to be identical, demonstrating an absence of magnetic hindrance or noise during the orientation of drilling cores. Hand samples were oriented in the field using standard magnetic compasses. A handheld GPS "Garmin" was used for obtaining the geographic coordinates of the sampling sites.

### 2.3.2. Methods

All sample cores were cut into cylinders with a 2.5 cm diameter and 1.5 – 2.2 cm height and subjected to stepwise demagnetization from 100 to 690°C in one chamber ASC TD48 Thermal Demagnetizer. Measurements of the remanent magnetization were conducted on the 2G Enterprise SQUID DC-4K (755-1.65) cryogenic magnetometer. An interpretation of remanent magnetization directions was conducted using the principal component analysis (PCA) of the stepwise thermal demagnetization data (Kirschvink, 1980) in Enkin's (2004) software. Statistical analysis of the

mean directions within each sample site and for each formation was conducted using Fisher statistics (Fisher, 1953). For samples with low magnetization resulting in scattered data points in Zijderveld diagrams and stereographs, we used a joint analysis of demagnetization great circles and directions (McFadden & McElhinny, 1988). Identification of a primary magnetization component whether it was acquired before or after folding was conducted by using the fold (McElhinny, 1964, McFadden, 1990) and reversal (McFadden & McElhinny, 1990) tests. All measurements were performed at the Physics Department Paleomagnetic Laboratory of the University of Alberta.

To estimate Curie points the temperature dependence of magnetic susceptibility was determined in the air at the Paleomagnetic Laboratory of the Northwest University, Xi'an, China. Isothermal remanent magnetization (IRM) was measured with a VFTB at the University of Alberta.
All figures with the spherical and equal-area projections were plotted using PaleoMac from Cogné (2003).

### 2.4. U-Pb Zircon Dating

Sandstone units were sampled from both the Taiyuan and Shanxi Formations for detrital zircon geochronology. Zircons were extracted at the ICPMS Laboratory of the University of Alberta. U-Pb zircon data was processed using the software IsoPlotR (Vermeesch, 2018). The U–Pb zircon results are listed in Appendix (Table A1).

The STJ1801 and STJ1802 sandstone samples collected from the outcrop of the Taiyuan Formation, locality 1 (Fig. 2.6), yielded a mean concordia age of 294.7 ± 1.5 Ma (number of grains = 4; MSWD = 1.2, discordant < 15%) and 289.3 ± 1.8 Ma (number of grains = 9; MSWD = 14.0) respectively. The weighted mean age derived from $^{206}Pb/^{238}U$ ratio is 294.8 ± 1.5 Ma (number of

grains = 4/4; MSWD = 12.7) and 285.9 ± 1.9 Ma (number of grains = 4/5; MSWD = 1.1) for the sample STJ1801 and STJ1802 respectively.

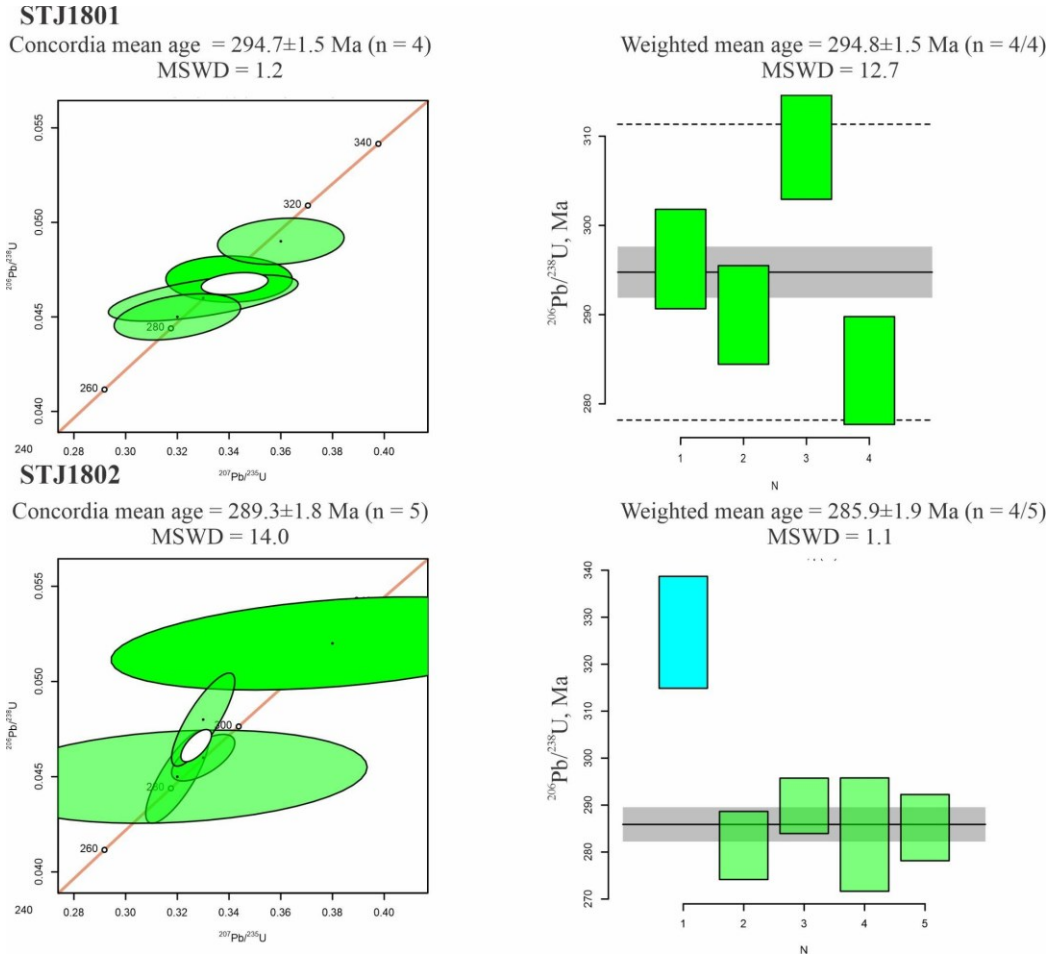


Figure 2.6. Pb-U zircon results for the Taiyuan Formation (STJ1801 and STJ1802 samples), locality 1. The figure is plotted using IsoplotR from Vermeesch (2018).

The small number of zircon grains used in statistics and the significant (15%) discordance of some of the grains resulted in high MSWD values for both concordia and weighted means. In addition, the derived zircon means exceed the timing constraints of the Taiyuan Formation therefore these zircons could not be used in further discussion

The sandstone sample STJ1804 collected along a boundary between the Benxi and Taiyuan Formations, in locality 3 (Fig. 2.7), yielded mean age of 302.1 ± 1.8 Ma (number of grains = 5/7;

MSWD = 0.006) and 304.6 ± 1.7 Ma (number of grains = 7; MSWD = 0.7) based on $^{206}Pb/^{238}U$ and mean concordia dates respectively (Fig. 2.7). It shows that the age of the Taiyuan strata at the bottom of the outcrop within the locality 3 is younger than ~304 - 302 Ma.

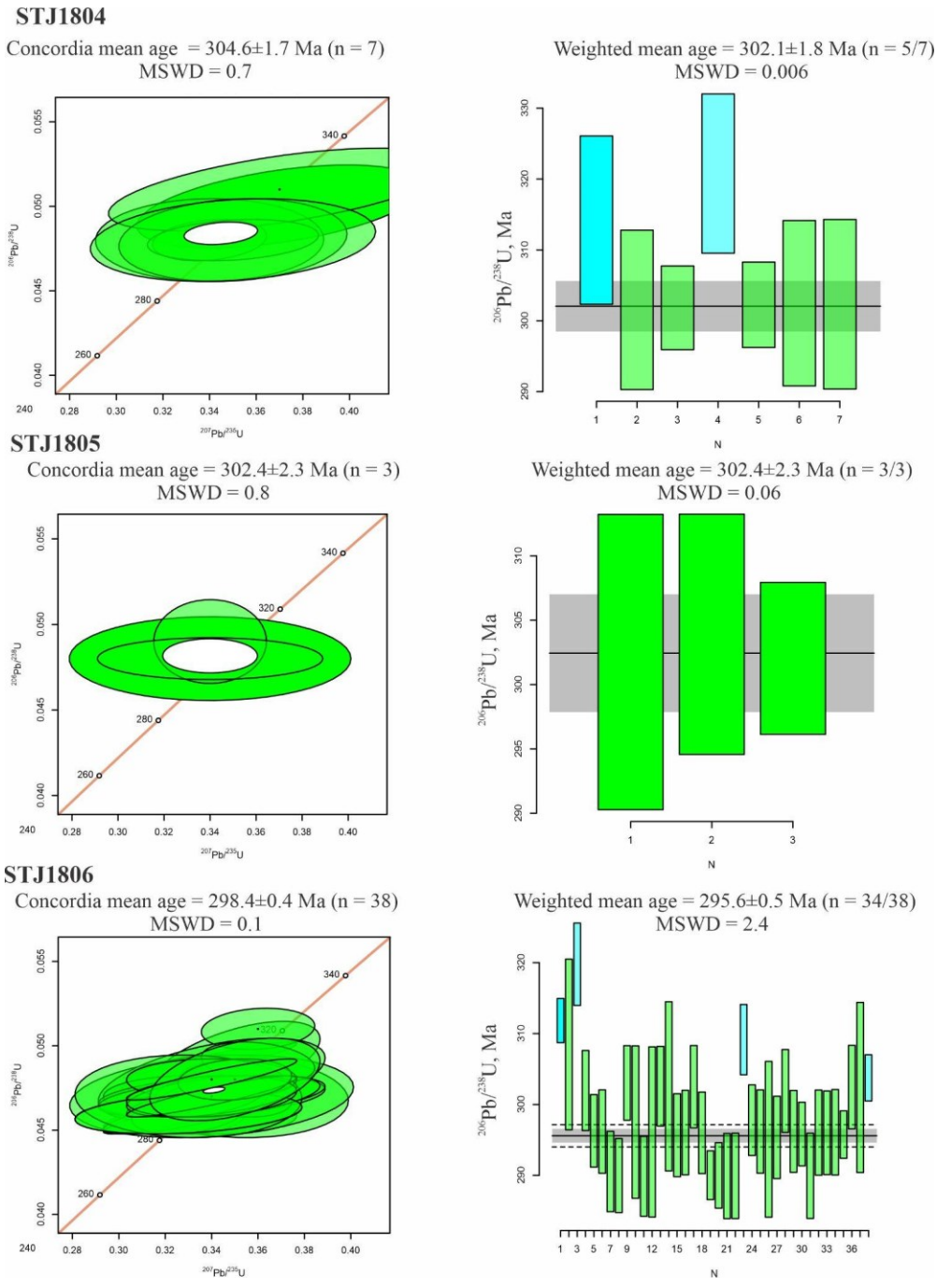


Figure 2.7. Pb-U zircon results for the Taiyuan Formation (STJ1804, STJ1805, STJ1806 samples), locality 3. The figure is plotted using IsoplotR from Vermeesch (2018).

Sandstone sample STJ1806 collected from the top of the Taiyuan Formation, in locality 3 (Fig. 2.7), yielded mean zircon ages in 298.4 ± 0.4 Ma (number of grains = 38; MSWD = 0.1) and 295.6 ± 0.5 Ma (number of grains = 34/38; MSWD = 2.4) based on concordia and $^{206}Pb/^{238}U$ ratios respectively. It implies that the age of the Taiyuan strata at the top of this section is younger than ~298 - 295 Ma. The sample STJ1805 provided only three zircon grains that could not be regarded as reliable (Fig. 2.7).

The obtained zircon ages suggest that the oldest depositional age of the Taiyuan Formation within the study area is younger than ~306 Ma. This age range corresponds to the Kasimovian stage of the Upper Carboniferous. The youngest zircon age from the top of the Taiyuan Formation on locality 3 is 298 Ma that is close to the boundary between the Late Carboniferous and Early Permian.

Sandstones STJ1807 and STJ1809 collected from the lower part of the exposed Shanxi Formation yielded a small number of grains with highly discordant (~20%) that provided no reliable data (Fig. 2.8).

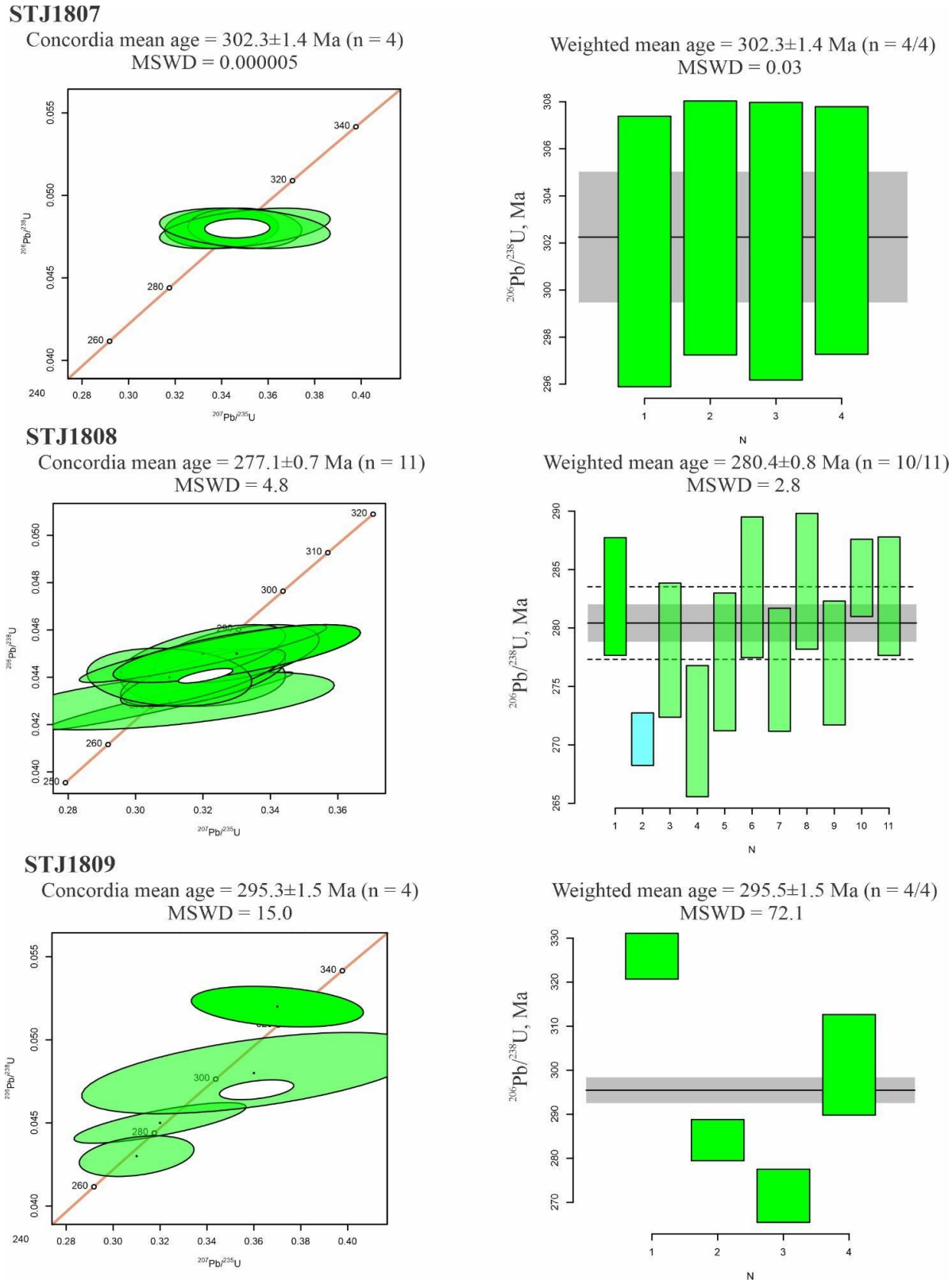


Figure 2.8. Pb-U zircon results for the Shanxi Formation (STJ1808 and STJ1809 samples), locality 4. The figure is plotted using IsoplotR from Vermeesch (2018).

Sample STJ1808 was collected from the top of the studied outcrop of the Shanxi Formation. Zircon mean from the STJ1808 is 277.1 ± 0.7 Ma (number of grains = 11; MSWD = 4.8, discordant < 15%) based on concordia mean age and 280.4 ± 0.8 Ma (number of grains = 10/11; MSWD = 2.8, discordant < 15%) based on $^{206}Pb/^{238}U$ ratio (Fig. 2.8). These zircon ages correspond to the Kungurian stage of the Early Permian. Since we derived only one reliable mean zircon age, we could not constrain the time interval of the Shanxi Formation within our study area.

To estimate the quality of the Pb-U dating, the age of Plesovice zircon grains was determined in accordance with the Plesovice standard in Sláma et al. (2008). The obtained mean Plesovice age is 337.5 ± 0.3 Ma (number of grains = 47/48; MSWD = 2.0) based on the weighted mean of $^{206}Pb/^{238}U$ ratio (Fig. 2.9) which correlates with 337.1 ± 0.4 Ma Plesovice standard calculated in Sláma et al. (2008).

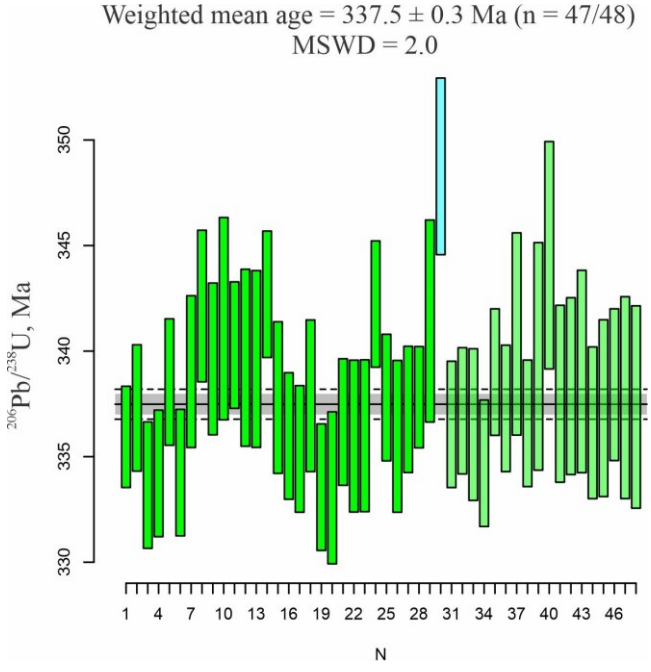


Figure 2.9. Pb-U dating of the reference Plesovice zircon grains.

## 2.5. Rock-magnetic Analysis

The temperature-dependent magnetic susceptibility graphs for the Taiyuan and Shanxi samples are illustrated in Figure 2.10 with two main types of magnetic susceptibility vs. temperature curves (k-T curves) in the air.

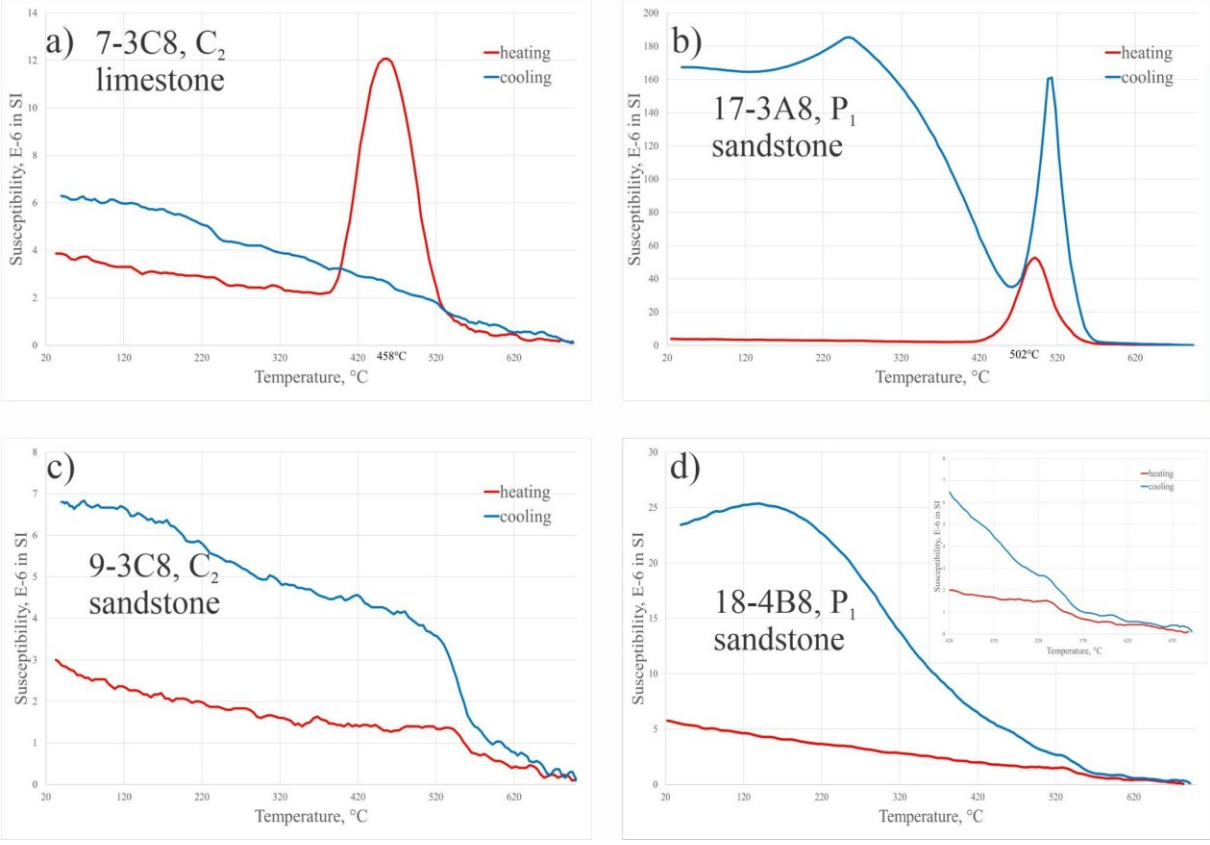


Figure 2.10. Representative thermomagnetic curves from samples of the Taiyuan and Shanxi Formations.

The first type of k-T curves is irreversible with the distinctive Hopkinson peaks in the temperature range between 450 - 520°C (Fig. 2.10a, b). This indicates titanomagnetite as a predominant carrier of NRM for the Taiyuan and Shanxi samples. The final demagnetization was achieved at 650°C that marks the presence of a fraction of hematite.

The second type of k-T curves was also irreversible and characterized by a moderate decrease up to 520 - 540°C proceeded by a steep step down in the temperature range between 520 - 570°C (Fig. 2.10c, d). The final demagnetization was gained at ~690°C. This indicates a mixture of magnetite and hematite.

In all cases the k-T curves were irreversible or nearly irreversible, the cooling curves passed above the heating curves with a significant exceeding at the low temperature range after 200°C. This indicates an oxidation process during measurements causing the formation of new magnetic minerals.

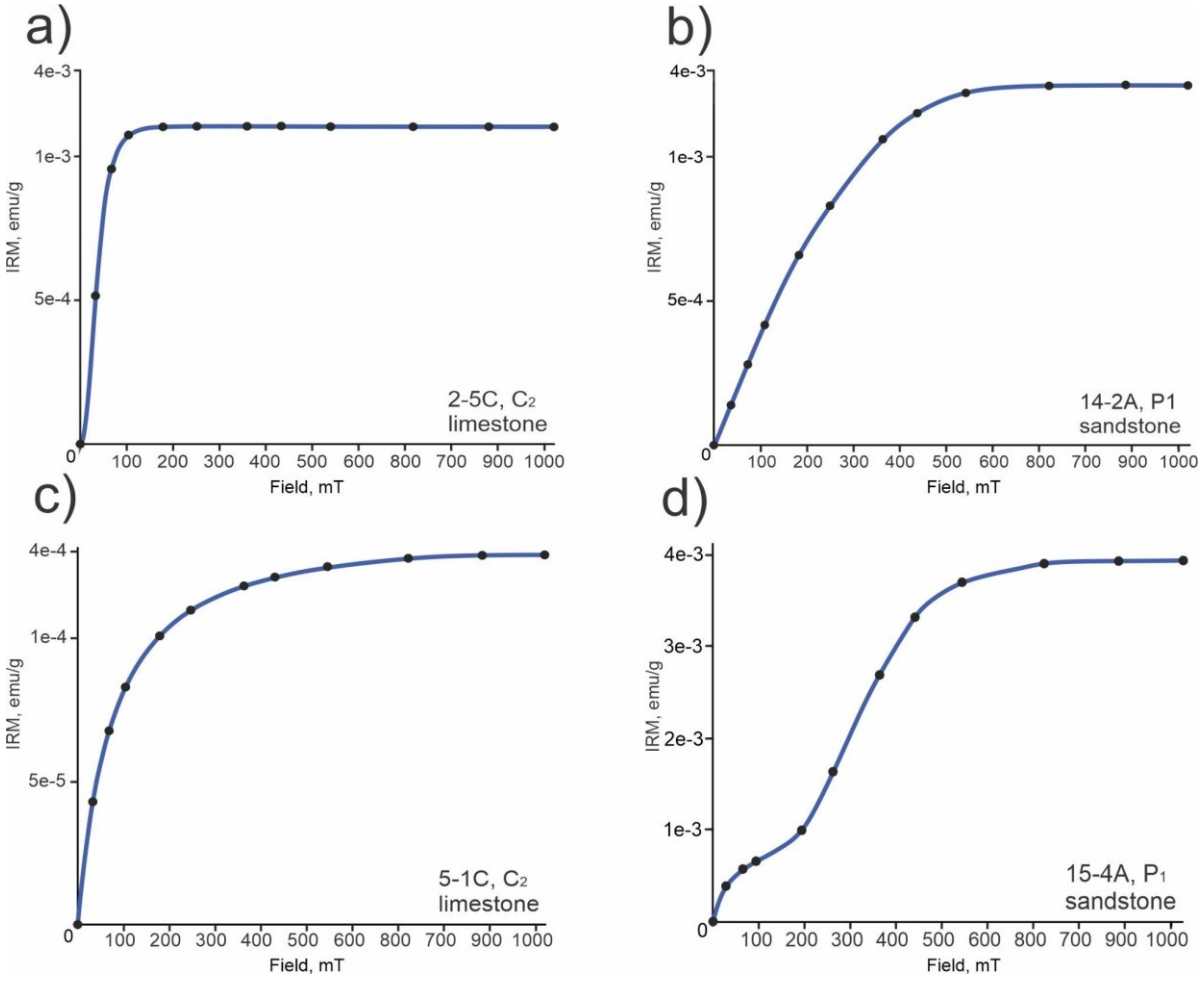


Figure 2.11. Representative IRM curves from samples of the Taiyuan and Shanxi Formations.

IRM acquisition was carried out with a magnetic field up to 1000 mT. Due to a weak magnetization of the Taiyuan and Shanxi samples, only about 10% of the measured samples yielded adequate IRM curves. The most representative IRM curves are shown in Figure 2.11. Limestones of the Taiyuan Formation yielded the two most distinct IRM curves. The first type of IRM curves (Fig. 2.11a) acquired saturation up to 150 mT. This indicates magnetite as a predominant carrier of NRM. The second type of IRM curves derived from limestones of the Taiyuan Formation was characterized by a saturation between 400 - 900 mT (Fig. 2.11c). This reveals a mixture of magnetic minerals carrying the magnetization, most likely titanomagnetite/magnetite and hematite. The IRM curves of the Shanxi samples mostly showed a saturation of 600 - 900 mT (Fig. 2.11b, d) that indicates a mixture of magnetite and hematite as the most likely carrier of NRM.

## 2.6. Paleomagnetic results

### 2.6.1. Fengfeng Formation

The reliable Ordovician paleomagnetic poles have been already published in previous works (Huang et al., 2018). The difference between the Ordovician and Carboniferous directions, however, can be used to assess a possibility of a regional overprint at the sampling locality therefore we sampled one site (site 4) of the Middle Ordovician Fengfeng Formation at locality 1.

A low temperature component (LTC) of the Fengfeng Formation samples was defined in the temperature range between 100°C and 200 - 300°C using the PCA method (Fig. 2.12a, b, c).

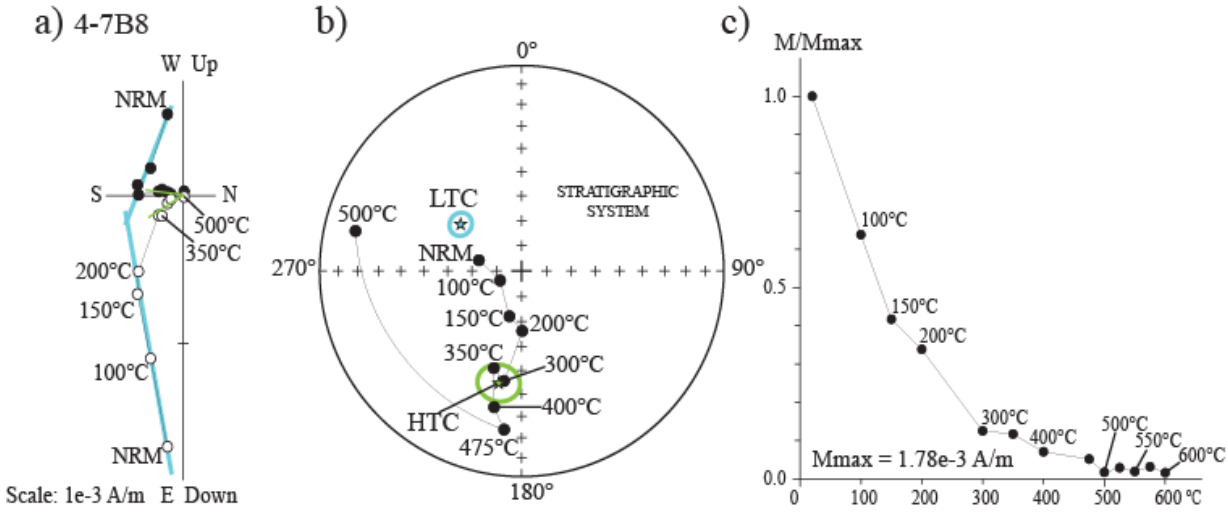


Figure 2.12. Representative (A) Zijderveld diagram, (B) equal-area projection of the directions, and (C) step-wise demagnetization plot for the Fengfeng Formation samples. Blue line, star - a direction obtained from the low temperature component (LTC), green line, circle - a direction obtained from the high temperature component (HTC).

The mean direction of the LTC is Dg = 309.1°, Ig = 69.5° ($\alpha_{95}$ = 23.0°, kg = 12.0, n = 5 samples) in geographic coordinates and Ds = 323.6°, Is = 64.0° ($\alpha_{95}$ = 23.0°, ks = 12.1) in stratigraphic coordinates (Table 2.1, Fig. 2.13a, b). The confidence cone $\alpha_{95}$ of the mean LTC direction is close to the direction of the present-day geomagnetic field (PDF). In addition, nine of 14 samples on the same temperature range yielded a cluster of directions at Dg = 185.9°, Ig = 63.8° ($\alpha_{95}$ = 10.9°, kg = 23.9, n = 9 samples) and Ds = 186.4°, Is = 72.1° ($\alpha_{95}$ = 10.9°, ks = 23.1) in stratigraphic coordinates. This mean direction probably corresponds to the middle temperature component (Fig. 2.13a).

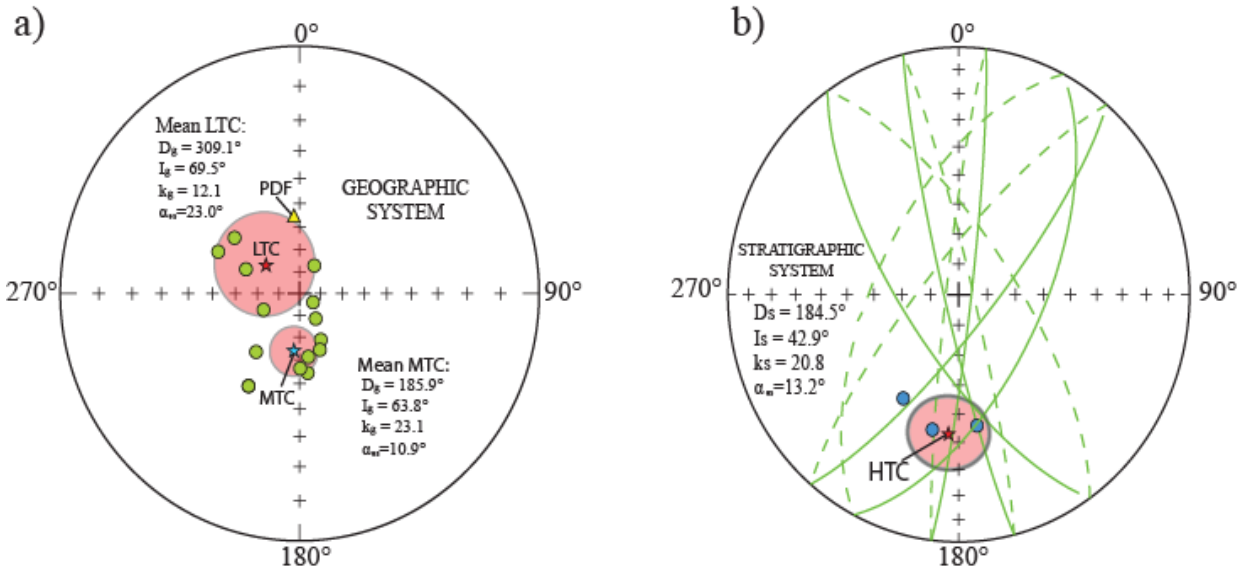


Figure 2.13. A) stereographic projection of the low temperature component (LTC) and middle temperature component (MTC) directions. PDF - present-day geomagnetic field (yellow triangle). B) equal-area of the high temperature component (HTC) directions. The red star is a mean direction drawn from the LTC directions (a) and HTC directions (b), and the green star is a mean direction drawn from the MTC directions. Blue circles - HTC directions obtained using PCA analysis. Green circles - great circle fitting, a dashed line of circles is a part of circles crossing the reverse polarity, solid green line of a circle corresponds to the normal polarity.

A high temperature component (HTC) of the Fengfeng Formation samples was isolated between 300 and 450 - 475°C. The mean direction from the HTC was in Dg = 184.5°, Ig = 34.6° ($\alpha_{95}$ = 13.2°, kg = 20.8, n =8 samples) in geographic coordinates and Ds = 184.5°, Is = 42.9° ($\alpha_{95}$ = 13.2°, ks = 20.8) in stratigraphic coordinates (Table 2.1, Fig. 2.13b).

Table 2.1. Low, middle, and high temperature components for the Ordovician samples, sampling site 4, locality 1

| Locality | Site ID | Temperature component | Strike (°) | Dip (°) | $n/n_0$ | N/R | Dg (°) | Ig (°) | k | $\alpha_{95}$ (°) | Ds (°) | Is (°) | k | $\alpha_{95}$ (°) |
|---|---|---|---|---|---|---|---|---|---|---|---|---|---|---|
| 1 | 4 | LTC | 279.2 | 8.3 | 5/14 | 5/14 | 309.1 | 69.5 | 12.0 | 23.0 | 323.6 | 64.0 | 12.1 | 23.0 |
| | | MTC | | | 8/14 | 9/14 | 185.9 | 63.8 | 23.1 | 10.9 | 186.4 | 72.1 | 23.1 | 10.9 |
| | | HTC | | | 6/14 | 8/14 | 184.5 | 34.6 | 20.8 | 13.2 | 184.5 | 42.9 | 20.8 | 13.2 |

*Dg, s and Ig, s - declination and inclination respectively in the geographic and stratigraphic systems, kg and $\alpha_{95}$ - Fisher dispersion parameter and radius of the 95% confidence cone respectively, n - number of samples used in the calculation, $n_0$ - number of measured samples.

Obtained HTC mean direction from sampling site 4 yielded a paleomagnetic pole at 29.2°N, 285.9°E (A=12.9°, paleolatitude = 24.9°S) (Fig. 2.14). Since this paleomagnetic pole was calculated only for one sampling site, it could not be regarded as a reliable pole. Nonetheless, the paleomagnetic pole agrees with the published poles (Huang et al., 2018) in the previous studies of the Middle Ordovician for the NCC (Fig. 2.14). This result demonstrates that the Middle Ordovician direction is most likely primary and regional overprint in the sampling area is unlikely.

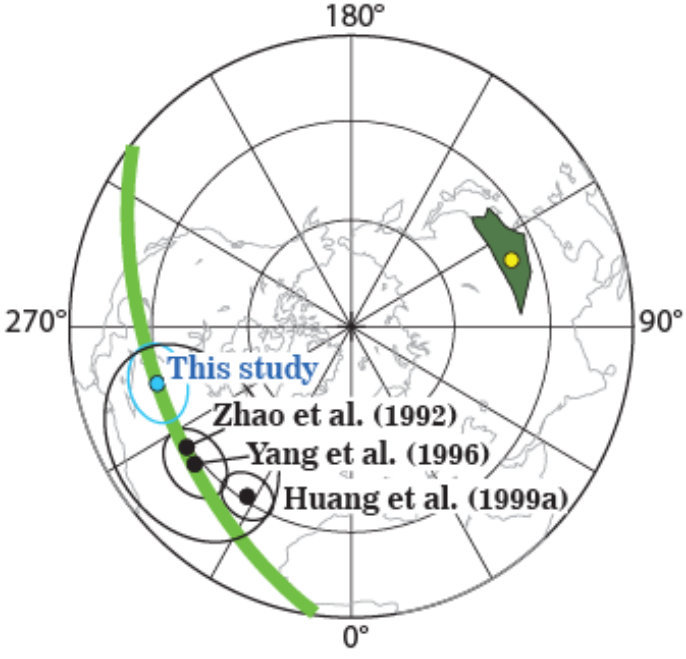


Figure 2.14. Equal-area projection of the Ordovician paleomagnetic poles for the NCC.

### 2.6.2. Taiyuan Formation

The LTC for the Taiyuan Formation was defined in the temperature range NRM - 200°C or 100 - 200°C for the samples from localities 1 and 5 and in the temperature range 100 - 300°C for the samples from locality 3 (Fig. 2.15, 2.16).

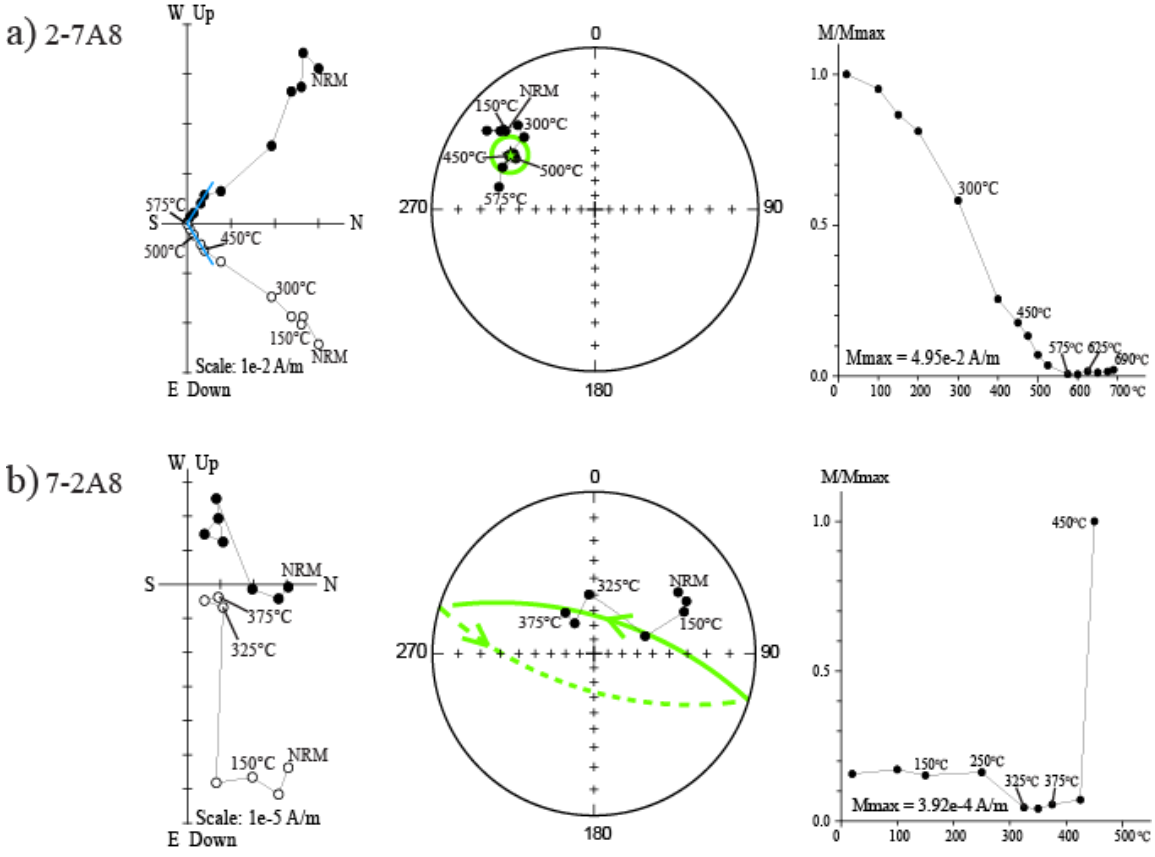


Figure 2.15. Zijderveld diagrams, stereographic projection of the directions for the high temperature component (a) and great circle fitting (b), and step-wise demagnetization plots of representative samples yielded a normal polarity. The blue line corresponds to the high temperature component trend along the great circle.

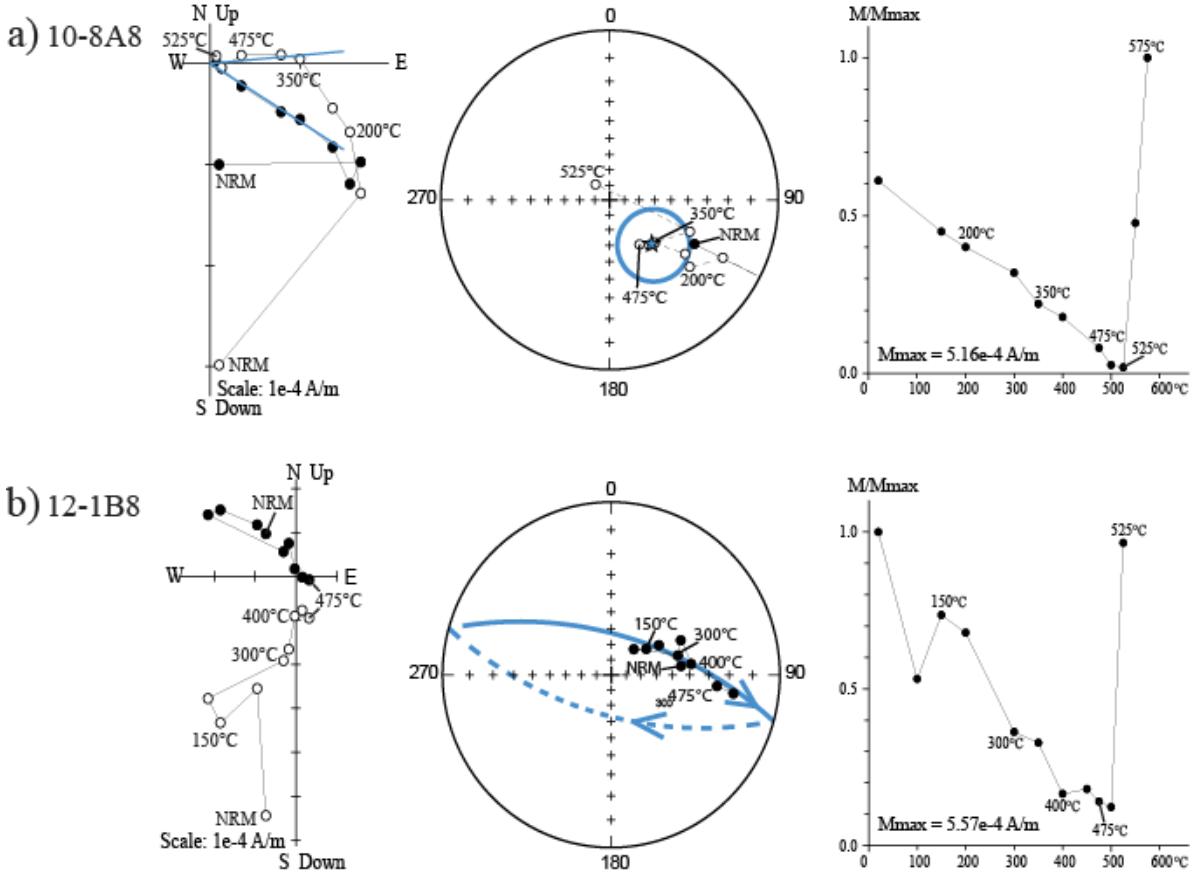


Figure 2.16. Zijderveld diagrams, stereographic projection of the directions for the high temperature component (a) and great circle fitting (b), and step-wise demagnetization plots of representative samples yielded a reverse polarity. The blue line corresponds to the high temperature component trend along the great circle.

The LTC yielded the mean direction at Dg = 352.8°, Ig = 59.9° ($\alpha_{95}$ = 5.6°, kg = 48.2, n = 169 samples) for 15 sites in geographic coordinates and at Ds =33.1°, Is = 45.2° ($\alpha_{95}$ = 14.8°, ks = 7.7) in stratigraphic coordinates (Fig. 2.17, Table 2.2). The direction in geographic coordinates overlaps the PDF within its $\alpha_{95}$ ($D_{PDF}$ = 355.6°, $I_{PDF}$ = 54.9°) while in the stratigraphic coordinates the PDF value lies beyond the cone of confidence for the LTC. Therefore, this suggests that the LTC corresponds to the PDF overprint.

Table 2.2. Summary of results for the low temperature component of the Taiyuan Formation, NCC.

| Locality | Site ID | Strike (°) | Dip (°) | $n/n_0$ | Dg(°) | Ig(°) | kg | $\alpha_{95}$(°) | Ds(°) | Is(°) | ks | $\alpha_{95}$(°) |
|---|---|---|---|---|---|---|---|---|---|---|---|---|
| 1 | 1 | 288.5 | 16 | 8/16 | 323.0 | 60.7 | 16.8 | 13.9 | 338.7 | 48.9 | 16.8 | 13.9 |
| | 2 | 201.3 | 13 | 8/17 | 335.7 | 64.8 | 12.6 | 16.2 | 320.8 | 55 | 12.6 | 16.2 |
| | 3 | 264 | 12 | 5/19 | 340.8 | 71.4 | 6 | 34.1 | 344.1 | 59.5 | 6 | 34.2 |
| | HB1 701-705 | 66.5 | 9.6 | 12/17 | 330.0 | 62.4 | 6.6 | 18.3 | 331.9 | 69.8 | 6.5 | 18.5 |
| 2 | 23 | 279.1 | 9.4 | 0/9 | 0 | 0 | 0 | 0 | 0 | 0 | 0 | 0 |
| | 24 | 279.1 | 9.4 | 0/6 | 0 | 0 | 0 | 0 | 0 | 0 | 0 | 0 |
| | HB2 706-723 | 68.5 | 11.5 | 41/54 | 358.6 | 53.6 | 15.3 | 5.9 | 355.6 | 56.7 | 9.5 | 7.6 |
| 3 | 5 | 1.8 | 58.9 | 15/17 | 5.6 | 46.3 | 7.3 | 15.2 | 41.2 | 16.3 | 7.3 | 15.2 |
| | 6 | 1.8 | 58.9 | 11/16 | 351.7 | 64.9 | 12.2 | 13.6 | 57.4 | 29.9 | 12.2 | 13.6 |
| | 7 | 1.8 | 58.9 | 13/16 | 5.3 | 62.9 | 10.1 | 13.7 | 57.1 | 23.6 | 10.1 | 13.7 |
| | 8 | 357.2 | 55.3 | 8/9 | 342.1 | 66.1 | 5.6 | 25.8 | 52.7 | 35.3 | 5.5 | 25.9 |
| | 9 | 1.8 | 58.9 | 8/13 | 347.3 | 55.6 | 10.3 | 18.2 | 46.3 | 30.2 | 10.3 | 18.1 |
| | 10 | 11.2 | 53.3 | 9/14 | 5.8 | 61.4 | 13.0 | 14.8 | 61.6 | 31.7 | 13.0 | 14.8 |
| | 11 | 11.2 | 53.3 | 7/11 | 349.6 | 52.3 | 11.8 | 18.3 | 48.1 | 37.6 | 11.8 | 18.3 |
| | 12 | 11.2 | 53.3 | 6/9 | 336.5 | 47.6 | 3.8 | 39.9 | 39.9 | 45.0 | 3.8 | 39.9 |
| | HB3 724-730 | 5.2 | 53.9 | 12/17 | 18.2 | 58.4 | 14 | 12 | 65.8 | 21.7 | 12.2 | 12.9 |
| 5 | 25 | 217 | 27 | 6/8 | 24.9 | 52.2 | 24.9 | 13.7 | 357.2 | 41.8 | 24.8 | 13.7 |
| | | | Total | 169/268 | 352.8 | 59.9 | 48.2 | 5.6 | 33.1 | 45.2 | 7.7 | 14.8 |

*Dg, s and Ig, s - declination and inclination respectively in the geographic and stratigraphic systems, kg and $\alpha_{95}$ - Fisher dispersion parameter and radius of the 95% confidence cone respectively, n - number of samples used in the calculation, $n_0$ - number of measured samples.

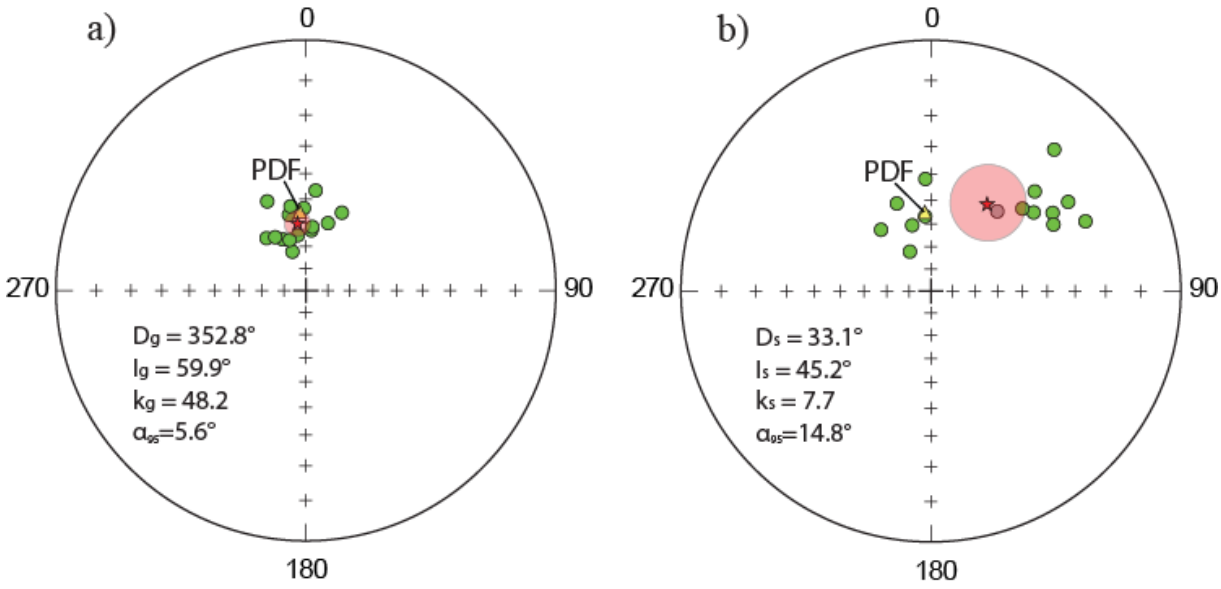


Figure 2.17. Stereographic projection of the low temperature component (LTC) for the Taiyuan Formation in geographic coordinates (a) and in stratigraphic coordinates (b). PDF - present-day geomagnetic field (yellow triangle). The red star is a mean direction drawn from the LTC directions.

McElhinny's (1964) fold test for the LTC mean directions is negative since a ratio of dispersion parameters in geographic and stratigraphic coordinates kg/ks = 6.3 exceeded the critical value of 1.9 at 95% confidence limit and 2.5 at 99% confidence limit. The McFadden's (1990) fold test is also negative: $\xi_1$ = 1.5 for geographic coordinates < critical values 4.5 at 95% confidence limit and 6.3 at 99% confidence limit. While $\xi_1$ = 10.5 for stratigraphic coordinates significantly exceeded the critical values both at 95% and 99% confidence limits. This indicated a post-folding origin of the LTC for the Taiyuan Formation.

The temperature range of the HTC varied between 300 and 525°C (Fig. 2.15, 2.16). The HTC directions were characterized by the north-west declinations for the normal polarity (Fig. 2.15) and south-east declinations for the reverse polarity with steep-intermediate inclination values (Fig. 2.16). After a temperature of 500 - 550°C, the intensity curves demonstrated sharp increases probably corresponding to a formation of new magnetic minerals during the stepwise

demagnetizations (Fig. 2.15, 2.16). The great circles were usually well constrained in the temperature range of 300 - 425°C (Fig. 2.15, 2.16). Great circles were observed both in normal and reverse polarities similar to the HTC directions.

The Taiyuan directions based on PCA analysis and great circles revealed both polarities (Fig. 2.18a, b). Directions were characterized by the northwest and southeast declinations with steep-moderate positive and reverse inclinations. There were five and seven sites of normal and reverse polarities respectively (Fig. 2.18a, b). Generally, each sampling site demonstrated only one polarity except sampling site HB3 (724-730) which yielded three out of eight normal polarity directions. McFadden and McElhinny's (1990) polarity test indicated an angle of 11.4° between the site-mean directions of the normal and reverse polarities. This angle was less than the critical $\gamma = 12.1°$. This revealed a positive reversal test at the 95% confidence limit with classification "C" (McFadden and McElhinny, 1990).

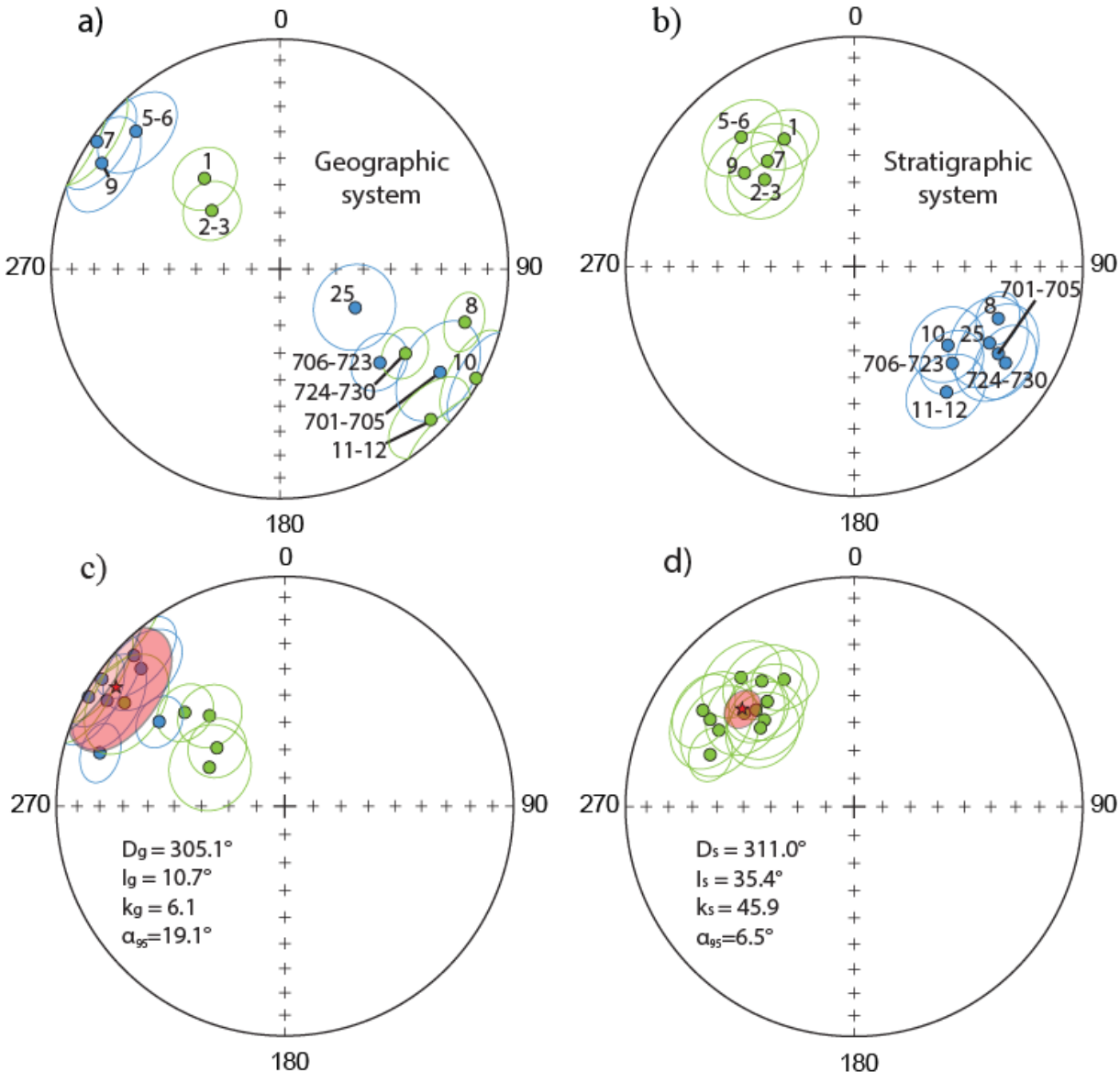


Figure 2.18. Equal-area projections of mean sites for the Taiyuan Formation in geographic coordinates (a, c) and in stratigraphic coordinates (b, d).

The mean directions of the HTC for both polarities was obtained at Dg = 305.1°, Ig = 10.7° ($\alpha_{95}$ = 19.1°, $k_g$ = 6.1, N = 12 sampling sites) in geographic coordinates and at Ds = 311.0°, Is = 35.4° ($\alpha_{95}$ = 6.5°, ks = 45.9) in stratigraphic coordinates. All site-mean HTC directions for the Taiyuan Formation are listed in Table 2.3.

Table 2.3. Summary of results for the high temperature component of the Taiyuan Formation, NCC.

| Locality | Site ID | Strike (°) | Dip (°) | n/$n_0$ | HTC/ circle | N/R | Dg(°) | Ig(°) | Ds(°) | Is(°) | ks | $\alpha_{95}$(°) |
|---|---|---|---|---|---|---|---|---|---|---|---|---|
| 1 | 1 | 288.5 | 16 | 7/16 | 5/2 | 7/0 | 320.1 | 47.4 | 331.1 | 36.8 | 31.4 | 11.2 |
| | 2-3 | 232.7 | 14.6 | 10/36 | 3/7 | 10/0 | 310.5 | 57.9 | 313.9 | 44.7 | 14.9 | 13.5 |
| | HB1 701-705 | 66.5 | 9.6 | 7/17 | 1/6 | 0/7 | 122.7 | -17.8 | 121.1 | -27.3 | 20.0 | 15.7 |
| 2 | 23 | 279.1 | 9.4 | 0/9 | 0/0 | 0 | 0 | 0 | 0 | 0 | 0 | 0 |
| | 24 | 279.1 | 9.4 | 0/6 | 0/0 | 0 | 0 | 0 | 0 | 0 | 0 | 0 |
| | HB2 706-723 | 68.5 | 11.5 | 23/54 | 3/20 | 0/23 | 133.0 | -39.9 | 134.5 | -39.7 | 8.3 | 11.2 |
| 3 | 5-6 | 1.8 | 58.9 | 11/33 | 4/7 | 11/0 | 313.6 | -14.2 | 318.7 | 26.0 | 13.0 | 13.5 |
| | 7 | 1.8 | 58.9 | 7/16 | 2/5 | 7/0 | 304.7 | -3.0 | 320.4 | 40.2 | 24.5 | 13.6 |
| | 8 | 357.2 | 55.3 | 4/9 | 2/2 | 0/4 | 106.0 | 16.9 | 109.8 | -33.5 | 158.5 | 8.5 |
| | 9 | 1.8 | 58.9 | 8/13 | 4/4 | 8/0 | 300.6 | -10.5 | 310.3 | 37.1 | 17.3 | 14.2 |
| | 10 | 11.2 | 53.3 | 6/14 | 4/2 | 0/6 | 119 | 2.1 | 130 | -45.6 | 29.4 | 13.1 |
| | 11-12 | 11.2 | 53.3 | 11/20 | 1/10 | 0/11 | 134.8 | 7.7 | 143.6 | -32.5 | 14.2 | 13.4 |
| | HB3 724-730 | 5.2 | 53.9 | 8/17 | 2/6 | 3/5 | 123.8 | 34.2 | 122.4 | -22.7 | 26.8 | 11.8 |
| 5 | 25 | 217 | 27 | 5/8 | 2/3 | 0/5 | 117.1 | -59.6 | 119.4 | -32.6 | 35.0 | 14.9 |
| | Total ($N/N_0$=17/12): | | | 107/268 | 33/74 | 46/61 | 305.1 | 10.7 | 311 | 35.4 | 45.9 | 6.5 |

*Dg, s and Ig, s - declination and inclination respectively in the geographic and stratigraphic systems, kg and $\alpha_{95}$ - Fisher dispersion parameter and radius of the 95% confidence cone respectively, n - number of samples used in the calculation, $n_0$ - number of measured samples.

Figure 2.18c, d shows that the mean-site directions become more clustered after tilt-corrections (kg = 6.1, $\alpha_{95}$ = 19.1° in geographic coordinates, ks = 45.9, $\alpha_{95}$ = 6.5° in stratigraphic coordinates). McElhinny's (1964) fold test is positive with a dispersion ratio $k_1/k_2$ = 5.6 > critical values of 2.1 and 2.8 at the 95% and 99% confidence limits respectively. McFadden's (1990) fold test (12 mean-sites) was positive since $\xi_1$ = 7.1 in geographic coordinates exceeded the critical value $\xi_{95}$ = 4.0. In the stratigraphic system, the $\xi_{99}$= 5.6, and $\xi_1$ = 2.0 were below the corresponding critical values ($\xi_{99}$ = 5.6). This indicates that the HTC mean direction was acquired before folding and the HTC is the primary magnetization recorded in the Late Carboniferous.

### 2.6.3. Shanxi Formation

For the majority of the Permian samples, the LTC was isolated in the temperature range of 100° - 300°C (Figs. 2.19 and 2.20).

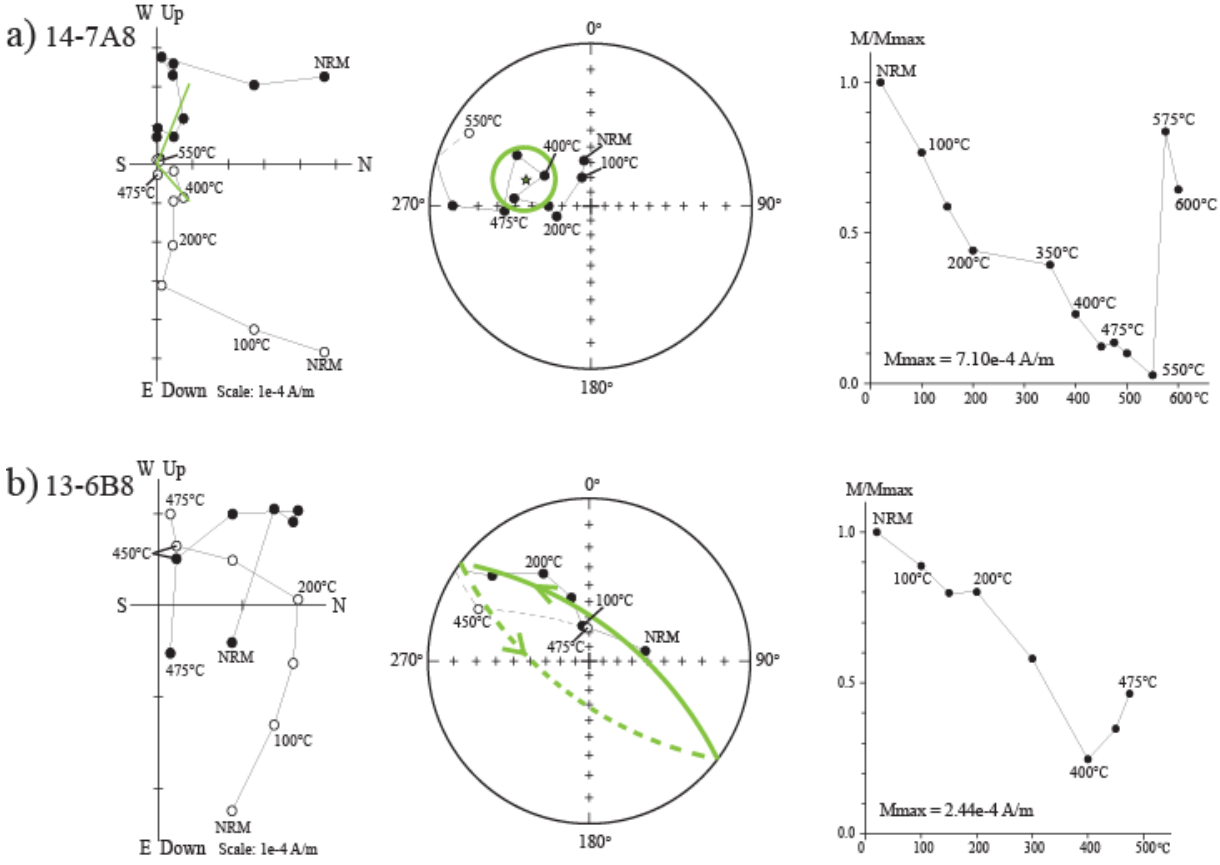


Figure 2.19. Zijderveld diagrams, stereographic projection of the directions for the high temperature component (a) and great circle fitting (b), and step-wise demagnetization plots of the representative Shanxi samples yielded a normal polarity. The green line corresponds to the high temperature component trend along the great circle.

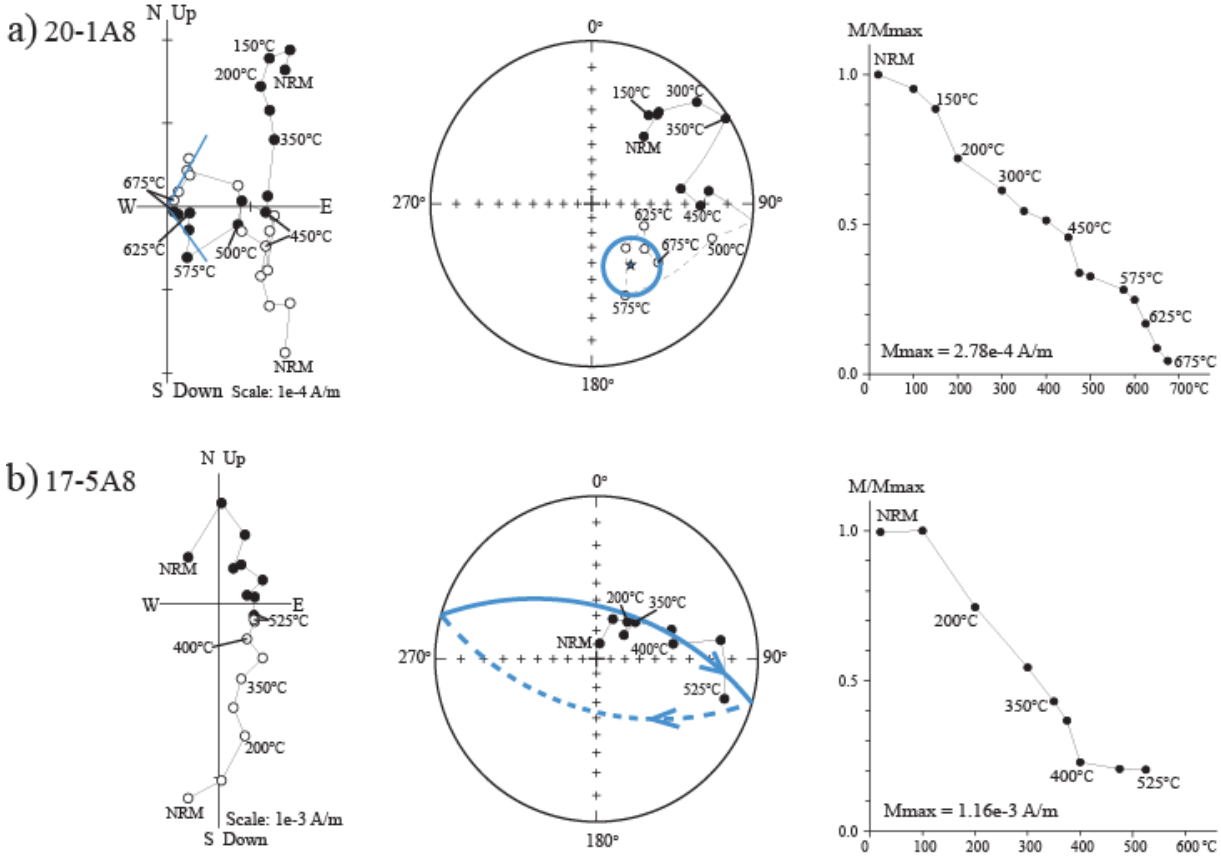


Figure 2.20. Zijderveld diagrams, stereographic projection of the directions for the high temperature component (a) and great circle fitting (b), and step-wise demagnetization plots of the representative Shanxi samples yielded a reverse polarity. The blue line corresponds to the high temperature component trend along the great circle.

A site mean direction for the LTC in the geographic coordinates was obtained at Dg = 356.3°, Ig = 59.2° ($\alpha_{95}$ = 4.5°, n = 99 samples, N = 8 sample sites). The cone of 95% confidence for the LTC mean involved the direction of the present-day field in geographic coordinates that indicated the LTC is a PDF overprint (Fig. 2.21).

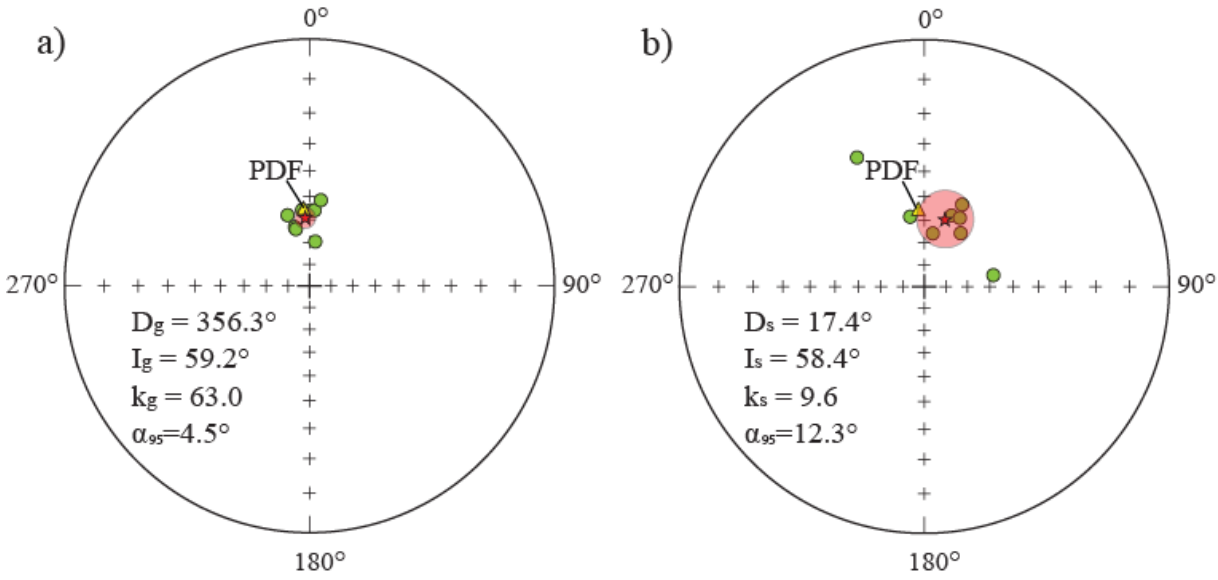


Figure 2.21. Stereographic projections of the low temperature component (LTC) for the Shanxi Formation in geographic coordinates (a) and in stratigraphic coordinates (b). PDF - present-day geomagnetic field (yellow triangle). The red star is a mean direction drawn from the LTC directions.

Table 2.4. Summary of results for the low temperature component of the Shanxi Formation, NCC

| Locality | Site ID | Strike (°) | Dip (°) | n/n$_0$ | Dg (°) | Ig (°) | kg | $\alpha_{95}$ (°) | Ds (°) | Is (°) | ks | $\alpha_{95}$ (°) |
|---|---|---|---|---|---|---|---|---|---|---|---|---|
| 4 | 13 | 33.7 | 33.9 | 8/8 | 7.5 | 69.5 | 20.6 | 12.5 | 80.8 | 58.1 | 20.6 | 12.5 |
| | 14-15 | 35.3 | 20.6 | 15/21 | 1.3 | 55.9 | 14.7 | 10.3 | 34.6 | 60.6 | 14.7 | 10.3 |
| | 16 | 16.7 | 11.7 | 10/15 | 345.8 | 62.4 | 12.2 | 14.4 | 9.2 | 65.4 | 12.2 | 14.4 |
| | 17 | 16.7 | 11.7 | 14/15 | 3.9 | 55.9 | 34.1 | 6.9 | 21.2 | 55.7 | 34.1 | 6.9 |
| | 18 | 14.6 | 14.2 | 11/13 | 7.6 | 51.4 | 26.1 | 9.1 | 25.0 | 49.8 | 26.1 | 9.1 |
| | 19-20 | 274.6 | 5.7 | 14/16 | 346.4 | 63.4 | 15.6 | 10.4 | 348.5 | 57.8 | 15.6 | 10.4 |
| | 21-22 | 7.7 | 29.1 | 13/19 | 342.6 | 56.6 | 17.2 | 10.3 | 27.6 | 55.2 | 17.2 | 10.3 |
| 6 | 26-29 | 215.4 | 36.2 | 14/34 | 354.4 | 55.7 | 11.4 | 12.3 | 332.3 | 28.9 | 13.8 | 11.1 |
| | | Total | | 99/141 | 356.3 | 59.2 | 63 | 4.5 | 17.4 | 58.4 | 9.6 | 12.3 |

*Dg, s and Ig, s - declination and inclination respectively in the geographic and stratigraphic systems, kg and $\alpha_{95}$ - Fisher dispersion parameter and radius of the 95% confidence cone respectively, n - number of samples used in the calculation, $n_0$ - number of measured samples.

McElhinny's (1964) and McFadden's (1990) fold tests for the LTC mean direction were negative at the 95 and 99% confidence levels. McElhinny (1964) fold test yielded a ratio of dispersion

parameters kg/ks = 7.7 exceeding critical values 2.5 and 3.7 (8 sampling sites) at the 95 and 99% confidence levels respectively. McFadden's (1990) fold test (8 sampling sites) yielded $\xi_1 = 0.5$ for the LTC mean in the geographic coordinates that is below the critical values $\xi_{95} = 3.3$ and $\xi_{99} = 4.6$ at the 95 and 99% confidence levels respectively. In stratigraphic coordinates, $\xi_1 = 5.0$ exceeded the critical values at both confidence levels. Negative fold tests indicated a post-folding origin of the Shanxi LTC.

The HTC was isolated in a temperature range between 500 - 575°C and 500 - 675°C (Fig. 2.19a, 2.20a). Samples characterized by an unstable demagnetization were analyzed using a great circle fitting plane in the temperature range from 200 to 500°C (Fig. 2.19b, 2.20b). Five out of six sampling sites revealed south-east directions with the reverse polarity and only one sampling site demonstrated a mixed polarity presented by the south-east and north-west directions (Fig. 2.22).

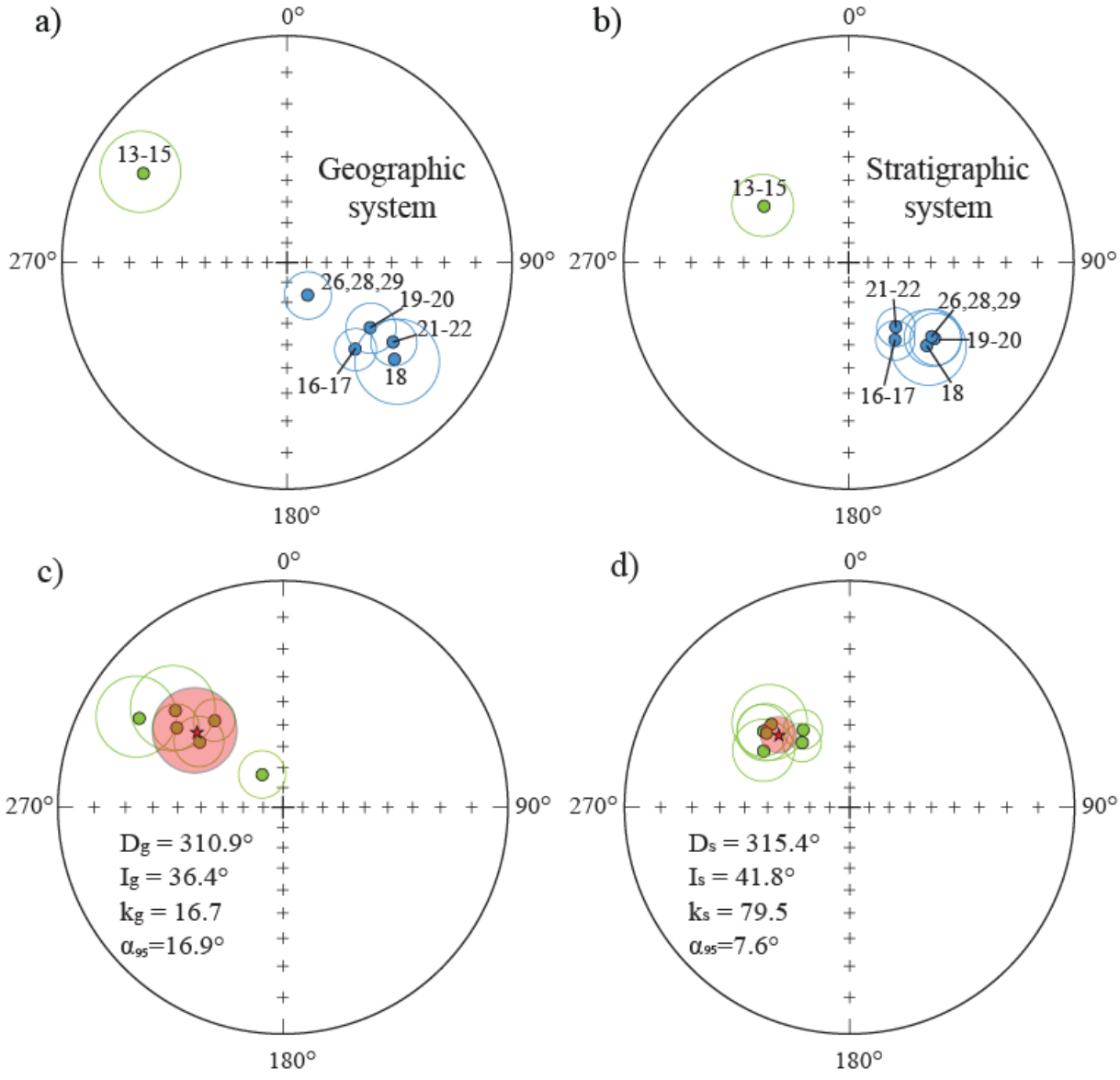


Figure 2.22. Stereographic projections of the site mean for the Shanxi Formation in geographic coordinates (a, c) and in stratigraphic coordinates (b, d).

Since only one sampling site yielded a site mean with a normal polarity the reversal test McFadden & McElhinny's (1990) is indeterminate. An angle between two average gammas was 10.8° which is less than a critical $\gamma = 20.7°$ and resulted in the indeterminate McFadden & McElhinny (1990) reversal test at the 95% confidence limit with a classification "I".

The mean direction for the HTC was at Dg =310.9°, Ig = 36.4°, ks = 16.7, $\alpha_{95}$ = 16.9° in geographic coordinates and Ds = 315.4°, Is = 41.8°, ks = 79.5, $\alpha_{95}$ = 7.6° in stratigraphic coordinates for n = 69 samples, N = 6 sampling sites (Table 2.5).

Table 2.5. Summary of results for the high temperature component of the Shanxi Formation, NCC.

| Locality | Site ID | Strike (°) | Dip (°) | $n/n_0$ | HTC/ circles | N/R | Dg (°) | Ig (°) | Ds (°) | Is (°) | ks | $\alpha_{95}$ (°) |
|---|---|---|---|---|---|---|---|---|---|---|---|---|
| 4 | 13-15 | 34.7 | 25.3 | 13/29 | 2/11 | 6/7 | 301.6 | 16.3 | 303.4 | 41.5 | 11.9 | 13.0 |
| | 16-17 | 16.7 | 11.7 | 17/30 | 1/16 | 0/17 | 141.6 | -38.0 | 148.9 | -46.5 | 19.3 | 8.6 |
| | 18 | 14.6 | 14.2 | 8/13 | 2/6 | 0/8 | 131.8 | -24.7 | 136.6 | -36.4 | 16.6 | 15.1 |
| | 19-20 | 274.6 | 5.7 | 11/16 | 4/7 | 0/11 | 127.9 | -39.8 | 131.3 | -36.1 | 21.7 | 10.4 |
| | 21-22 | 7.7 | 29.1 | 10/19 | 1/9 | 0/10 | 126.7 | -29.1 | 143.6 | -51.1 | 37.4 | 8.7 |
| 6 | 26,28, 29 | 215.4 | 36.2 | 10/26 | 1/9 | 0/10 | 147.5 | -70.6 | 131.6 | -37.5 | 21.3 | 11.6 |
| | 27 | 222.4 | 36.6 | 0/8 | 0/0 | 0/0 | 0 | 0 | 0 | 0 | 0 | 0 |
| | Total ($N/N_0$=6/15) | | | 69/141 | 11/58 | 6/63 | 310.9 | 36.4 | 315.4 | 41.8 | 79.5 | 7.6 |

*Dg, s and Ig, s - declination and inclination respectively in the geographic and stratigraphic systems, kg and $\alpha_{95}$ - Fisher dispersion parameter and radius of the 95% confidence cone respectively, n - number of samples used in the calculation, $n_0$ - number of measured samples.

The site means directions for the HTC were clustered better in stratigraphic coordinates (Fig. 2.22c, d). A ratio of the dispersion parameters ks/kg = 4.8 > a critical value 3.0 (6 mean sampling sites) that yielded the positive McElhinny (1964) test at the 95% confidence limit but inconclusive at the 99% confidence limit (ks/kg = 4.8 < a critical value 4.85). McFadden's (1990) fold test was positive at the 95 and 99% confidence limits and yielded $\xi_1$ = 4.3 in geographic coordinates that exceeded the critical values $\xi_{95}$ = 2.9 and $\xi_{99}$= 3.9 (6 mean sampling sites), and $\xi_1$ = 2.2 lower the critical values in stratigraphic coordinates. The positive fold tests indicated a pre-folding origin of the HTC of the Shanxi samples.

### 2.6.4. Geomagnetic Superchron

The Taiyuan and Shanxi samples yielded both normal and reverse polarities. This raises a question regarding the possible remagnetization of directions drawn from these samples since the time interval of the studied formations corresponds to the dominantly reverse polarity Kiaman Superchron. The Kiaman Superchron lasted from ~318 to 269 Ma which includes the Late Carboniferous to early Middle Permian (Hounslow, 2022; Hounslow and Balabanov, 2018; references therein). However, the recent reassessment of the available magnetostratigraphic datasets suggested that the Kiaman Superchron could have a few normal polarity short intervals (Hounslow, 2022; Hounslow and Balabanov, 2018).

In this study, the samples that yielded the normal polarity were collected at the bottom of the Taiyuan and Shanxi Formations. In locality 3 sandstone samples collected in the lower part of the Taiyuan Formation (Fig. 2.3) yielded zircon ages around 306 - 302 Ma. This indicates that the age of the corresponding deposits is younger than 306 - 302 Ma.

The time interval corresponding to 306 - 302 Ma includes a short-term normal polarity (Fig. 2.5) in the magnetostratigraphic scale published in Hounslow (2022). Thus, the samples collected from the bottom of the Taiyuan Formation in locality 3 could record the normal polarity event during the Kiaman Superchron. The normal polarity short interval at approximately the same stratigraphic level as in locality 3 was obtained at the sampling sites 1-3 of locality 1. The Middle Ordovician sediments of site 4 of locality 1 also preserved the normal polarity. The Middle Ordovician is characterized by a normal-reverse polarity pattern (Hounslow et al., 2021) with relatively long normal polarity intervals that were well registered in the previous paleomagnetic work in northern

China (Huang et al., 1999). The Ordovician result suggests that the stratigraphic section has not been subjected to magnetic overprinting and that the normal polarity event recorded in the Taiyuan Formation is a primary magnetic record.

The Shanxi samples (13-15 sampling sites, Fig. 2.3) also showed the HTC directions of normal polarity in contrast to other reverse polarity sampling sites. The zircon studies of sandstones collected from the bottom of the Shanxi Formation within locality 4 yielded low-quality results that did not allow us to conclude the time constraints of the exposed sequence. But in accordance with the magnetostratigraphic scale in Hounslow and Balabanov (2018), there are two short-term normal polarities within the time interval of 299 - 297 Ma. This time interval coincides with the stratigraphic boundary between the Taiyuan and Shanxi Formations defined in Shen et al. (2021) (Fig. 2.5). Hence, there is a high likelihood of a short record of normal polarity by the Shanxi samples composing the bottom of this formation.

It should be also noted that the normal polarity directions were previously obtained from the Taiyuan Formation (Wu et al., 1990) and from the Lower Permian volcanic rocks (~313 - 291 Ma) (Zhang et al., 2021a).

### 2.7. Discussion of the Late Carboniferous and Early Permian paleomagnetic poles

We obtained the new Late Carboniferous and Early Permian paleomagnetic poles at the average locality positions 44.1°N/13.1°E ($A_{95}$ = 5.7°, dp/dm = 7.5°/4.3°, N = 12 sites) and at 49.9°N/15.8°E ($A_{95}$ = 7.3°, dp/dm = 9.3°/5.7°, N = 6 sites) respectively. The 95% cones of confidence for the Late Carboniferous and Early Permian paleomagnetic poles, obtained using the PSV statistical model of Deenen et al. (2011), lie within a reliability envelope between the $A_{95min}$ = 4.4° and $A_{95max}$ =

17.1° and $A_{95min}$ = 5.8°, $A_{95min}$ = 26.5° respectively. The poles correspond to the fossil-determined age of the sediments (Feng et al., 2008; Shen et al., 2021) which is additionally constrained by our zircon study; we applied stepwise thermal demagnetization and up-to-date statistical analysis; the fold tests are positive; the study localities are situated in the center of the NCC within the COB; the reversal tests are positive. Our new poles are the first Late Carboniferous and Early Permian poles which meet all seven criteria of reliability outlined in Meert et al. (2020).

Inclination shallowing is common in sediments, and it affects calculations of both paleomagnetic pole and paleolatitude and therefore has to be taken into account. Torsvik et al. (2012) suggested applying a flattening factor (*f*) of 0.6 for the global plate reconstructions, and Van der Voo et al. (2015) and Wu et al. (2017) used this *f* value for paleomagnetic reconstructions of East Asia since the Late Paleozoic. However, Zhang et al. (2021a, b) stated that using *f* = 0.7 allowed achieving better consistency between paleomagnetic poles from the coeval igneous and clastic rocks for both China Cratons, therefore we use *f* of 0.7 in our study.

We listed all NCC Late Carboniferous and Early Permian paleomagnetic poles presented in the further discussion in Table 2.6. We illustrated all paleomagnetic poles and paleolatitudes for the NCC from the Early Carboniferous to Cretaceous without an application of flattening factor (Fig. 2.23) and with *f* of 0.7 applied to the clastic rocks (Fig. 2.24). Further, we discuss only poles and paleolatitudes that incorporate *f* = 0.7.

Table 2.6. Late Carboniferous and Early Permian paleomagnetic poles from the NCC.

| Tectonic unit | Lithology | Site latitude (N°) | Site Longitude (E°) | Pole latitude (N°) | Pole longitude (E°) | $A_{95}$ (°) | N/n | Paleolat (N°) | Paleolat (N°) with f = 0.7 | RI | Reference |
|---|---|---|---|---|---|---|---|---|---|---|---|
| **Late Carboniferous** | | | | | | | | | | | |
| NCC | Sedimentary rocks, Taiyuan Fr. | 36.6 | 111.1 | 44.1 | 13.1 | 5.7 | 12/ 107 | 19.6 | 26.9 | 1234 567 (7) | This study |
| Alxa Block | Sedimentary rocks, Taiyuan Fr. | 37.2 | 105.4 | 33.3 | 10.2 | 13.7 | -/11 | 15.6 | 21.7 | 1-3- 5-7 (4) | Huang et al. (2001) |
| NCC | Sedimentary rocks, Taiyuan Fr. | 35.5 | 110.2 | 30 | 11.9 | 4.6 | 3/15 | 10.1 | 14.3 | 1--- 5-7 (3) | Wu et al. (1990) |
| NCC | Sedimentary rocks, Taiyuan Fr. | 37.9 | 112.4 | 70.4 | 289.6 | 12.7 | 6/- | 18.3 | 25.3 | 1--- 5-7 (3) | Lin et al. (1984) |
| **Early Permian** | | | | | | | | | | | |
| NCC | Sedimentary rocks, Shanxi Fr. | 36.1 | 111.1 | 49.9 | 15.8 | 7.3 | 6/69 | 24.1 | 32.5 | 1234 567 (7) | This study |
| NCC | Sedimentary rocks, Lower Shihezi Fr. | 35.5 | 110.2 | 33.3 | 18.2 | 4.3 | -/33 | 16.3 | 22.8 | 1--- 5-7 (3) | Wu et al. (1990) |

| Tectonic unit | Lithology | Site latitude (N°) | Site Longitude (E°) | Pole latitude (N°) | Pole longitude (E°) | $A_{95}$ (°) | N/n | Paleolat (N°) | Paleolat (N°) with f = 0.7 | RI | Reference |
|---|---|---|---|---|---|---|---|---|---|---|---|
| NCC | Sedimentary rocks | 35.5 | 110.3 | 47 | 359.2 | 4.5 | 4/- | 13.3 | 18.6 | 123-5-7 (5) | Ma et al. (1993) |
| NCC | Sedimentary rocks, Lower Shihezi Fr. | 37.8 | 112.3 | 20.9 | 1.4 | 8.7 | -/11 | -2.6 | -3.7 | 1---5-7 (3) | Embleton et al. (1996) |
| The northern margin of the NCC | Volcanic rocks, Sanmianjing and Elitu Fr. | 42 | 113.9 | 66.2 | 328.1 | 4.1 | 24/- | 20.4 | - | 1234 5-7 (6) | Zhang et al. (2018) |

*$A_{95}$ - the radius of a 95% cone confidence, N/n – the number of sites/number of samples; RI - reliability index (Meert et al., 2020): 1, well-determined rock age and a presumption that magnetization is the same age; 2, demagnetization techniques and statistical analysis; 3, rock magnetic studies, 4, field tests; 5, tectonic coherence relatively plate or block; 6, positive reversal test; 7, no remagnetization. Paleolatitudes (paleolat) are calculated at a reference point corresponding to the sampling site of each pole.

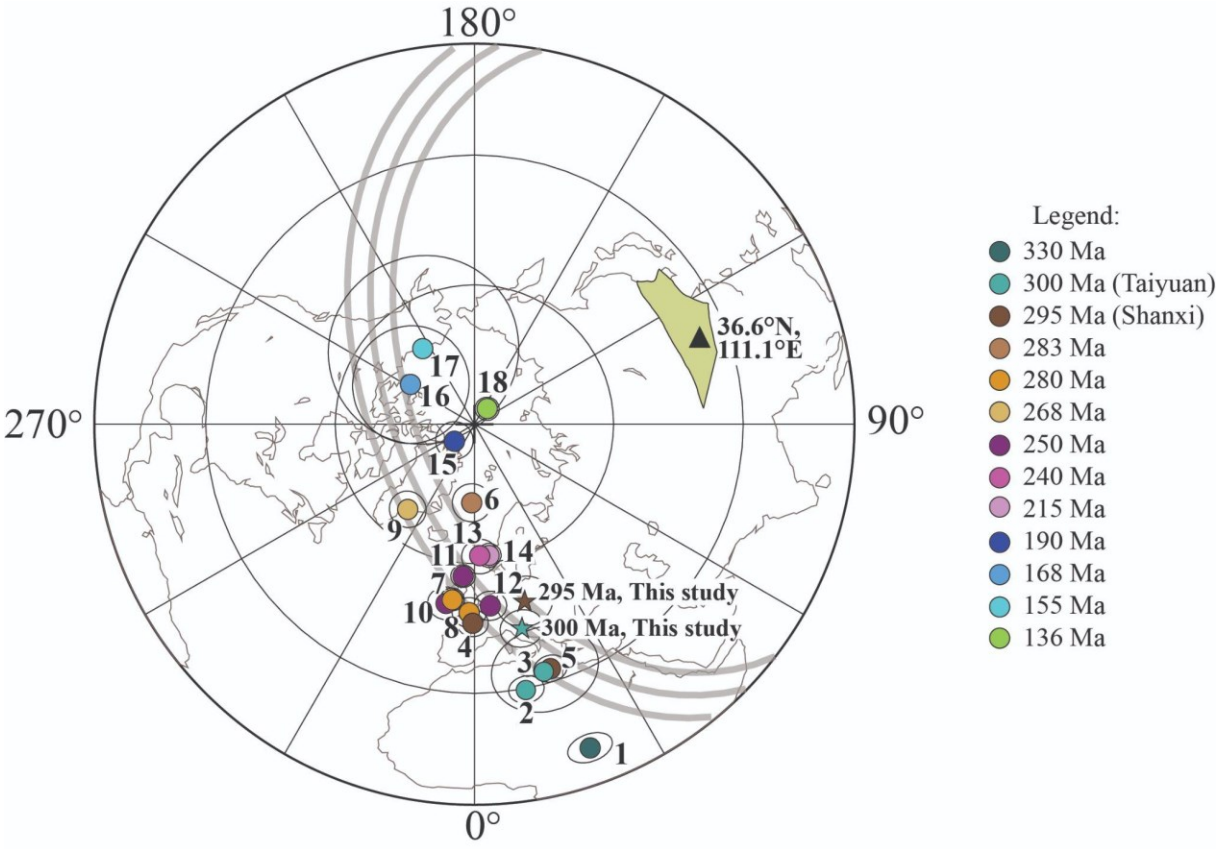


Figure 2.23. Equal area projection of the Carboniferous - Early Cretaceous paleomagnetic poles for the NCC without $f = 0.7$. References: 1. Huang et al. (2001); 2. Wu et al. (1990); 3. Huang et al. (2001); 4. Ma et al. (1993); 5. Wu et al. (1990); 6. Zhang et al. (2018), recalculated; 7. Embleton et al. (1996); 8. Ma et al. (1993); 9. Zhang et al. (2018), recalculated; 10. Embleton et al. (1996); 11. Ma et al. (1993); 12. Huang et al. (2005); 13. $T_2$, mean of Fang et al. (1992), Ma et al. (1993), Tan et al. (1995), Yang et al. (1991); 14. $T_3$, mean of Ma et al. (1993) and Yang et al. (1991); 15 $J_1$, mean of Uno and Huang (2003); 16. $J_2$, mean of Fang et al. (1988), Gilder and Courtillot (1997), and Yang et al. (1992); 17. $J_3$, mean of Gilder and Courtillot (1997) (volcanoclastic rocks), Pei et al. (2011) (volcanic rocks), and Ren et al. (2016) (volcanic rocks); 18. $K_1$, mean of Zhu et al. (2002) and Zhu et al. (2004).

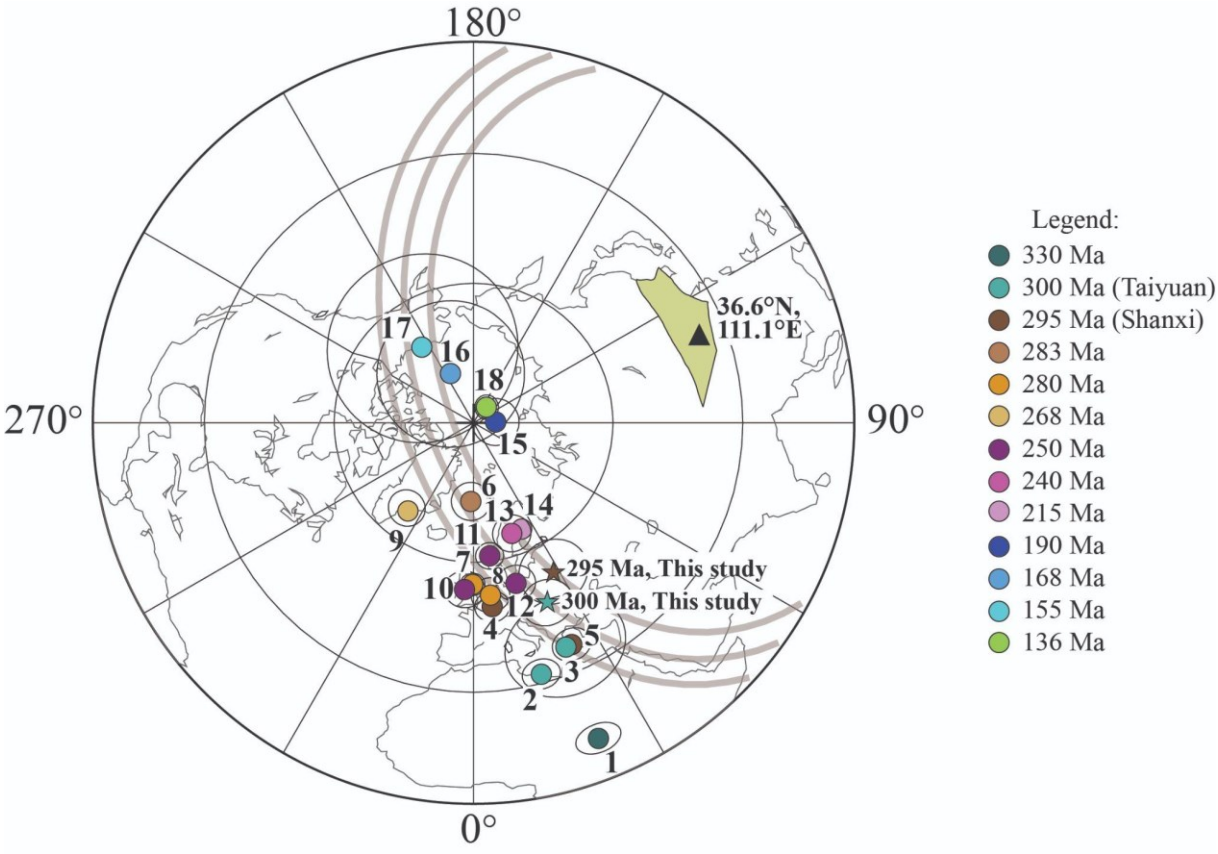


Figure 2.24. Equal area projection of the Carboniferous - Early Cretaceous paleomagnetic poles for the NCC with $f$ = 0.7. References: 1. Huang et al. (2001); 2. Wu et al. (1990); 3. Huang et al. (2001); 4. Ma et al. (1993); 5. Wu et al. (1990); 6. Zhang et al. (2018), recalculated; 7. Embleton et al. (1996); 8. Ma et al. (1993); 9. Zhang et al. (2018), recalculated; 10. Embleton et al. (1996); 11. Ma et al. (1993); 12. Huang et al. (2005); 13. $T_2$, mean of Fang et al. (1992), Ma et al. (1993), Tan et al. (1995), Yang et al. (1991); 14. $T_3$, mean of Ma et al. (1993) and Yang et al. (1991); 15 $J_1$, mean of Uno and Huang (2003); 16. $J_2$, mean of Fang et al. (1988), Gilder and Courtillot (1997), and Yang et al. (1992); 17. $J_3$, mean of Gilder and Courtillot (1997) (volcanoclastic rocks), Pei et al. (2011) (volcanic rocks), and Ren et al. (2016) (volcanic rocks); 18. $K_1$, mean of Zhu et al. (2002) and Zhu et al. (2004).

### 2.7.1. The Late Carboniferous paleomagnetic poles of the NCC from previous studies

There are two Late Carboniferous paleomagnetic poles that have been used to constrain the paleoposition of the NCC (Huang et al., 2001; Yuan and Yang, 2015). Both poles were obtained from the Alxa Block (Fig. 2.1). However, Yuan and Yang (2015) suggested that the Alxa Block was not amalgamated with the NCC by the Late Permian. Notably, Yuan and Yang (2015) derived their Late Carboniferous pole from the middle temperature component which resembled the Early-

Middle Carboniferous high temperature component reported by Huang et al. (2001) from the Alxa Block. Therefore, the pole from Yuan and Yang (2015) cannot be used as a solid proof for the Alxa Block detachment from the NCC.

During the last twenty years, the Late Carboniferous pole of Huang et al. (2001) was widely used as an anchor pole in paleogeographic reconstructions of PAO in the Late Paleozoic (Domeier and Torsvik, 2014; Huang et al., 2018; Zhang et al., 2021b). However, this pole has a low number of samples, lacks field tests and rock-magnetic analysis, therefore it was not considered in some reconstructions (Torsvik and Cocks, 2013). Fig. 2.24 shows that our Late Carboniferous pole lies within a large cone of confidence of the pole from Huang et al. (2001).

Another paleomagnetic pole from Wu et al. (1990) was calculated from 15 samples collected from the COB. The absence of stepwise demagnetizations, principal component analysis, field tests, and rock magnetic measurements together reduce the reliability of this pole. Figure 2.25 illustrates that the pole from Wu et al. (1990) yields a much lower paleolatitude for the NCC compared to the paleolatitudes obtained in our study and in Huang et al. (2001).

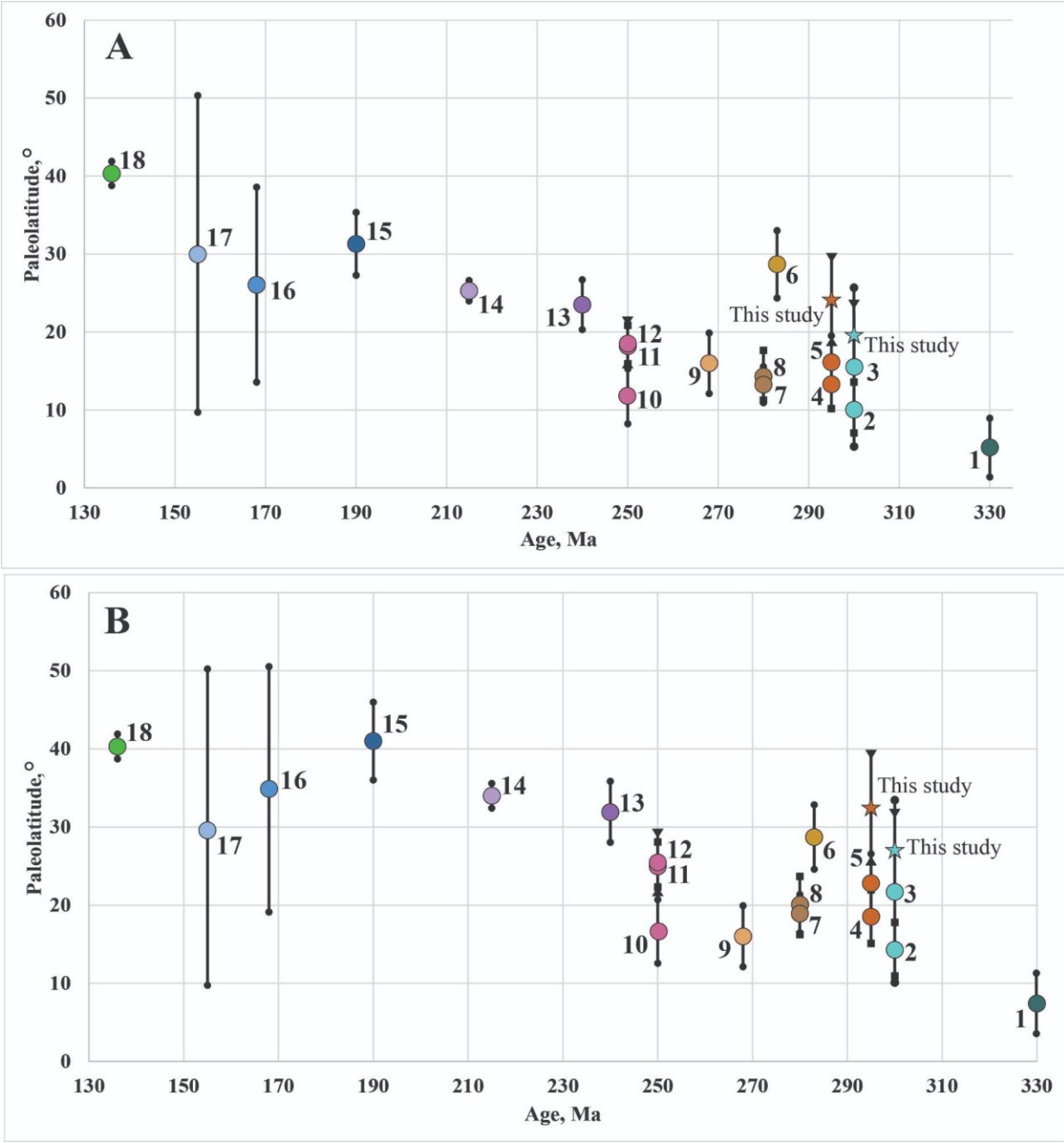


Figure 2.25. Carboniferous - Early Cretaceous paleolatitudes for the NCC without $f = 0.7$ (A) and after $f = 0.7$ (B). References: 1. Huang et al. (2001); 2. Wu et al. (1990); 3. Huang et al. (2001); 4. Ma et al. (1993); 5. Wu et al. (1990); 6. Zhang et al. (2018), recalculated; 7. Embleton et al. (1996); 8. Ma et al. (1993); 9. Zhang et al. (2018), recalculated; 10. Embleton et al. (1996); 11. Ma et al. (1993); 12. Huang et al. (2005); 13. $T_2$, mean of Fang et al. (1992), Ma et al. (1993), Tan et al. (1995), Yang et al. (1991); 14. $T_3$, mean of Ma et al. (1993) and Yang et al. (1991); 15 $J_1$, mean of Uno and Huang (2003); 16. $J_2$, mean of Fang et al. (1988), Gilder and Courtillot (1997), and Yang et al. (1992); 17. $J_3$, mean of Gilder and Courtillot (1997) (volcanoclastic rocks), Pei et al. (2011) (volcanic rocks), and Ren et al. (2016) (volcanic rocks); 18. $K_1$, mean of Zhu et al. (2002) and Zhu et al. (2004).

Lin et al. (1984) published the pole from the Taiyuan limestones. The study does not have any field tests and rock magnetic studies or stepwise demagnetizations. In addition, the authors noted that their samples were likely remagnetized therefore we excluded this pole from further discussion.

The NCC was located at 19.6°N ± 4.3° without the application of *f* and at 26.9°N ± 5.2° after an appliance of $f = 0.7$ (Fig. 2.25a, b). The paleolatitude obtained in our study is higher by five degrees than the reported paleolatitude from Huang et al. (2001).

### 2.7.2. The Early Permian poles from the previous studies

All published Early Permian paleomagnetic poles for the NCC are listed in Table 2.6. Due to the absence of field tests and small numbers of samples, the paleomagnetic poles from Wu et al. (1990), Ma et al. (1993), and Embleton et al. (1996) have a low reliability index (RI) of Meert et al. (2020) and therefore we did not use the poles in our paleogeographic reconstructions (Table 2.6).

The most recent pole from Zhang et al. (2018) has the highest RI among the Early Permian poles from the NCC. This pole was calculated from a direction mean derived from the Early and Middle Permian formations. Since samples in Zhang et al. (2018) were collected from the craton margin (Fig. 2.1), paleomagnetic declinations drawn from these samples could be affected by a rotation because the northern margin of the NCC was subjected to the collision between the NCC and adjacent Inner Mongolia. We recalculated the paleomagnetic poles from the directions provided in Zhang et al. (2018) for the Early and Middle Permian independently to represent their particular age intervals. Fig. 2.24 shows that these poles are significantly rotated relatively to the coeval and

Carboniferous poles that could be attributed to the folding of the northern margin of the NCC. The Early Permian paleolatitude obtained in our study lies within the limit confidence of the coeval paleolatitude from Zhang et al. (2018) (Fig. 2.25b).

The Middle Permian paleolatitude from Zhang et al. (2018) almost coincides with the coeval paleolatitudes calculated in Embleton et al. (1996) and Ma et al. (1993). Considering that the paleomagnetic poles in Zhang et al. (2018) were calculated from volcanic rocks while the poles in Embleton et al. (1996) and Ma et al. (1993) were obtained from clastic rocks that we corrected using $f = 0.7$ (Fig. 2.25b). At the same time, our pole and some other Permian poles are located close to the Triassic group of poles (Fig. 2.24). Therefore, we cannot exclude that the paleomagnetic directions derived from the Shanxi Formation could be subjected to Triassic remagnetization. However, the probability of such an event is low because the folding of Paleozoic-Early Mesozoic strata within the COB took place after the Middle Triassic (Zhang et al., 2020; Zhao et al., 2020; reference therein).

The Early Permian paleolatitude of our study is 24.1°N ± 5.7° without correction for the flattening, and 32.5°N ± 8.6° after application of $f = 0.7$. The paleolatitude coincides with the Early Permian paleolatitude (28.7°N ± 4.3°) from Zhang et al. (2018) which was recalculated in our study. This paleolatitude was derived from directions obtained from volcanic rocks. It places the NCC on higher paleolatitudes than in previous reconstructions.

## 2.8. Late Carboniferous and Early Permian paleogeographic reconstructions of the North China Craton

According to our new paleomagnetic results, the NCC moved in the Late Carboniferous and Early Permian from 26.9°N ± 4.3° to 32.5°N ± 5.7° considering the flattening factor of 0.7.

Construction of the APWP for the NCC for the Middle-Late Paleozoic interval is complicated due to the lack of paleomagnetic data. Our Late Carboniferous pole together with the Early-Middle Carboniferous pole from Huang et al. (2001) indicate that the NCC sharply moved northward from the subequatorial latitude of ~7°N in the Early-Middle Carboniferous (Huang et al. 2001) to ~27°N in the Late Carboniferous (this study) (Fig. 2.25b). These paleolatitudes mean that the velocity of the NCC motion between 330 and 300 Ma was ~7.4 cm/yr. The obtained velocity is close to the mean absolute plate motion velocities calculated for the Mesozoic Era which vary between ~4 and 9.5 cm/yr (Müller et al., 2016).

The Late Paleozoic reconstruction of the Amuria, Altai-Gobi Zone (AGZ), Mandalovoo terrane, and NUT is complicated because of a lack of coeval paleomagnetic and tectonic data. Geochronological and tectonic studies (Baatar, 2001; Badarch et al., 2002; Guy et al., 2014) proposed that all these tectonic units developed as an accretionary wedge with joint volcanic island arcs attributed to the subduction of PAO since the Ordovician - Devonian. Amuria, Altai-Gobi Zone, and Mandalovoo terrane are thought to be finally accreted by the Late Paleozoic - Mesozoic (Badarch et al., 2002). Thus, in our paleogeographic reconstruction, we assume that the Late Paleozoic latitudes of these tectonic units should be consistent with each other.

The most recent paleomagnetic poles with a high reliability index were reported in Zhang et al. (2021a) and Zhang et al. (2021b) for the Songliao Block and NUT respectively. We used these poles to constrain a paleoposition of the composite Amuria and adjacent areas in the Late Carboniferous - Early Permian. Both Zhang et al (2021a) and Zhang et al. (2021b) showed that the Amuria, Mandalovoo terrane, Inner Mongolia, and Songliao Block constituted one large composite block ~300 Ma located at 33 - 37°N. The Carboniferous and Early Permian paleomagnetic poles obtained from volcanic rocks of the AGZ in Bazhenov et al. (2016) and Kovalenko and Chernov (2008) yielded a paleolatitude range of ~ 47 - 58°N showing the proximity of the AGZ to the Tuva-Mongolia terrane and Siberian continent. Therefore, in our Late Carboniferous - Early Permian reconstruction we placed all the Amuria, AGZ, Inner Mongolia, and adjacent areas as a union tectonic composite at 33 - 37°N (Fig. 2.26).

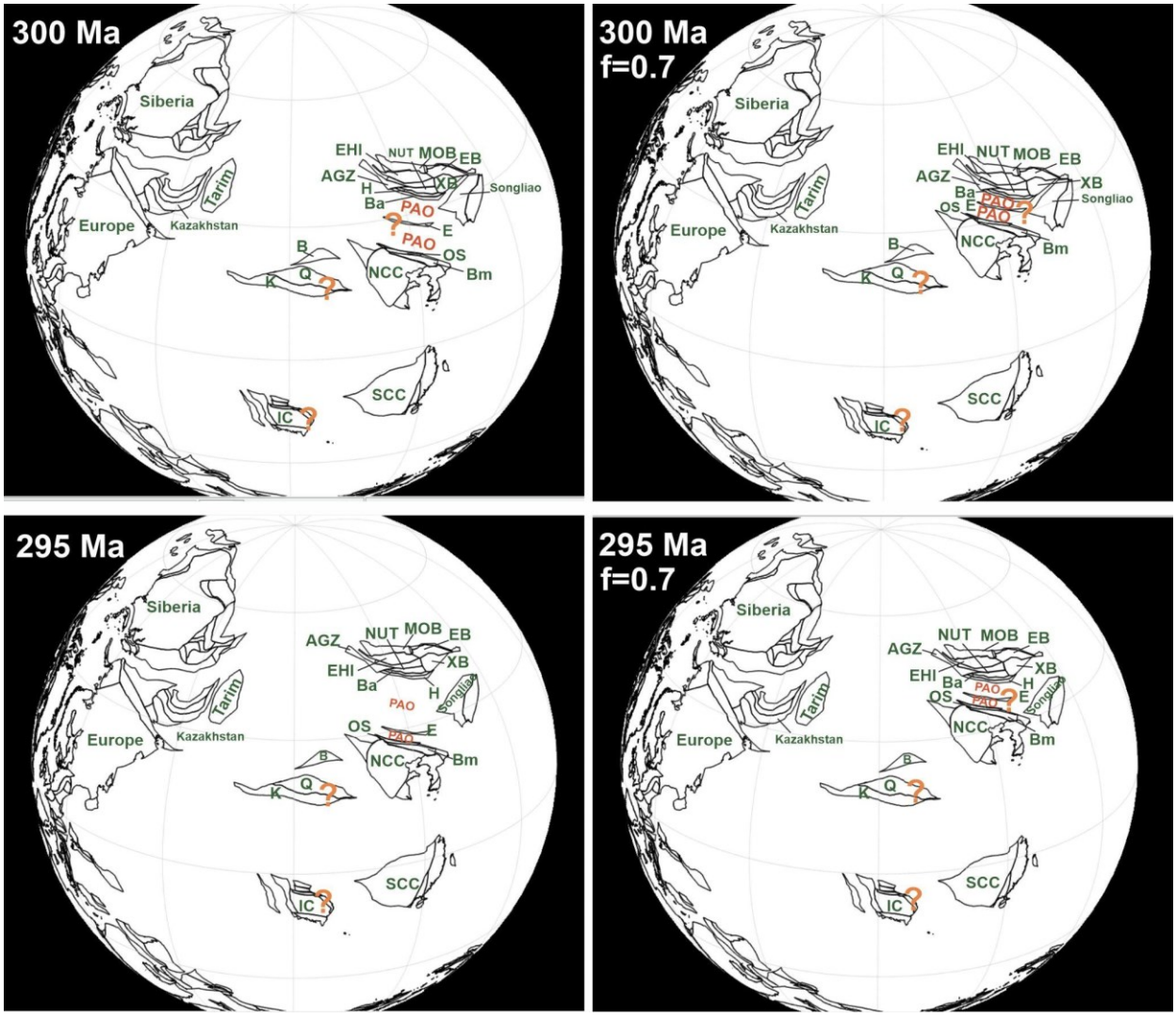


Figure 2.26. Simplified paleogeography reconstruction of East Asia in the Late Carboniferous - Early Permian. Paleopositions of Siberia, Baltica, and Tarim are from Young et al. (2019); paleoposition of the SCC (South China Craton) is from Huang et al. (2018); paleoposition of NUT is based on the paleomagnetic poles from Zhang et al. (2021); paleoposition of Songliao Block is based on a paleomagnetic pole from Zhang et al. (2021); paleoposition of Beishan Orogenic Complex is based on a paleomagnetic pole from Xu et al. (2019); orange question-mark - undefined paleoposition. AGZ - Altai - Gobi Zone, Bm - Bainaimiao Arc Complex, Ba - Baolidao Accretion Complex, EB - Erguna Block, EHI - Ereendavaa-Herlen-Idermeg, E - Erdaojing Accretion Complex, H - Hegenshan Accretion Complex, K - Kunlun, MOB - Mongol-Okhotsk Belt, NUT - Nuhetdavaa-Uliastai fore/backarc terrane, OS - Ondor Sum Accretion Complex, Q - Qilian Orogenic Complex, XB - Xing'an Block.

Zhang et al. (2021b) reported the Early Permian paleomagnetic result from the volcanic rocks that allocate the paleolatitude for the NUT at 43.6 ± 5.5°N. It implies that the NUT and the other

attached tectonic units such as the Inner Mongolia and Amuria moved northward from ~37.2°N in the Late Carboniferous to 43.6°N in the Early Permian.

Geochronological and geochemical studies proposed that the Erguna, Xing'an, and Songliao Blocks were separated by the oceanic branches of the northeast PAO in the Paleozoic Era (Feng et al., 2018, and the references therein). Closure of PAO branches started with a subsequent amalgamation between the Erguna and Xing'an Blocks in the Early Paleozoic and proceeded by the welding with the Songliao Block in the Late Paleozoic - Early Mesozoic time (Feng et al., 2018; Fu et al., 2021; Gou et al., 2019; Ma et al., 2019; Yang et al., 2019; Zhao et al., 2019; and references therein). Therefore, we showed in our reconstruction that the eastern branch of PAO existed between the Erguna-Xing'an and Songliao Blocks in the Late Carboniferous - Early Permian (Fig. 2.26).

There is no reliable Late Carboniferous - Early Permian paleomagnetic data from the Inner Mongolian blocks. Xiao et al. (2018) suggested that PAO branches separated these accretionary complexes before the Middle Permian. Based on geochronological and geochemical studies, Wei et al. (2018, and references therein) proposed that the Hegenshan ophiolites were formed from the Middle Carboniferous to the Early Permian. It implies that the Hegenshan arc complex could be attached to the NUT by the Late Carboniferous (Fig. 2.26).

Xu et al. (2019) reported the Early Permian paleomagnetic pole from the Beishan Orogenic complex (BOC) with a paleolatitude at 33.7°N ± 1.8° (with $f = 0.7$). It implies that the BOC was located at similar paleolatitudes with the NCC (Fig. 2.25).

Reconstruction of all parts constituting East Asia using our new paleolatitudes shows that the width of PAO in ~300 - 295 Ma varied around 650 - 620 km when applying the flattening factor to all paleomagnetic data obtained from sediments, or around 1200 - 1600 km without the application of flattening factor (Fig. 2.25).

# Chapter 3: Paleomagnetism of the Ediacaran - Early Cambrian sediments for the South China Craton

## 3.1. Introduction

The paleogeographic position of the South China Craton (SCC) is the key to Neoproterozoic - Early Paleozoic global plate tectonic reconstructions. This period is characterized by the break-up of the supercontinent Rodinia, the formation of Gondwana, rapid motions of the continents, the emergence of Cambrian animals, and significant changes in the Earth's atmosphere (Cawood et al, 2016; Evans, 2009; Li et al., 2008; Xia et al., 2018; Zhu et al., 2007). The SCC position in the Neoproterozoic - Early Cambrian period with regard to the other continents remains unclear (Xia et al., 2018; Zhang et al., 2015; references herein).

The debates regarding the SCC position revolve around whether the SCC was an internal part of Rodinia or if this craton was located on Rodinia's periphery. Li et al. (2008) proposed that the SCC was located between the Laurentia (eastern part of Rodinia) and Australia. This model originated from the similarity of volcanic and detrital rocks in the eastern part of the SCC and the western part of Australia. Evans (2000) suggested that the SCC was separated from Australia by India on the western margin of Australia. Macouin et al. (2004) and Yang et al. (2004) placed the SCC between India and Australia westward from Australia's margin in the Late Neoproterozoic - Early Paleozoic on the basis of paleomagnetic data. The Cawood et al. (2016) reconstruction of Rodinia's break-up did not include the SCC.

The major difficulty for the Neoproterozoic - Early Paleozoic complete global reconstruction is a lack of paleomagnetic data from the SCC. There are consistent paleomagnetic poles for the Middle Neoproterozoic reported by Evans et al. (2000), Zhang et al. (2013), and Zhang and Piper (1997).

But for the Late Neoproterozoic (Ediacaran) and Early Cambrian, there are only two Early Ediacaran paleomagnetic poles of Macouin et al. (2004) and Zhang et al. (2015). These poles yield controversial paleolatitudes for the SCC at ~3.3 ± 4.6°N (Macouin et al., 2004) and 24.4 ±5 .6°N (Zhang et al., 2015). It implies that one or both poles was subjected to remagnetization at younger ages. Gong et al. (2017) reported the remagnetized paleomagnetic directions from the Early Ediacaran rocks that matched with the Cretaceous paleomagnetic directions from the SCC.

The Middle Cambrian (520 - 510 Ma) paleomagnetic pole yielded a paleolatitude around 8°N (Yang et al., 2004). There is a time gap of 30 Ma in the paleomagnetic dataset that corresponds to the Ediacaran - Early Cambrian. Therefore, our study's primary goal is to obtain reliable paleomagnetic data for this interval. We sampled rocks from the northwestern part of the SCC whereas the previous Neoproterozoic poles were obtained from the rocks in the central part of the SCC along the Jiangnan Orogeny orogenic belt.

Here we report new paleomagnetic poles from the Doushantou and Dengying Formations (Ediacaran) and Xiaoping, ShuiJingtuo, Shipai, and Tianheban Formations (Early Cambrian). The results of Chapter 3 are preliminary because we plan to demagnetize more samples in order to obtain statistically plausible results that can be published.

### 3.2. Geological background

The SCC is separated from the NCC by the Qinling-Dabie Orogen (QDO) in the north and is flanked by the Qiangtang-Sanjiang Orogenic System (QSOS) in the northwest (Fig.3.1a). The Yangtze Block in the northwest and the Cathaysia Block in the southeast constitute the SCC (Fig. 3.2b).

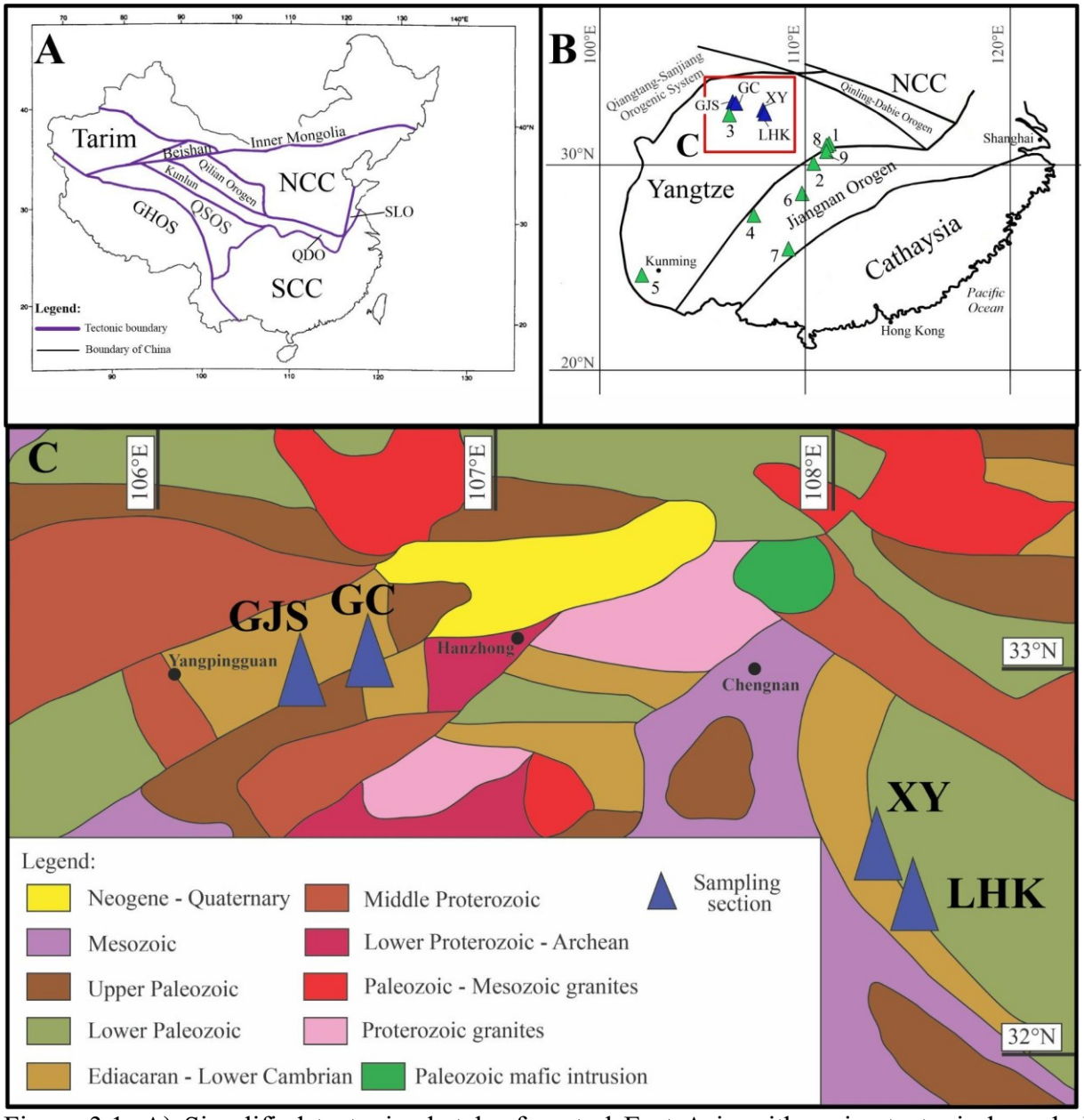


Figure 3.1. A) Simplified tectonic sketch of central East Asia with major tectonic boundaries (Modified after Zhang and Piper (1997)). GHOS - Gangdese–Himalaya orogenic system; NCC - North China Craton; SCC -South China Craton; SLO - Sulu orogenic orogen; QDO - Qinling-Dabie orogen; QSOS - Qiangtang-Sanjiang orogenic system. B) Simplified tectonic map of the SCC. Modified after Zhao (2015). Blue triangles show sampling localities. GC - Gangchang section; GJS - Gaojiashan section; LHK - Lianghekou section;XY - Xiaoyang section. Green triangles show sampling localities from studies: 1) Evans et al. (2000); 2) Macouin et al. (2004); 3) Yang et al. (2004); 4,5) Zhang and Piper (1997); 6,7) Zhang et al. (2013); 8,9) Zhang et al. (2015). C) Simplified geological map of the study area with sampling sections (modified after Chen, 2004)

Amalgamation of the two blocks is thought to be attributed to the closure of a paleoocean between the Yangtze Block and Cathaysia Block. The paleoocean subducted beneath the Yangtze Block (Li et al., 2020; Xia et al. 2018) gave rise to the Jiangnan Orogen (Li et al., 2020, and the references therein). The timing of collision is constrained to ~830 Ma based on geochemical data (Li et al., 2020; Xia et al., 2018; Yao et al., 2019).

The basement of the Yangtze Block consists of the Archean granodioritic–trondhjemitic gneisses, trondhjemites, and Paleoproterozoic metasediments and magmatic rocks (Yao et al., 2015). The poorly exposed basement of Cathaysia Block consists of Paleoproterozoic - Neoproterozoic metamorphosed granitoids and supracrustal rocks (Li et al., 2014; Yao et al., 2015). Both basements are covered by the Middle-Late Neoproterozoic to Phanerozoic sedimentary sequences and intruded by the Paleozoic-Mesozoic granitoids (Li et al., 2014; Wang et al., 2020; Yao et al., 2015). The amalgamation of the SCC was followed by rifting (Xia et al., 2018). The Ediacaran - Early Cambrian SCC rift to drift was characterized by Ediacaran shallow marine carbonate successions overlain by deep marine black shales (Wang and Li, 2003). Within the SCC the black shales are commonly mineralized due to hydrothermal activity related to the abundant basement pre-existing deformation that facilitates fluid flows (Zhang et al., 2021).

### 3.2.1. Study area

The geology of the study area and four sampling section locations, Xiaoyang, Gangchang, Gaojiashan, and Linghekou, are shown in Fig.3.1. Ediacaran and Early Cambrian rocks were sampled. The Ediacaran sequence includes the Doushantou (Early Ediacaran) and Dengying (Late

Ediacaran) formations (Steiner et al., 2007). The Early Cambrian sequence consists of the Guojiaba, Xihaoping, Shuijingtuo, Shipai, and Tianheban formations (Duan et al., 2021) (Fig. 3.2).

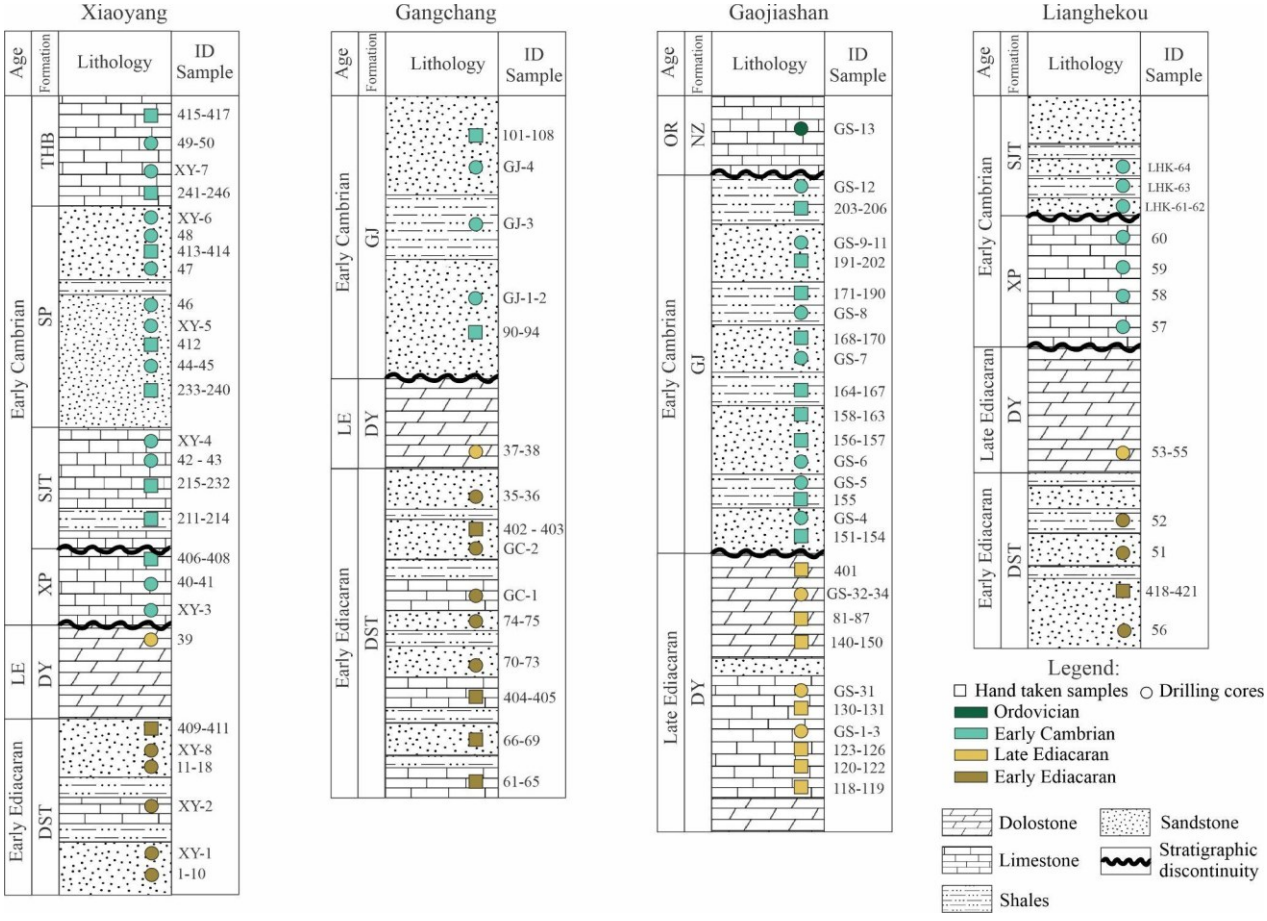


Figure 3.2. Simplified stratigraphic columns of the four study sections. Ediacaran: DST - Doushantou Formation, DY - Dengying Formation; Early Cambrian: GJ - Guojiaba Formation, XP - Xihaoping Formation, SJT - Shuijingtuo Formation, SP - Shipai Formation, THB - Tianheban Formation; Ordovician (OR) - NZ - Nanzheng Formation. LE - Late Ediacaran.

Ediacaran and Early Cambrian were sampled in four stratigraphic sections: Xiaoyang, Gangchang, Gaojiashan, and Linghekou (Fig. 3.1b, c; Fig. 3.2).

The earliest Ediacaran Doushantou Formation consists of carbonates and sandstone with shale interbeds. It is conformably overlain by dolostones of the Dengying Formation. The Doushantou - Dengying boundary is marked by organic-rich black shales. The Doushantou deposition extended

from 635 to 551 Ma; the Dengying Formation was accumulated from 551 to 541 Ma (Och et al., 2016).

In the Gangchang and Gaojiashan sections, the Dengying Formation is disconformably overlain by siliciclastic shales and coarse and fine-grained sandstones of the Lower Cambrian Guojiaba Formation (Steiner et al., 2007). In the Xiaoyang and Lianghekou sections, the Dengying Formation is disconformably overlain by the Early Cambrian strata composed of Xihaoping, Shuijingtuo, Shipai, and Tianheban formations (Steiner et al., 2007). Xihaoping Formation is composed of carbonates (Jiang et al., 2012; Steiner et al., 2007) that are overlain by massive limestone layers interbedded with organic-rich black shale of the Shuijingtuo Formation which is in turn conformably overlain by the Shipai Formation fine-grained sandstones and black shales. The youngest unit, the Tianheban Formation, consists of dark limestones. Deposition of the Early Cambrian strata spanned 542 – 520 Ma within the SCC (Jiang et al., 2012).

### 3.3. Rock-magnetic analysis

The most representative curves of magnetic rock analysis are given in Figure 3.3.

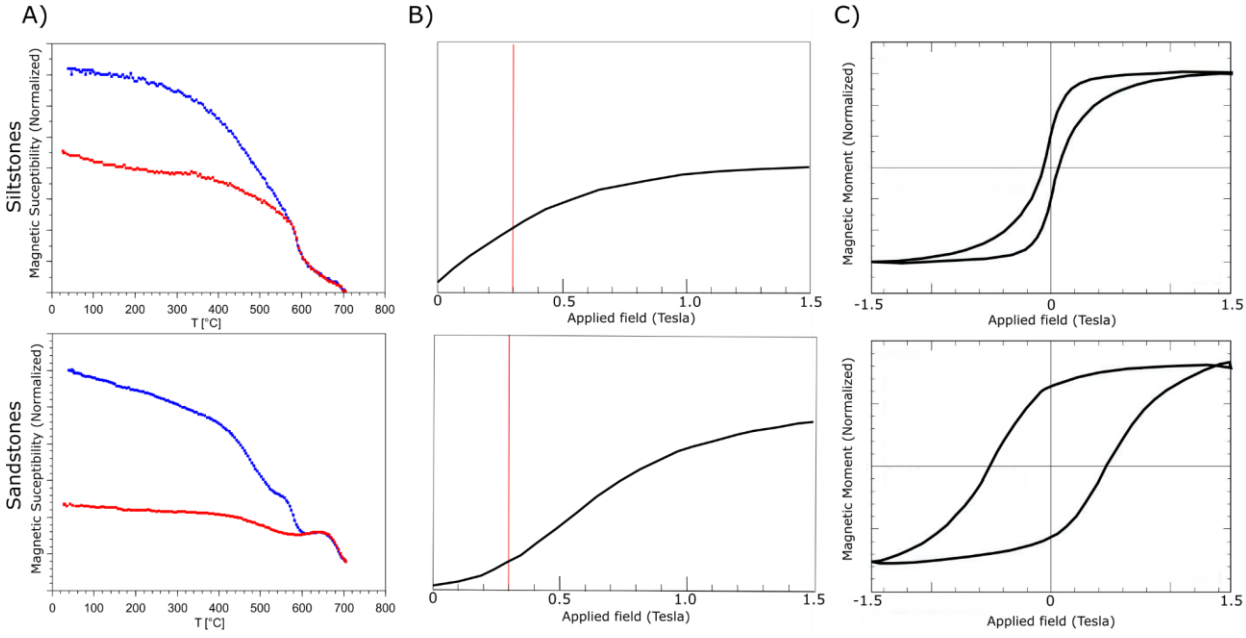


Figure 3.3. Representative (A) thermomagnetic curves, (B) IRM curves, and (C) hysteresis loops from samples of the Dengying and Doushantou Formations. These Rock-magnetic studies and the figure were published in Lysak (2020).

Some thermal demagnetization curves were characterized by a moderate decay up to 570°C that was proceeded by a sharp decrease until 620°C indicating magnetite. The final demagnetization for the majority of samples was achieved at 680°C which corresponds to the unblocking temperature of hematite. This type of the curves revealed a mixture of magnetite and some hematite as carriers of the remnant magnetization. This was supported by the wasp-waist shape of hysteresis loops which also is a signature of a mixture of magnetic minerals with distinct coercivity characteristics (Roberts et al., 1995). The thermomagnetic, IRM, and hysteresis curves are also sensitive to the particle size and type of magnetic domain that we did not study.

The second type of the thermal demagnetization curves is characterized by a moderate decrease up to 600°C succeeded by a distinct hump around 650°C and then a gradual decrease until ~700°C (Fig. 3.3). This also indicates a mixture of magnetite and hematite as carriers of remanence magnetization.

The IRM curves showed that the saturation was either achieved by 1.5 T or was not reached at all (Fig. 3.3b). The absence of full saturation in samples arises from the predominance of hematite as the magnetic carrier (Özdemir and Dunlop, 2014).

### 3.4. Paleomagnetic analysis

#### 3.4.1. Paleomagnetic results for the Ediacaran

The LTC was identified in the temperature range of 100 - 300°C for the Ediacaran samples from all four sections. All mean directions of the LTC at the level of sections are provided in Table 3.1. The identified LTC was characterized by the steep northeast directions with a single normal polarity.

Table 3.1. Summary of results for the low temperature component of the Ediacaran

| Age | Section | Formation | $n/n_0$ | Dg (°) | Ig (°) | kg | $\alpha_{95}$ (°) | Ds (°) | Is (°) | ks | $\alpha_{95}$ (°) |
|---|---|---|---|---|---|---|---|---|---|---|---|
| Early Ediacaran | GC | Doushantou | 94/111 | 5.5 | 57.2 | 19 | 3.4 | 1.3 | 73.5 | 22.1 | 3.2 |
| | LHK | Doushantou | 59/78 | 3 | 55.1 | 17.7 | 4.5 | 32.4 | 6.4 | 17.9 | 4.5 |
| | XY | Doushantou | 23/34 | 15.1 | 50.8 | 21.9 | 6.6 | 36.4 | 12.6 | 21.1 | 6.7 |
| Late Ediacaran | GC | Dengying | 8/11 | 4.7 | 52.6 | 16.9 | 13.9 | 358.7 | 69.8 | 18.8 | 13.1 |
| | GSJ | Dengying | 38/95 | 14.7 | 54.4 | 11.3 | 7.2 | 1.2 | 0.5 | 11.9 | 7 |
| | LHK & XY | Dengying | 10/10 | 15.8 | 48.5 | 17.8 | 11.1 | 35.5 | 24.1 | 14.2 | 12.6 |
| | | Total: | 232/339 | 10 | 53.2 | 288.8 | 3.9 | 22.6 | 31.4 | 5.4 | 31.8 |

*Dg,s and Ig,s - declination and inclination respectively in the geographic and stratigraphic systems, kg and $\alpha_{95}$ - Fisher dispersion parameter and radius of the 95% confidence cone respectively, n - number of samples used in the calculation, $n_0$ - number of the measured samples. GC - Gangchang, GJS - Gaojiashan, LHK - Lianghekou, XY - Xiaoyang sections.

Fig. 3.4 shows that the mean LTC directions for the sections are significantly clustered in the geographic system compared to the stratigraphic system.

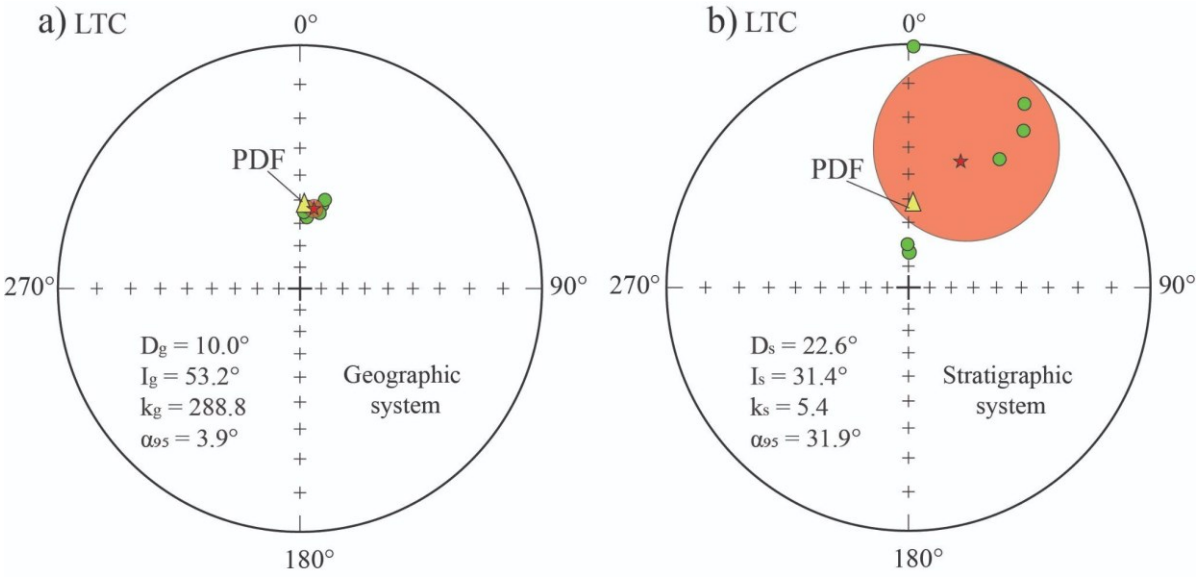


Figure 3.4. Stereographic projections for the LTC of the Ediacaran sections in geographic (a) and stratigraphic (b) coordinates; red star - mean LTC for all sections, yellow triangle - present-day geomagnetic field (PDF), green circles - mean LTC for individual sections.

An overall mean LTC direction from all sections is Dg = 10.0°, Ig = 53.2° ($\alpha_{95}$ = 3.9°, kg = 288.8, n = 232 samples) and Ds = 22.6°, Is = 31.4° ($\alpha_{95}$ = 31.8°, ks = 5.4) in geographic and stratigraphic coordinates correspondingly. The overall LTC mean in geographic coordinates is close to the present-day field (PDF) for the sampling area ($D_{PDF}$ = 3.0°, $I_{PDF}$ = 51°) which indicates the post-folding origin of the component (Fig. 3.4).

McElhinny's (1964) fold test for the mean directions of the LTC is negative since a ratio of dispersion parameters in geographic and stratigraphic coordinates kg/ks = 65.1 exceeds the critical value of 2.97 at the 95% confidence limit and 4.85 at the 99% confidence limit. McFadden's (1990) fold test is also negative: $\xi_1$ = 0.15 for geographic coordinates is less than the critical values of 0.28 at the 95% confidence limit and 0.39 at the 99% confidence limit. In stratigraphic coordinates of coordinates, $\xi_1$ = 0.59 exceeds the critical values ($\xi_{95}$ = 0.28, $\xi_{99}$ = 0.39) significantly at both confidence limits. This supports the post-folding origin of the LTC for all Ediacaran samples.

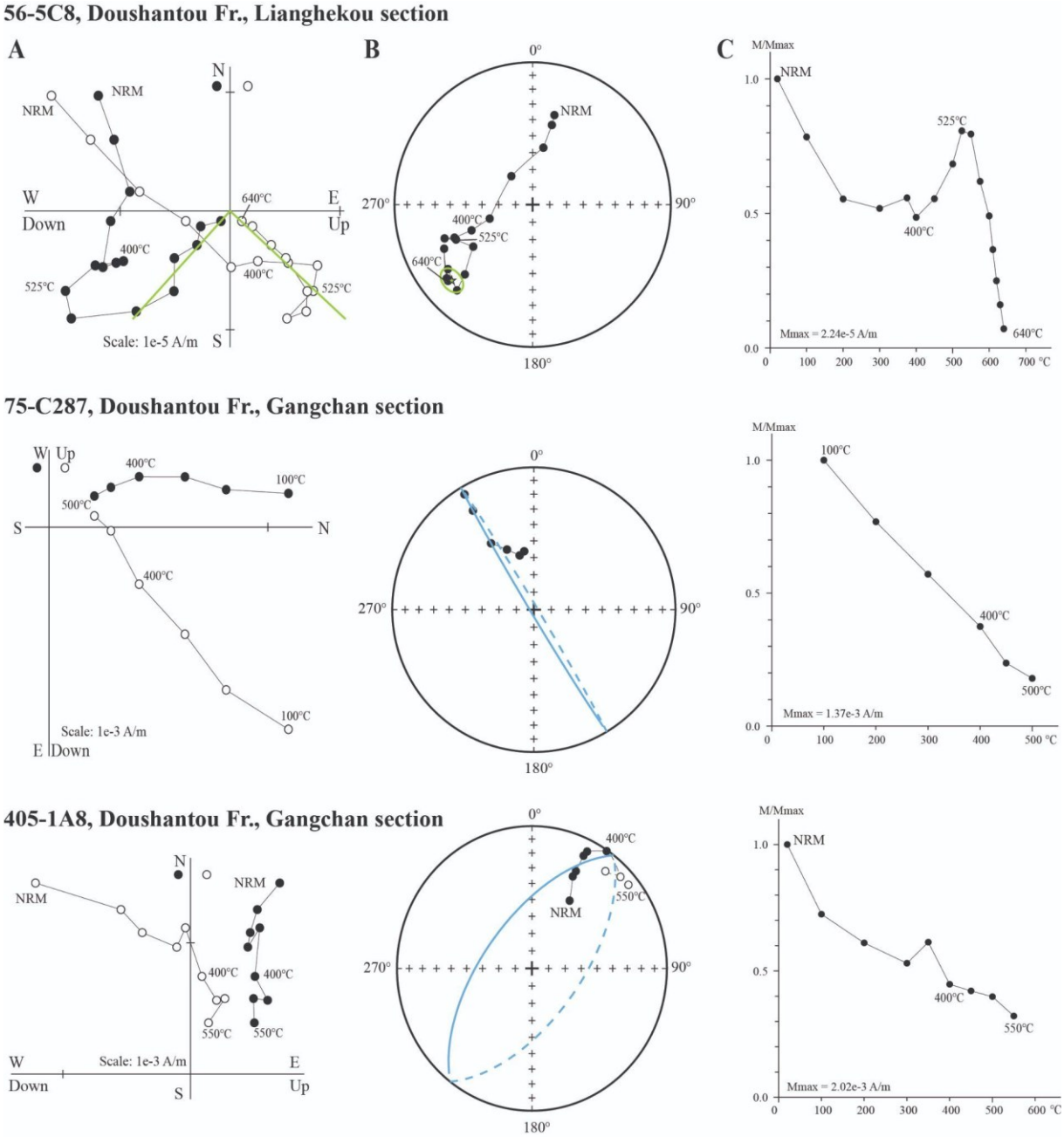


Figure 3.5. Representative (A) Zijderveld diagram, (B) equal-area projection of the directions, and (C) step-wise demagnetization plot for samples of the Doushantou Formation. The green line, star - a direction obtained from the high temperature component (HTC) with normal polarity; blue circles - great circle fitting for directions with reverse polarity.

Samples of the Early Ediacaran Doushantou Formation yielded two distinct clusters of the directions in the southeast (A1SE) and southwest (A2SW) quarters of the stereographic projections (Fig. 3.6). For both clusters, the HTC was identified in the temperature range between 500 - 570°C

and 600 - 690°C which corresponds to the unblocking temperature of magnetite and hematite respectively. The presence of magnetite and hematite as the dominant carriers of the NRM was confirmed by our rock-magnetic studies (Chapter 3.3). The great circle analysis was applied for the samples with a weak NRM in the temperature range between 200 - 550°C.

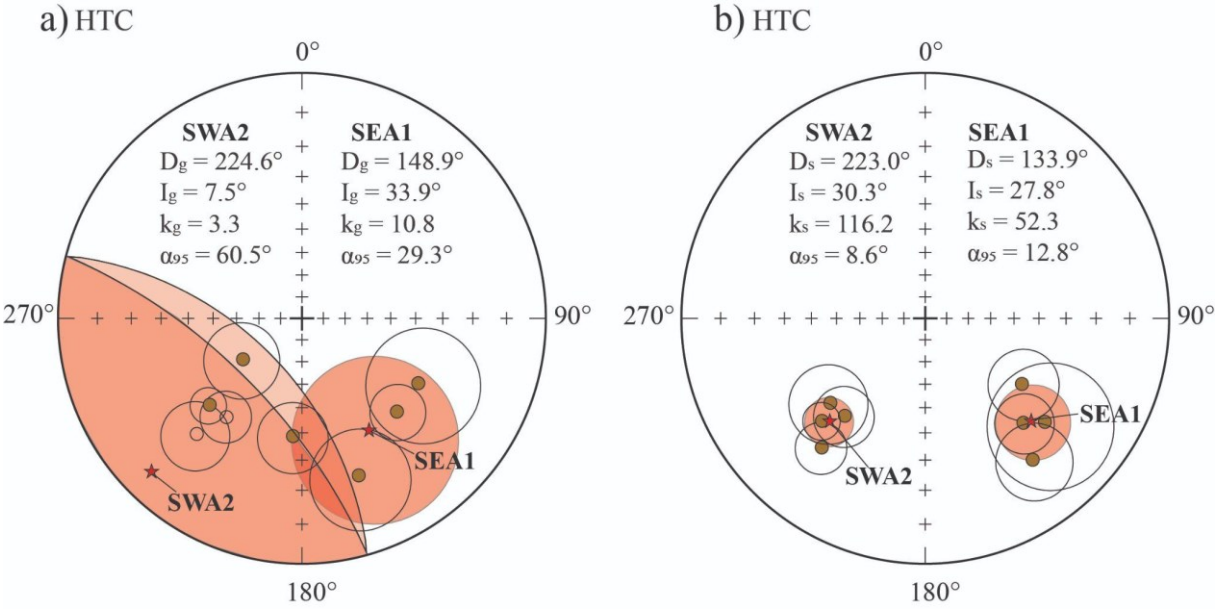


Figure 3.6. Stereographic projections for the HTC of the Doushantou Formation in the geographic (a) and stratigraphic (b) coordinates; red star - mean HTC, the brown circles - mean HTC derived from the site means.

The first cluster A1SE yielded a site mean direction at Dg = 148.9°, Ig = 33.9° ($\alpha_{95}$ = 29.3°, kg = 10.8, n = 31 samples) for four groups of sites with similar bedding orientations in geographic coordinates, and at Ds = 133.9°, Is = 27.8° ($\alpha_{95}$ = 12.8°, ks = 52.3) in stratigraphic coordinates (Fig. 3.6, Table 3.2). The second cluster A2SW was characterized by the mean direction at Dg = 224.6°, Ig = 7.5° ($\alpha_{95}$ = 60.5°, kg = 3.3, n = 4 sites) in geographic coordinates, and at Ds = 223.0°, Is = 30.3° ($\alpha_{95}$ = 8.6°, ks = 116.2) in stratigraphic coordinates (Fig. 3. 6, Table 3.2).

Table. 3.2. Summary of the high temperature component (HTC) results for the Doushantou Formation (Early Ediacaran).

| Component | Section | Samples | Strike (°) | Dip (°) | $n/n_0$ | HTC/ circles | N/R | Dg (°) | Ig (°) | Ds (°) | Is (°) | ks | $\alpha_{95}$ (°) |
|---|---|---|---|---|---|---|---|---|---|---|---|---|---|
| A2SW | LHK | 51, 418-420 | 329.3 | 63.2 | 12/78 | 4/8 | 4/8 | 217.8 | -36.4 | 218.9 | 21.9 | 30.5 | 8.3 |
| A2SW | LHK | 56 | 342.4 | 48.4 | 6/78 | 3/3 | 2/4 | 222.3 | -24.7 | 219.7 | 35.4 | 40.2 | 11.5 |
| A1SE | LHK | 56 | 342.4 | 48.4 | 6/78 | 3/3 | 5/1 | 184.4 | 38.6 | 124 | 38.9 | 29.1 | 13.5 |
| A2SW | GC | 35,36, 402,403 | 120.3 | 19.3 | 6/111 | 2/4 | 3/3 | 234.9 | 57.1 | 228.5 | 35.1 | 27.5 | 14.5 |
| A2SW | GC | 61-74, 404,405 | 82.2 | 19.9 | 14/ 111 | 1/13 | 1/1 3 | 227.1 | 34.9 | 225.4 | 28.5 | 46.7 | 6.5 |
| A1SE | GC | 61-74, 404,405 | 82.2 | 19.9 | 12/11 1 | 2/10 | 2/1 0 | 134.3 | 32.9 | 136.6 | 29.3 | 20.4 | 10.4 |
| A1SE | GC | 35,36, 402,403 | 120.3 | 19.3 | 5/111 | 1/4 | 4/1 | 119 | 32.8 | 130.7 | 24.2 | 22.3 | 20.5 |
| A1SE | XY | XY2,10, 411, XY8, 409 | 333.6 | 46.5 | 8/34 | 1/7 | 5/3 | 160 | 21.5 | 142.6 | 18.1 | 28.6 | 11.8 |
| Total of SEA1 component: | | | | | | | | 148.9 | 33.9 | 133.9 | 27.8 | 52.3 | 12.8 |
| Total of SWA2 component: | | | | | | | | 224.6 | 7.5 | 223 | 30.3 | 116.2 | 8.6 |

*Dg, s and Ig, s - declination and inclination respectively in the geographic and stratigraphic systems of coordinates, kg and $\alpha_{95}$ - Fisher dispersion parameter and radius of the 95% confidence cone respectively, $n_0$ - number of the measured samples, n - number of samples used in the calculation. GC - Gangchang, LHK - Lianghekou, XY - Xiaoyang sections.

The HTC obtained from the A1SE cluster yielded a positive fold test of McElhinny (1964) at the 95% confidence limit and an inconclusive fold test at the 99% confidence limit. A dispersion ratio $k_1/k_2$ = 4.6 exceeded the critical value of 4.3 at the 95% confidence limit but it was below the critical value of 8.5 at the 99% confidence limit (4 sites). McFadden's (1990) fold test for the A1SE directions was inconclusive. The $\xi_1$ = 2.0 in geographic coordinates was around the critical values $\xi_{95}$ = 2.3 and below $\xi_{99}$= 3.1. In stratigraphic coordinates, $\xi_1$ = 0.8 was significantly below both the critical values. In cases when the first definition $\xi_1$ of the McFadden's (1990) fold test appears inconclusive, it is worth considering the second definition $\xi_2$. The first definition $\xi_1$ works better when the angle between the overall mean directions in geographic and stratigraphic coordinates is less than an angle between positions of an individual mean site in corresponding coordinates. In the case of the A1SE cluster, there is a small change in directions (~15° in declination and ~6° in inclination) for the overall mean site as well as for the mean sites.

In geographic coordinates, $\xi_2$ = 3.6 exceeded both the critical values $\xi_{95}$ = 0.2 and $\xi_{99}$= 0.3, and in stratigraphic coordinates, $\xi_2$ = 0.9 was significantly below the corresponding critical values that indicated a positive fold test of McFadden (1990) for the second definition $\xi_2$. The inconclusive fold test of McElhinny (1964) at the 99% confidence limit and the inconclusive fold test of McFadden (1990) for the first definition $\xi_1$ may indicate that the A1SE cluster directions were acquired during or after the folding processes, however, at this stage of the project, we do not have a sufficient number of measured samples to provide statistically significant site-mean directions. This work is planned to be completed during the summer.

For the mean directions calculated from the A2SW cluster, the fold test of McElhinny (1964) was positive and yielded a dispersion ratio of $k_1/k_2$ = 21.2 which exceeded both the critical values of

4.3 and 8.7 at the 95% and 99% confidence limits respectively (4 sites). The McFadden's (1990) fold test was positive since the $\xi_1 = 0.4$ in geographic coordinates exceeded the critical values $\xi_{95} = 0.23$ and $\xi_{99} = 0.32$, in stratigraphic coordinates $\xi_1 = 0.2$ was below the corresponding critical values. These results indicate that the derived HTC from the A2SW cluster was acquired before folding and could be regarded as a primary HTC. The timing of this component is discussed in Chapter 3.5.

The directions from the Early Ediacaran Doushantou Formation samples revealed both the reverse and normal polarities. However, to provide a reversal statistical test of McFadden and McElhinny's (1990) it is necessary to measure more samples, which is a goal of the summer work for this project.

The HTC identified from the samples of the Dengying Formation (Late Ediacaran) yielded directions with a normal polarity in the southwest quarter of the stereographic projection and reverse polarity in the northeast quarter (Fig. 3.7).

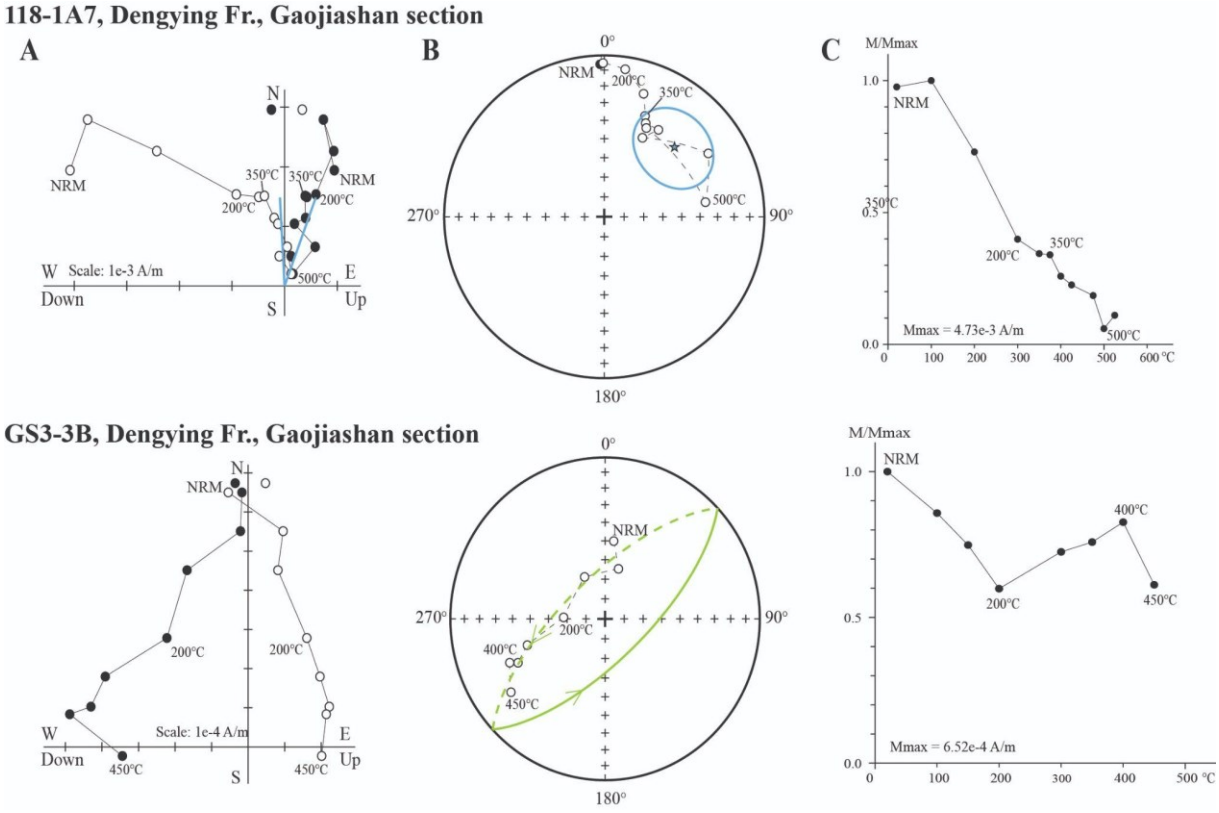


Figure 3.7. Representative (A) Zijderveld diagram, (B) equal-area projection of the directions, and (C) step-wise demagnetization plot for samples of the Dengying Formation. The blue line, star - a direction obtained from the high temperature component (HTC) with reverse polarity; green circles - great circle fitting for directions with normal polarity.

The mean direction (SWA2) from three site means was at Dg = 209.7°, Ig = 4.0° ($\alpha_{95}$ = 66.4°, kg = 4.5, n = 31 samples) in geographic coordinates and at Ds = 211.1°, Is = 29.4° ($\alpha_{95}$ = 10.8°, ks = 131.1) in stratigraphic coordinates (Fig. 3.8, Table 3.3).

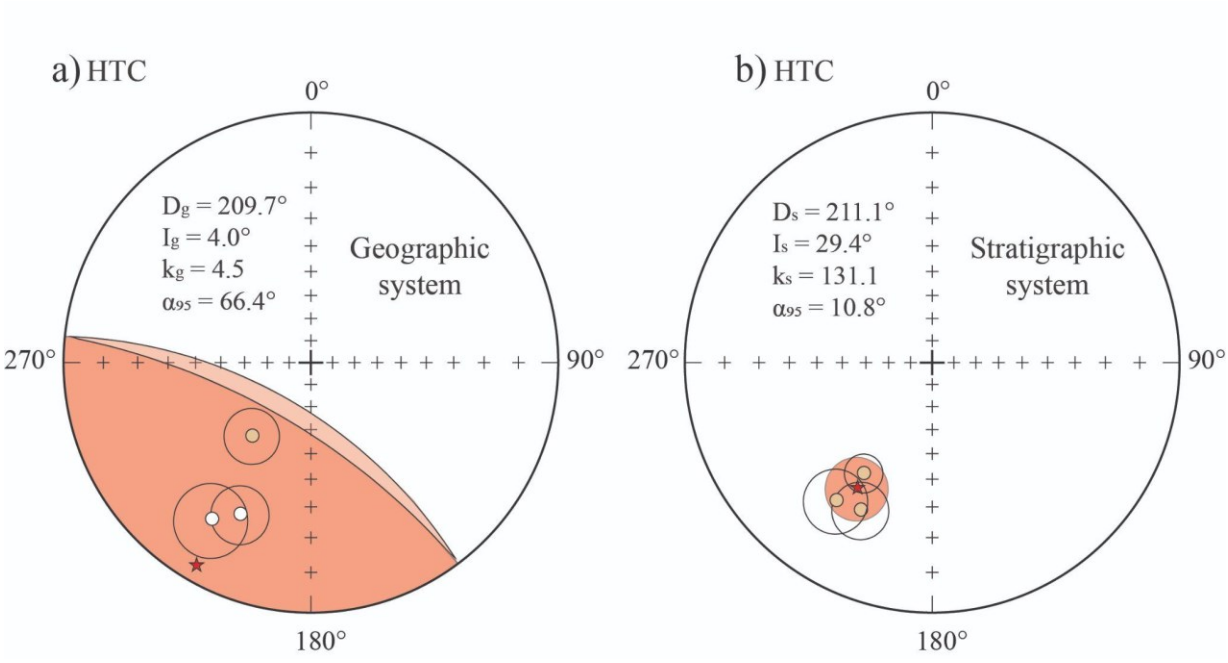


Figure 3.8. Stereographic projections for the HTC of the Dengying Formation in geographic (a) and stratigraphic (b) coordinates; red star - mean HTC, brown circles - mean HTC derived from the section means.

Table. 3.3. Summary of results for the high temperature component (HTC) of the Dengying Formation (Late Ediacaran)

| Component | Section | Samples | Strike (°) | Dip (°) | n/n$_0$ | HTC/ circles | N/R | Dg (°) | Ig (°) | Ds (°) | Is (°) | ks | $\alpha_{95}$ (°) |
|---|---|---|---|---|---|---|---|---|---|---|---|---|---|
| A2SW | GC | 38 | 107.3 | 19.4 | 5/11 | 1/4 | 2/3 | 219 | 48.8 | 212 | 35 | 184.8 | 7 |
| A2SW | GJS | 118, 119, 120 | 257.3 | 57 | 7/95 | 4/3 | 1/6 | 205.2 | -22.5 | 206.1 | 23.6 | 48.4 | 9.2 |
| A2SW | GJS | 131, 149, GS1-3 | 264.2 | 64.8 | 15/95 | 2/13 | 11/4 | 212.6 | -16.9 | 215.1 | 22.2 | 14.6 | 10.7 |

| Component | Section | Samples | Strike (°) | Dip (°) | $n/n_0$ | HTC/ circles | N/R | Dg (°) | Ig (°) | Ds (°) | Is (°) | ks | $\alpha_{95}$ (°) |
|---|---|---|---|---|---|---|---|---|---|---|---|---|---|
| - | LHK | 53-55 | 353 | 29 | 0/8 | 0 | 0 | 0 | 0 | 0 | 0 | 0 | 0 |
| - | XY | 39 | 339.3 | 57 | 0/2 | 0 | 0 | 0 | 0 | 0 | 0 | 0 | 0 |
| Total of SWA2 component: | | | | | | | | 209.7 | 4 | 211.1 | 29.4 | 131.1 | 10.8 |

*Dg, s and Ig, s - declination and inclination respectively in the geographic and stratigraphic systems, kg and $\alpha_{95}$ - Fisher dispersion parameter and radius of the 95% confidence circle respectively, $n_0$ - number of the measured samples, n - number of samples used in the calculation. GC - Gangchang, GJS - Gaojiashan, LHK - Lianghekou, XY - Xiaoyang section.

The obtained HTC from the Late Ediacaran Dengying Formation yielded a positive fold test of McElhinny (1964) at the 95% confidence limit and an inconclusive fold test at the 99% confidence limit. A dispersion ratio $k_1/k_2 = 5.0$ exceeded the critical value of 4.3 at the 95% confidence limit but it was below the critical value of 8.5 at the 99% confidence limit. The McFadden (1990) fold test at the first definition $\xi_1$ of the mean site directions of the Dengying Formation appeared inconclusive at both levels of confidence. The $\xi_1 = 2.0$ in geographic coordinates was about the critical value $\xi_{95} = 2.3$ and it was below $\xi_{99} = 3.1$. In stratigraphic coordinates, $\xi_1 = 0.9$ was below both the critical values. At the second definition $\xi_2$, the fold test of McFadden (1990) was positive. In geographic coordinates, the second definition $\xi_2 = 3.7$ exceeded both the critical values $\xi_{95} = 2.0$ and $\xi_{99} = 3.1$, and in stratigraphic coordinates, $\xi_2 = 0.5$ was significantly below the critical value.

A small number of the obtained site means (only four site means at this stage of the project development) undoubtedly impacted the results of fold tests. The overall means from the HTC of the Dengying Formation and A1SE of the Doushantou Formation are visually more clustered in

stratigraphic coordinates compared to the geographic. After we complete more laboratory demagnetization experiments in the summer, we plan to produce more statistically significant fold test results.

### 3.4.2. Paleomagnetic results for the Early Cambrian

The Early Cambrian samples yielded the LTC in the temperature range of 100 - 300°C. The mean section directions of the LTC from four sections are listed in Table 3.4. The Early Cambrian LTC directions were characterized by the steep inclination with normal polarity and concentrated in the north - northeast quarters of stereographic projection.

The overall mean direction of the LTC from all four sections was obtained at Dg = 11.5°, Ig = 56.2° ($\alpha_{95}$ = 5.9°, kg = 239.9, n = 31 samples) in geographic coordinates and at Ds = 23.5°, Is = 17.6° ($\alpha_{95}$ = 39.3°, ks = 6.4) in stratigraphic coordinates (Fig. 3.9, Table 3.4).

Table 3.4. Summary of results for the LTC of the Early Cambrian.

| Age | Section | Formation | n/$n_0$ | Dg (°) | Ig (°) | kg | $\alpha_{95}$ (°) | Ds (°) | Is (°) | ks | $\alpha_{95}$ (°) |
|---|---|---|---|---|---|---|---|---|---|---|---|
| Early Cambrian | GC | Guojiaba | 13/17 | 14.6 | 57.9 | 18.5 | 9.9 | 13.5 | 48.1 | 19.1 | 9.7 |
| | GSJ | Guojiaba | 42/62 | 0.5 | 53.4 | 13.7 | 6.2 | 358.3 | -14.5 | 10.3 | 7.2 |
| | XY | XP, STJ, SP, THB | 96137 | 15.3 | 53.6 | 29.9 | 2.7 | 36.7 | 12.5 | 28.9 | 2.7 |
| | LHK | XP, STJ | 20/20 | 16.6 | 59.3 | 43.9 | 5 | 42.4 | 20.9 | 45.1 | 4.9 |
| | | Total: | 171236/ | 11.5 | 56.2 | 239.9 | 5.9 | 23.5 | 17.6 | 6.4 | 39.3 |

*Dg, s and $I_{g,\ s}$ - declination and inclination respectively in the geographic and stratigraphic systems, kg and $\alpha_{95}$ - Fisher dispersion parameter and radius of the 95% confidence cone respectively, n - number of samples used in the calculation, $n_0$ -. number of the measured samples, GC - Gangchang, GJS - Gaojiashan, LHK - Lianghekou, XY - Xiaoyang sections.

The PDF ($D_{PDF}$ = 3.0°, $I_{PDF}$ = 51°) lies close to the vicinity of the overall LTC mean in geographic coordinates. The mean section directions are more scattered. This indicates the post-folding origin of the LTC is most likely an overprint by the PDF (Fig. 3.9).

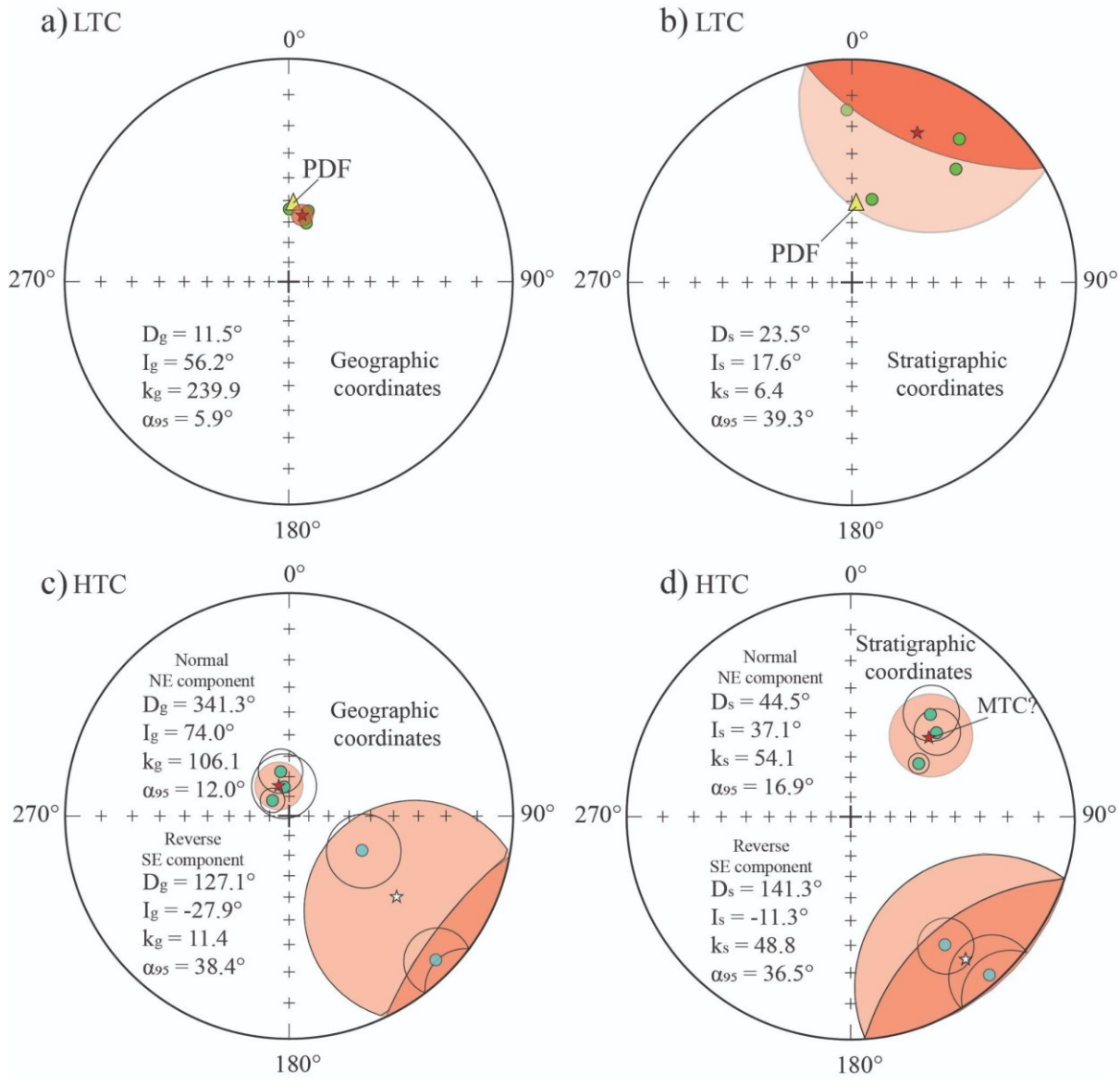


Figure 3.9. Stereographic projections for the LTC of the Early Cambrian in geographic (a) and stratigraphic (b) coordinates; red star - mean LTC, yellow triangle - present day geomagnetic field (PDF), green circles - mean LTC from the sections. Stereographic projections for the HTC of the Early Cambrian in the geographic (c) and stratigraphic (d) coordinates; open star - mean HTC with reverse polarity.

The Early Cambrian HTC directions yielded two distinct clusters in the northeast quarter of the stereographic projection (normal polarity) and southeast quarter of the stereographic projection (reverse polarity) (Fig. 3.9). The HTC of the first cluster was defined in the temperature range of 400 - 550°C and characterized by the northeast directions with normal polarity (Fig. 3.10).

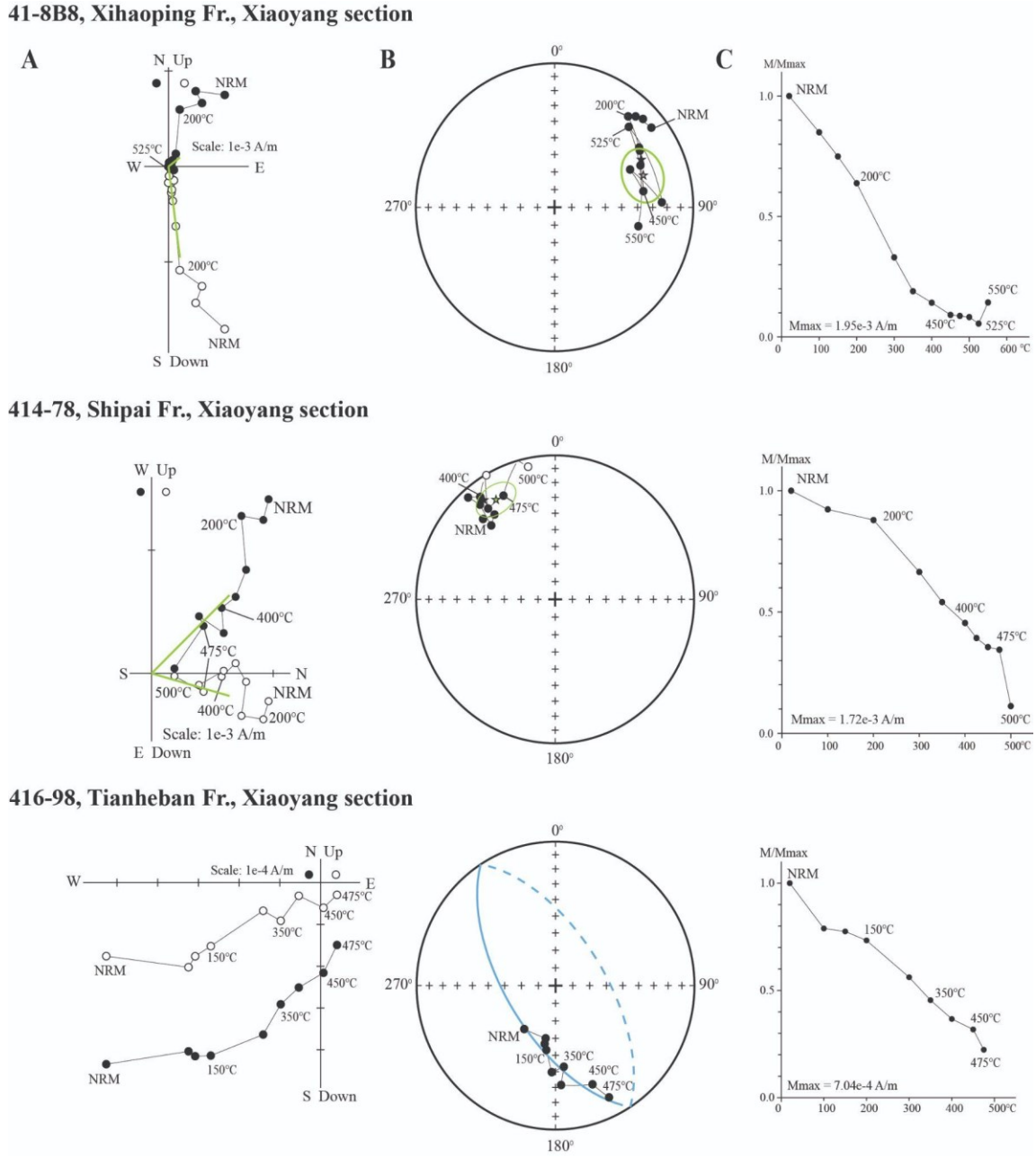


Figure 3.10. Representative (A) Zijderveld diagram, (B) equal-area projection of the directions, and (C) step-wise demagnetization plot for the Early Cambrian samples. The green line, star - a direction obtained from the high temperature component (HTC) with normal polarity; blue circles - great circle fitting for directions with reverse polarity.

The site mean direction obtained from this cluster was at Dg = 341.3°, Ig = 74.0° ($\alpha_{95}$ = 12.0°, kg = 106.1, n = 22 samples) and at Ds = 44.5°, Is = 37.1° ($\alpha_{95}$ = 16.9°, ks = 54.1) in geographic and stratigraphic coordinates respectively (Fig. 3.9, Table 3.5).

Table. 3.5. Summary of results for the high temperature component (HTC) for the Early Cambrian.

| Formation | Component | Section | Samples | Strike (°) | Dip (°) | n/n$_0$ | HTC/circles | N/R | $D_g$ (°) | $I_g$ (°) | $D_s$ (°) | $I_s$ (°) | $k_s$ | $\alpha_{95}$ (°) |
|---|---|---|---|---|---|---|---|---|---|---|---|---|---|---|
| XP | reverse SE | GJS | 152,194, GS11, 5, 6, 9 | 262.1 | 72.1 | 10/79 | 1/9 | 1/9 | 115.4 | -50.4 | 138.9 | -3.4 | 21.2 | 11.6 |
| XP, STJ | normal NE | LHK | 57-60 | 341.1 | 46.6 | 5/20 | 2/3 | 5/0 | 313 | 78.4 | 51.9 | 47.8 | 277.5 | 4.6 |
| SP, THB | normal NE | XY | 242, XY6,7, 44 | 339.7 | 49.3 | 5/77 | 4/1 | 5/0 | 350.4 | 74.9 | 45.5 | 33.5 | 75.1 | 9.2 |
| XP, STJ | normal NE | XY | 40,41,42 XY3,4 | 335.4 | 53 | 12/55 | 5/7 | 12/0 | 349.2 | 67.1 | 37.8 | 29.7 | 18.4 | 10.7 |
| SP, THB | reverse SE | XY | 414-417, 46-48, 235 - 236 | 339.7 | 49.3 | 17/77 | 3/14 | 2/15 | 134.6 | -4.8 | 143.8 | -19.1 | 15.5 | 9.5 |
| Total of SE reverse component: | | | | | | | | | 127.1 | -28 | 141.3 | -11.3 | 48.8 | 36.5 |
| Total of NE normal component: | | | | | | | | | 341.3 | 74 | 44.5 | 37.1 | 54.1 | 16.9 |

*Dg, s and Ig, s - declination and inclination respectively in the geographic and stratigraphic coordinates, kg/ks - Fisher dispersion parameter in geographic/stratigraphic coordinates, $\alpha_{95}$ - radius of the 95% confidence circle, n$_0$ - number of the measured samples, n - number of samples used in the calculation. GJS - Gaojiashan, LHK - Lianghekou, XY - Xiaoyang sections.

McElhinny's (1964) fold test was inconclusive for the northeast cluster since a dispersion ratio of $k_1/k_2$ = 2.2 was below the critical $k_{95}$ = 6.4 and $k_{99}$ = 16.0. McFadden's (1990) fold test was inconclusive both at the 95% and 99% confidence levels as well. The first definition $\xi_1$ = 0.69 in

the geographic and $\xi_1$ = 0.67 in stratigraphic coordinates was below the critical values $\xi_{95}$ = 2.1 and $\xi_{99}$= 2.7. Both fold tests indicated that the HTC derived from the northeast cluster was likely acquired during post-folding processes and probably corresponds to the youngest age magnetization. In addition, the defined mean directions were located close to the PDF and yielded only single normal polarity. This also supports an assumption that the recorded HTC is post- or synfolding or could be interpreted as the middle temperature component (MTC).

The second cluster included only two mean sites characterized by shallow southeast inclinations with reverse polarity. The HTC was dominated by reverse polarity and was identified in the temperature range between 400 - 560°C correlated with the temperature range observed in the northeast cluster. For samples that revealed a weak NRM with unstable behavior of step-wise demagnetization after 500°C, the great circle fitting was applied in the temperature range of 200 - 500°C (Fig. 3.10).

Since only two site means were defined for the southeast cluster, the fold tests of McElhinny (1964) and McFadden (1990) were not applied. To improve statistics additional measurements of the step-wise demagnetization will be conducted in the next stage of this project. Nevertheless, the overall mean was calculated for the reverse southeast cluster that was at Dg = 127.1°, Ig = -28.0° ($\alpha_{95}$ = 146.7°, kg = 5.7, n = 27 samples) and at Ds = 141.3°, Is = -11.3° ($\alpha_{95}$ = 36.5°, ks = 48.8) in geographic and stratigraphic coordinates respectively (Fig. 3.9, Table 3.5).

### 3.5. Discussion of the Ediacaran and Early Cambrian paleomagnetic poles

In this study two distinct site-mean HTCs (SEA1 and SWA2) were derived from the Early Ediacaran Doushantou Formation which yielded the paleomagnetic poles at 25.7°S/157.6°E ($A_{95}$

= 10.3°, dp/dm = 14.0°/7.6°, N = 4 sites) and 26.5°S/60.0°E ($A_{95}$ = 7.1°, dp/dm = 9.6°/5.3°, N = 4 sites) respectively (Table 3.6).

Table 3.6. Paleomagnetic results for Ediacaran and Early Cambrian in the SCC

| **Component** | **Pole latitude (°)** | **Pole longitude (E°)** | **$A_{95}$ (°)** | **dp** | **dm** | **N/n** | **Paleolat (N°)** |
|---|---|---|---|---|---|---|---|
| Early Ediacaran, Doushantou Formation | | | | | | | |
| SEA1 | 25.7S | 157.6 | 10.3 | 14.0 | 7.6 | 4/31 | 14.8 |
| SWA2 | 26.5S | 60.0 | 7.1 | 9.6 | 5.3 | 4/38 | 16.3 |
| Late Ediacaran, Dengying Formation | | | | | | | |
| SW | 33.7S | 70.3 | 8.9 | 11.9 | 6.6 | 3/27 | 15.7 |
| Early Cambrian, Xihaoping, Shuijingtuo, Shipai, and Tianheban Formations | | | | | | | |
| NE | 48.9N | 201.7 | 15.2 | 19.8 | 11.6 | 3/22 | 20.7 |
| SE | 45.3N | 349.3 | 26.4 | 37.0 | 18.8 | 2/27 | 5.7 |

*$A_{95}$ - radius of 95% confidence cone about the pole; dp/dm - semi-axes of elliptical error around the pole at a probability of 95%; N - number of the section means; n - number of samples; N - Northern Hemisphere; S - Southern Hemisphere. Paleolatitudes are calculated at the reference point of 32°N/107°E.

The attributed paleolatitudes are at 14.8°N ± 7.6° and 16.3°N ± 5.3° for the SEA1 and SWA2 components correspondingly. The poles can be considered preliminary because the number of sites is too small for statistically significant conclusions.

Fig. 3.11 shows that the newly obtained poles are located on the same small circle relative to the study location at 32°N/107°E. This implies that the poles are rotated relative to each other by 84°.

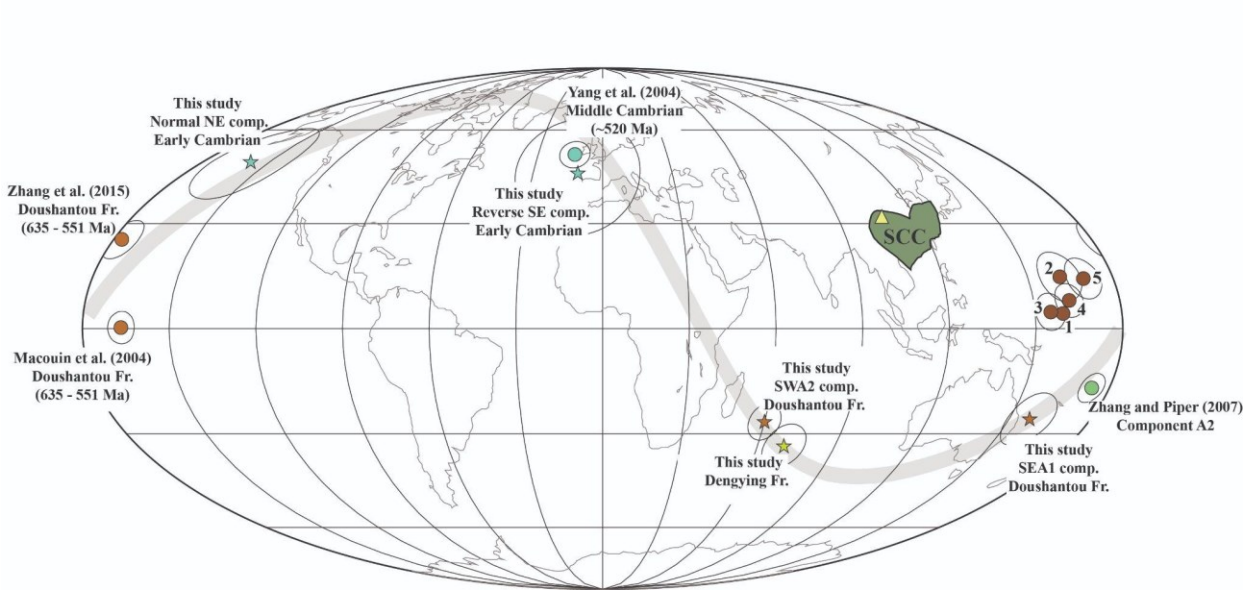


Figure 3.11. Paleomagnetic poles of the Neoproterozoic - Middle Cambrian for the SCC. The grey line represents a small circle.

Both our poles differ from the coeval paleomagnetic poles published in Macouin et al. (2004) and Zhang et al. (2015). A prefolding origin of the paleomagnetic directions in Macouin et al. (2004) has been doubted since only reverse polarity was identified in contrast to the paleomagnetic data obtained in the other works (Zhang et al., 2013; Zhang et al., 2015). The paleomagnetic directions in Zhang et al. (2015) passed the reversal test of McFadden and McElhinny (1990) but the fold tests were not applied because the samples were collected only at one locality with a similar bedding orientation. Thus, there is no solid evidence supporting the primary origin of the HTC in Macouin et al. (2004) or in Zhang et al. (2015).

The pole from Zhang et al. (2015) lies close to the great circle crossing our poles (Fig. 3.11) and may indicate potentially large rotations of the SCC. The depositional age range of the Doushantou Formation spans 84 m.y. (Jiang et al., 2011). Hence, the SCC could have rotated ~57° as suggested by the SEA1 and Zhang et al. (2015) poles, or ~129° as required by the SWA2 and Zhang et al. (2015) poles.

Fig. 3.12 shows that our poles and the pole from Zhang et al. (2015) yielded different paleolatitudes. The difference of ~10° could be explained by the difference in age between the samples collected in our study and those collected by Zhang et al. (2015). If the Zhang et al. (2015) samples were collected from near the bottom of the formation and ours from its near the top, then it is possible that the SCC moved southward within ~84 Ma with a velocity of about 1.3 cm/year.

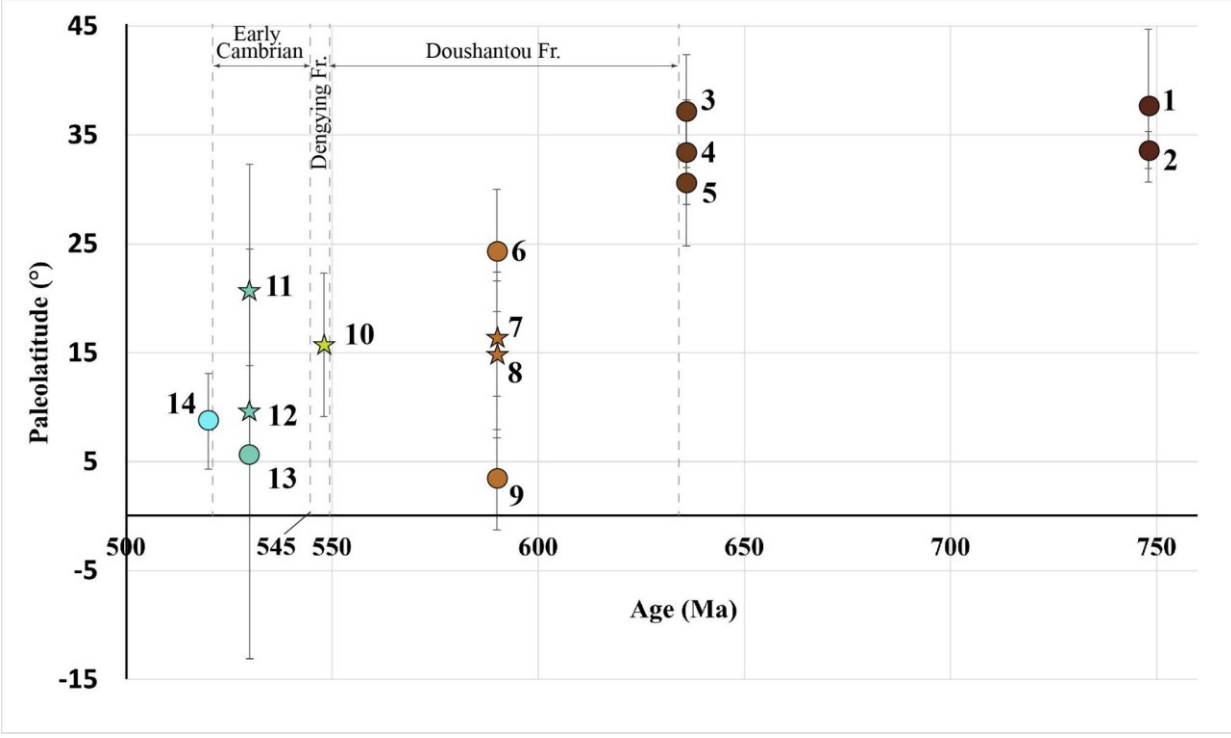


Figure 3.12. Middle Neoproterozoic - Middle Cambrian paleolatitudes for the SCC. 1, 2) Evans et al. (2000); 3) component A1, Zhang and Piper (1997); 4,5) Zhang et al. (2013); 6) Doushantou Fr., Zhang et al. (2015); 7) component SWA2, Doushantou Fr., this study; 8) component SEA1, Doushantou Fr., this study; 9) Doushantou Fr., Macouin et al. (2004); 10) Dengying Fr., this study; 11) normal NE component, Early Cambrian, this study; 12) reverse SE component, Early Cambrian, this study; 13) component A2, Zhang and Piper (1997); 14) Middle Cambrian, Yang et al. (2004). Paleolatitudes 6 - 9 representing the Doushantou Fr. are placed in the center of the Doushantou duration (635-551 Ma) although the exact stratigraphic relationship between them is not defined.

The paleolatitudes obtained by Zhang et al. (2013) and Zhang and Piper (1997) and our paleolatitude from the Doushantou Formation required that the SCC moved southward from ~33°N to ~15°N with a velocity of about 3.5 cm/year for the time interval of ~84 Ma (Fig. 3.12).

We obtained the first paleomagnetic pole from the Late Ediacaran Dengying Formation, 551 - 545 Ma, at 33.7°S/70.3°E ($A_{95}$ = 8.9°, dp/dm = 11.9°/6.6°, N = 3 sites). This preliminary pole resembles the paleomagnetic pole obtained from the SWA2 component of the Doushantou Formation and yielded a similar paleolatitude at 15.7°N ± 6.6° (Fig 3.12). It could mean that the SCC maintained a position around 15°N with a rotation at 11° during the Late Ediacaran. The obtained site mean directions from the Dengying Formations yielded the inconclusive fold test of McFadden's (1990) while the directions of the SWA2 gave a positive fold test. The preliminary character of the Doushantou and Dengying Formations paleomagnetic results does not allow us to provide a final interpretation now.

Similarly to us, Zhang and Piper (1997) obtained two distinct HTC components for the Middle Neoproterozoic samples with the age close to the boundary between the late Middle Neoproterozoic and Doushantou Formation of the Early Ediacaran. The component A2 yielded a paleomagnetic pole at 16.7°S/173.8°E ($A_{95}$ = 5.7°, dp/dm = 7.2°/5.2°, N = 5 sites) that lies close to our component SEA1 of the Doushantou Formation on the same great circle. Zhang and Piper (1997) proposed that this component could be secondary magnetization recorded later in the Ediacaran or Early Cambrian.

Two distinct components (normal NE and reverse SE) were isolated from the Early Cambrian samples as well. The normal polarity NE component yielded a paleomagnetic pole at 48.9°N/201.7°E ($A_{95}$ = 15.2°, dp/dm = 19.8°/11.6°, N = 3 sites). The directions of this component

yielded inconclusive fold tests because of a low number of sites used in statistics. Nevertheless, this pole also lies on the same great circle with the Ediacaran poles (Fig. 3.11).

The second reverse polarity SE component of the Early Cambrian yielded a pole at 45.3°N/349.3°E ($A_{95}$ = 26.4°, dp/dm = 37.0°/18.8°, N = 2 sites). This pole is located close to the Middle Cambrian pole reported in Yang et al. (2004).

Considering all available paleomagnetic data from the Middle Neoproterozoic to the Middle Cambrian it appears that the SCC was moving southward during this interval from the paleolatitudes ~33 - 37°N to subequatorial latitudes ~6 - 9°N (Fig. 3.12). This is consistent with a tectonic model described in Li et al. (2008) which addresses the period from 750 to 530 Ma when the supercontinent Rodinia experienced a break-up. The model proposed that the SCC was a part of the supercontinent but rifted away in part due to a superplume activity between 825 and 630 Ma.

Li et al. (2008) proposed that the SCC subsequently moved northward and reached 30°N in the Cambrian. This interpretation contradicts our preliminary Late Neoproterozoic - Early Cambrian paleomagnetic poles suggesting that, on the contrary, the SCC translated slowly southward to the subequatorial latitudes of ~9°N during 630 - 530 Ma (Fig. 3.12).

All the obtained poles lie on the same great circle, and the angle between them is always around 82 - 84°. The angle between the SWA2 and SEA1 is ~84°, the angle between the normal NE and reverse SE of the Early Cambrian is ~82°, and the angle between the SWA2 of the Doushantou and reverse SE of the Early Cambrian is ~96°. The SEA1 pole and pole from the Cambrian reverse polarity SE component are nearly antipodal.

Mitchell et al. (2010) reported the Early-Middle Cambrian paleomagnetic poles from central Australia that suggested a clockwise rotation of 60°. Meert (2014) reviewed a paleomagnetic dataset for Baltica corresponding to the Ediacaran - Ordovician period. Baltica probably experienced a rotation of 82° during 608 - 550 Ma and 97° during 550 - 500 Ma. These values correlate with a rotation of ~96° between the SWA2 of the Doushantou Formation and the reverse polarity SE component of the Early Cambrian in our study that takes place between 635 and 520 Ma (Ediacaran - Early Cambrian).

Rapid motions of the continents comprising the Rodinia during the Ediacaran - Early Cambrian have been interpreted as a result of plume activity. However, the more paleomagnetic data becomes available the more problematic reconstructions. This has resulted in the suggestion of a non-dipole geomagnetic field or oscillations of True Polar Wander (TPW). Abrajevitch and Van der Voo (2010) suggested that rapid motions of the paleomagnetic poles or, in the other words, rapid motions of the virtual geomagnetic poles (VGP) could be attributed not to continent motions but an oscillation or polarity reversals of the geomagnetic field during the Ediacaran - Early Cambrian. It was also proposed that the non-dipole components of the geomagnetic field could be predominant during a period of polarity reversals. Thus, Abrajevitch and Van der Voo (2010) proposed that in the Ediacaran - Early Cambrian the geomagnetic field could be dominated by the equatorial dipole component that contributed to a misalignment of the acquired NRM relatively to the axis of the dipolar component of the geomagnetic field. Such an idea was supported by a recent re-evaluation of the paleomagnetic data from Australia and Siberia (Shatsillo et al., 2022), where the authors suggested the coexistence of a weak, long-lived source of the geomagnetic field and a strong main dipole source that was unstable and changed its orientation. Pavlov et al. (2018) showed that the apparent scatter of the Siberian poles indicated irregular behavior of the

geomagnetic field in the Ediacaran - Cambrian. This could be attributed to the alternation of the co-axial and quasi-equatorial dipole. Kravchinsky et al. (2001) showed the presence of two high temperature components in the Ediacaran sediments of Siberia interpreting the highest temperature component as the primary because it had two polarities. They demonstrated that the paleomagnetic poles of Siberia were spread generally along the same great circle with the Euler pole at the sampling locality.

To provide better constraints of the motion of the SCC's VGP more paleomagnetic data is required allowing the use of statistical analysis and evaluation of the inclination shallowing. This project will be continued.

## Chapter 4: Conclusions and future work

This thesis provides the first reliable paleomagnetic poles for the Late Carboniferous and Early Permian of the North China Craton (Chapter 2) and preliminary poles for the Ediacaran - Early Cambrian of the South China Craton (Chapter 3).

We completed two statistically representative paleomagnetic studies for the Taiyuan (Late Carboniferous) and Shanxi (Early Permian) Formations. Our zircon data confirmed the Late Carboniferous age of the Taiyuan Formation. We purposely collected rock samples in the middle of the NCC, so the poles can represent the craton to avoid doubts regarding the tectonic coherence with the craton. Our new paleomagnetic poles for the NCC meet all reliability criteria for primary magnetization. The poles improve the Late Paleozoic segment of the NCC APWP and produce the first well-constrained paleogeographic reconstructions for the NCC between 306 Ma and 293 Ma. In our new reconstructions, the NCC is placed further north in the Late Carboniferous and Early Permian than it was assumed before based on the poles with a low reliability index. Our review of all available Late Carboniferous - Early Permian paleomagnetic poles from the adjacent blocks that constitute the Amuria/Inner Mongolia Blocks demonstrates that the Amuria collage of blocks was not a part of the NCC by the Early Permian. Our result showed that the width of Paleo Asian Ocean between the Amuria Block and NCC was ~700 km, which was approximately two times smaller than it was considered before.

We studied two Ediacaran Formations (Doushantou and Dengying) and four Early Cambrian Formations (Xihaoping, ShuiJingtuo, Shipai, and Tianheban) from the northeastern edge of the South China Craton. We obtained the Early Cambrian paleomagnetic data for the SCC for the first

time. Other paleomagnetic poles for the Ediacaran and Cambrian were mostly obtained in the center of the SCC in the Jiangnan Orogen between the Yangtze and Cathaysia Blocks. To test the validity of previous studies and to perform a reliable fold test, we sampled in different sections of the northeastern edge of the SCC. Our paleomagnetic poles for the Ediacaran and Early Cambrian of the South China Craton are preliminary, however, the potential of obtaining statistically plausible results in the future is demonstrated in the thesis results. We were able to successfully isolate low and high temperature components. The high temperature components for the Ediacaran Doushantou Formation and Early Cambrian Formations demonstrated the presence of two high temperature components rotated relative to each other. The Ediacaran and Early Cambrian poles lie on the same great circle with the Euler pole at the sampling locality but rotated relative to each other for almost 90°. Although it is early for us to make firm conclusions based on preliminary data, the rotated poles for the same geological time resemble the situation with the scattering of the Laurentian, Australian and Siberian poles. A number of hypotheses were suggested to explain such a scatter. We plan to measure more samples in the summer months and produce statistically reliable results and final interpretation.

## References

Abrajevitch, A., & Van der Voo, R. (2010). Incompatible Ediacaran paleomagnetic directions suggest an equatorial geomagnetic dipole hypothesis. *Earth and Planetary Science Letters*, *293*(1-2), 164-170.

Baatar, U. (2001). Paleozoic sedimentary basins and volcanic arc systems of southern Mongolia: New geochemical and petrographic constraints. *Paleozoic and Mesozoic tectonic evolution of Central and Eastern Asia*, *194*, 117.

Badarch, G., Cunningham, W. D., & Windley, B. F. (2002). A new terrane subdivision for Mongolia: implications for the Phanerozoic crustal growth of Central Asia. *Journal of Asian Earth Sciences*, *21*(1), 87-110.

Bazhenov, M. L., Kozlovsky, A. M., Yarmolyuk, V. V., Fedorova, N. M., & Meert, J. G. (2016). Late paleozoic paleomagnetism of South Mongolia: exploring relationships between Siberia, Mongolia and North China. Gondwana Research, 40, 124-141.

Butler, R. F. (1992). *Paleomagnetism: magnetic domains to geologic terranes* (Vol. 319). Boston: Blackwell Scientific Publications.

Cawood, P. A., Strachan, R. A., Pisarevsky, S. A., Gladkochub, D. P., & Murphy, J. B. (2016). Linking collisional and accretionary orogens during Rodinia assembly and breakup: Implications for models of supercontinent cycles. *Earth and Planetary Science Letters*, *449*, 118-126.

Cawood, P.A., Zhao, G., Yao, J., Wang, W., Xu, Y., & Wang, Y., 2018. Reconstructing South China in Phanerozoic and Precambrian supercontinents. Earth-Science Reviews, 186, 173-194.

Chai, H., Ma, Y., Santosh, M., Hao, S., Luo, T., Fan, D., ... & Wang, Q. (2020). Late Carboniferous to Early Permian oceanic subduction in central Inner Mongolia and its correlation with the tectonic evolution of the southeastern Central Asian Orogenic Belt. *Gondwana Research*, *84*, 245-259.

Chen, Y. (2004). Geological map of China 1: 4 000 000. Geological Publishing House.

Chen, Y., Zhang, Z., Qian, X., Li, J., Ji, Z., & Wu, T. (2020). Early to mid-Paleozoic magmatic and sedimentary records in the Bainaimiao Arc: An advancing subduction-induced terrane accretion along the northern margin of the North China Craton. *Gondwana Research*, *79*, 263-282.

Cleal, C. J., & Ziqiang, W. (2002). A new and diverse plant fossil assemblage from the upper Westphalian Benxi Formation, Shanxi, China, and its palaeofloristic significance. Geological Magazine, 139(2), 107-130.

Cogné, J. P. (2003). PaleoMac: a Macintosh™ application for treating paleomagnetic data and making plate reconstructions. Geochemistry, Geophysics, Geosystems, 4(1).

Dan, W., Li, X. H., Wang, Q., Wang, X. C., Wyman, D. A., & Liu, Y. (2016). Phanerozoic amalgamation of the Alxa Block and North China Craton: Evidence from Paleozoic granitoids, U–Pb geochronology and Sr–Nd–Pb–Hf–O isotope geochemistry. *Gondwana Research*, *32*, 105-121.

Deenen, M. H., Langereis, C. G., van Hinsbergen, D. J., & Biggin, A. J. (2011). Geomagnetic secular variation and the statistics of palaeomagnetic directions. *Geophysical Journal International*, *186*(2), 509-520.

Domeier, M., & Torsvik, T. H. (2014). Plate tectonics in the late Paleozoic. *Geoscience Frontiers*, *5*(3), 303-350.

Dong, Y., & Santosh, M. (2016). Tectonic architecture and multiple orogeny of the Qinling Orogenic Belt, Central China. *Gondwana Research*, *29*(1), 1-40.

Duan, X., Betts, M. J., Holmer, L. E., Chen, Y., Liu, F., Liang, Y., & Zhang, Z. (2021). Early Cambrian (Stage 4) brachiopods from the Shipai Formation in the Three Gorges area of South China. *Journal of Paleontology*, *95*(3), 497-526.

Embleton, B. J., McElhinny, M. W., Ma, X., Zhang, Z., & Xiang Li, Z. (1996). Permo-Triassic magnetostratigraphy in China: the type section near Taiyuan, Shanxi province, North China. *Geophysical Journal International*, *126*(2), 382-388.

Enkin, R. J. (2004). Paleomagnetism Data Analysis: Version 4.2. Geological Survey of Canada.

Evans, D. A. (1998). *I. Neoproterozoic-paleozoic supercontinental tectonics and true polar wander. II. Temporal and spatial distributions of proterozoic glaciations* (Doctoral dissertation, California Institute of Technology).

Evans, D. A. (2009). The palaeomagnetically viable, long-lived and all-inclusive Rodinia supercontinent reconstruction. *Geological Society, London, Special Publications*, *327*(1), 371-404.

Evans, D. A., Li, Z. X., Kirschvink, J. L., & Wingate, M. T. (2000). A high-quality mid-Neoproterozoic paleomagnetic pole from South China, with implications for ice ages and the breakup configuration of Rodinia. *Precambrian Research*, *100*(1-3), 313-334.

Fang, D. J., Guo, Y., Wang, Z. L., Tan, X. D., Fan, S. Q., Yuan, Y. R., ... & Wang, B. (1988). Tectonic implications of Triassic and Jurassic paleomagnetic results from Ningwu basin, Shanxi Province. *Kexue Tongbao*, *2*, 133-135.

Fang, D. J., Yang, S. F., Guo, Y. B., Jin, G. H., Chen, H. L., Tian, X. D., & Wu, N. Y. (1992). Preliminary discussion on the tectonic evolution and the relationships among three major plates of China from paleomagnetic data of late Paleozoic to Mesozoic. In *Symposium of Researches on Modern Geology* (Vol. 1, pp. 199-210). Nanjing University Press.

Feng, L., Huaicheng, Z., & Shu, O. (2008). Late Carboniferous–Early Permian palynology of Baode (Pao-te-chou) in Shanxi Province, North China. *Geological Journal*, *43*(4), 487-510.

Feng, Z. Q., Li, W. M., Liu, Y. J., Jin, W., Wen, Q. B., Liu, B. Q., ... & Li, X. Y. (2018). Early Carboniferous tectonic evolution of the northern Heihe–Nenjiang–Hegenshan suture zone, NE China: Constraints from the mylonitized Nenjiang rhyolites and the Moguqi gabbros. Geological Journal, 53(3), 1005-1021.

Fisher, R. A. (1953). Dispersion on a sphere. *Proceedings of the Royal Society of London. Series A. Mathematical and Physical Sciences*, *217*(1130), 295-305.

Fu, L., Li, Z., Xu, J., Li, J., Wang, P., Ji, Q., & Ding, Z. (2010). Impermeability Analysis of Middle Ordovician Fengfeng Formation in Wangjialing Coalmine [J]. *Coal Geology of China*, *3*.

Fu, W., Hou, H., Gao, R., Zhou, J., Zhang, X., Pan, Z., ... & Guo, R. (2021). Lithospheric Structures of the Northern Hegenshan-Heihe Suture: Implications for the Paleozoic Metallogenic Setting at the Eastern Segment of the Central Asian Orogenic Belt. *Ore Geology Reviews*, 104305.

Gilder, S., & Courtillot, V. (1997). Timing of the North-South China collision from new middle to late Mesozoic paleomagnetic data from the North China Block. *Journal of Geophysical Research: Solid Earth*, *102*(B8), 17713-17727.

Gong, Z., Kodama, K. P., & Li, Y. X. (2017). Rock magnetic cyclostratigraphy of the Doushantuo Formation, South China and its implications for the duration of the Shuram carbon isotope excursion. *Precambrian Research*, *289*, 62-74.

Gou, J., Sun, D., Mao, A., Yang, D., & Tang, Z. (2019). Geochronology and geochemistry of Ordovician plutons in the Erguna Block (NE China): further insights into the tectonic evolution of the Xing'an–Mongolia Orogenic Belt. *International Geology Review*, *61*(8), 936-955.

Gradstein, F. M., & Ogg, J. G. (2020). The chronostratigraphic scale. In *Geologic time scale 2020* (pp. 21-32). Elsevier.

Guy, A., Schulmann, K., Clauer, N., Hasalova, P., Seltmann, R., Armstrong, R., ... & Benedicto, A. (2014). Late Paleozoic–Mesozoic tectonic evolution of the Trans-Altai and South Gobi Zones in southern Mongolia based on structural and geochronological data. *Gondwana Research*, *25*(1), 309-337.

Han, G., Liu, Y., Neubauer, F., Jin, W., Genser, J., Ren, S., ... & Liang, C. (2012). LA-ICP-MS U–Pb dating and Hf isotopic compositions of detrital zircons from the Permian sandstones in Da Xing'an Mountains, NE China: New evidence for the eastern extension of the Erenhot–Hegenshan suture zone. *Journal of Asian Earth Sciences*, *49*, 249-271.

Han, G., Liu, Y., Neubauer, F., Bartel, E., Genser, J., Feng, Z., ... & Yang, M. (2015). U–Pb age and Hf isotopic data of detrital zircons from the Devonian and Carboniferous sandstones in Yimin area, NE China: new evidences to the collision timing between the Xing'an and Erguna blocks in the eastern segment of Central Asian Orogenic Belt. *Journal of Asian Earth Sciences*, *97*, 211-228.

Hounslow, M. W., & Balabanov, Y. P. (2018). A geomagnetic polarity timescale for the Permian, calibrated to stage boundaries. *Geological Society, London, Special Publications*, *450*(1), 61-103.

Hounslow, M.W., Harris, S.E., Wójcik, K., Nawrocki, J., Ratcliffe, K.T., Woodcock, N.H., & Montgomery, P. (2021). A geomagnetic polarity stratigraphy for the Middle and Upper Ordovician. Palaeogeography, Palaeoclimatology, Palaeoecology, 567, 110225.

Hounslow, M. W. (2022). A geomagnetic polarity timescale for the Carboniferous. *Geological Society, London, Special Publications*, *512*(1), 141-195.

Huang, B. C., Otofuji, Y., & Yang, Z. Y. (1999). Paleomagnetic constraints on the tectonic relationship between the Alashan/Hexi Corridor terrane and the North China Block. *Geophysical Research Letters*, *26*(6), 787-790.

Huang, B., Otofuji, Y. I., Zhu, R., Shi, R., & Wang, Y. (2001). Paleomagnetism of Carboniferous sediments in the Hexi corridor: its origin and tectonic implications. *Earth and Planetary Science Letters*, *194*(1-2), 135-149.

Huang, B., Shi, R., Wang, Y., & Zhu, R. (2005). Palaeomagnetic investigation on Early-Middle Triassic sediments of the North China block: a new Early Triassic palaeopole and its tectonic implications. *Geophysical Journal International*, *160*(1), 101-113.

Huang, B., Yan, Y., Piper, J.D., Zhang, D., Yi, Z., Yu, S., Zhou, T. (2018). Paleomagnetic constraints on the paleogeography of the East Asian blocks during Late Paleozoic and Early Mesozoic times. Earth-Science Reviews, 186, 8-36.

Ji, Z., Zhang, Z., Yang, J., Chen, Y., & Tang, J. (2020). Carboniferous–Early Permian sedimentary rocks from the north-eastern Erenhot, North China: Implications on the tectono-sedimentary evolution of the south-eastern Central Asian Orogenic Belt. *Geological Journal*, *55*(3), 2383-2401.

Jiang, G., Shi, X., Zhang, S., Wang, Y., & Xiao, S. (2011). Stratigraphy and paleogeography of the Ediacaran Doushantuo Formation (ca. 635–551 Ma) in south China. *Gondwana Research*, *19*(4), 831-849.

Jiang, G., Wang, X., Shi, X., Xiao, S., Zhang, S., & Dong, J. (2012). The origin of decoupled carbonate and organic carbon isotope signatures in the early Cambrian (ca. 542–520 Ma) Yangtze platform. *Earth and Planetary Science Letters*, *317*, 96-110.

Jiang, Y. D., Schulmann, K., Kröner, A., Sun, M., Lexa, O., Janoušek, V., ... & Hanžl, P. (2017). Neoproterozoic-early Paleozoic peri-Pacific accretionary evolution of the Mongolian collage system: Insights from geochemical and U-Pb zircon data from the Ordovician sedimentary wedge in the Mongolian Altai. *Tectonics*, *36*(11), 2305-2331.

Jin, C., Liu, L., Hao, G., & Cao, K. (2015). Sandstone bodies sedimentary characteristics of Shanxi formation, at Chengjiazhuang section in Liulin, Shanxi province, China. *World Journal of Engineering*.

King, R. F. (1955). The remanent magnetism of artificially deposited sediments. Geophysical Supplements to the Monthly Notices of the Royal Astronomical Society, 7(3), 115-134.

Kirschvink, J. (1980). The least-squares line and plane and the analysis of palaeomagnetic data. Geophysical Journal International, 62(3), 699-718.

Kirschvink, J. L., Ripperdan, R. L., & Evans, D. A. (1997). Evidence for a large-scale reorganization of Early Cambrian continental masses by inertial interchange true polar wander. *Science*, *277*(5325), 541-545.

Kovalenko, D. V., & Chernov, E. E. (2008). Paleomagnetism of Carboniferous-Permian and early Jurassic geological complexes in Mongolia. Izvestiya, Physics of the Solid Earth, 44(5), 427-441.

Kravchinsky V.A. (2015) Geomagnetism. In: Jack Rink W., Thompson J.W. (eds) Encyclopedia of Scientific Dating Methods. Encyclopedia of Earth Sciences Series. Springer, Dordrecht.

Kravchinsky, V.A., Konstantinov, K.M. & Cogné, J.P. (2001). Palaeomagnetic study of Vendian and Early Cambrian rocks of South Siberia and Central Mongolia: was the Siberian platform assembled at this time? *Precambrian Research*, *110*(1-4), 61-92.

Kusky, T. M., Polat, A., Windley, B. F., Burke, K. C., Dewey, J. F., Kidd, W. S. F., ... & Peng, H. T. (2016). Insights into the tectonic evolution of the North China Craton through comparative 106 tectonic analysis: A record of outward growth of Precambrian continents. Earth-Science Reviews, 162, 387-432.

Li, B., Wen, X., & Li, G. (1999). High-resolution sequence stratigraphy analysis on the Permo-Carboniferous in north China platform. Earth Science Frontiers, 6, 81-94.

Li, Q. W., & Zhao, J. H. (2020). Amalgamation between the Yangtze and Cathaysia blocks in South China: Evidence from the ophiolite geochemistry. Precambrian Research, 350, 105893.

Li, S., Li, X., Wang, G., Liu, Y., Wang, Z., Wang, T., ... & Yu, S. (2019). Global Meso-Neoproterozoic plate reconstruction and formation mechanism for Precambrian basins: Constraints from three cratons in China. *Earth-Science Reviews*, *198*, 102946.

Li, X. H., Li, Z. X., & Li, W. X. (2014). Detrital zircon U–Pb age and Hf isotope constraints on the generation and reworking of Precambrian continental crust in the Cathaysia Block, South China: a synthesis. *Gondwana Research*, *25*(3), 1202-1215.

Li, Y., Yang, J., Xia, Z., & Mo, D. (1998). Tectonic geomorphology in the Shanxi graben system, northern China. *Geomorphology*, *23*(1), 77-89.

Li, Z. X., Bogdanova, S., Collins, A. S., Davidson, A., De Waele, B., Ernst, R. E., ... & Vernikovsky, V. (2008). Assembly, configuration, and break-up history of Rodinia: a synthesis. *Precambrian Research*, *160*(1-2), 179-210.

Li, Z. X., Li, X. H., Li, W. X., & Ding, S. (2008). Was Cathaysia part of Proterozoic Laurentia? – new data from Hainan Island, south China. *Terra Nova*, *20*(2), 154-164.

Lin, W., Shao, J., & Zhao, Z. (1984). Paleomagnetic features of Sino-Korea plate in Late Paleozoic Era [J]. *Geophysical and Geochemical Exploration*, *5*.

Liu, G. (1990). Permo-Carboniferous paleogeography and coal accumulation and their tectonic control in the North and South China continental plates. *International Journal of Coal Geology*, *16*(1-3), 73-117.

Lu, L., Qin, Y., Zhang, K. J., Han, C. Y., Wei, T., Li, Z. F., & Qu, Z. H. (2020). Provenance and tectonic settings of the Late Paleozoic sandstones in central Inner Mongolia, NE China: constraints

on the evolution of the southeastern Central Asian Orogenic Belt. *Gondwana Research*, *77*, 111-135.

Lv, D., & Chen, J. (2014). Depositional environments and sequence stratigraphy of the Late Carboniferous− Early Permian coal-bearing successions (Shandong Province, China): Sequence development in an epicontinental basin. *Journal of Asian Earth Sciences*, *79*, 16-30.

Lysak, B, (2020). Magnetic survey forward modelling and paleomagnetic reconstruction of the South China Block in the Ediacaran. University of Alberta, Canada.

Ma, X., Xing, L., Yang, Z., Xu, S., & Zhang J. (1993). Paleomagnetic study since late Paleozoic in the Ordos Basin. *Dìqiú wùlixué bào*, *36*(1), 68-79.

Ma, Y., Liu, Y., Wang, Y., Tang, Z., Qian, C., Qin, T., ... & Zang, Y. (2019). Geochronology and geochemistry of the Carboniferous felsic rocks in the central Great Xing'an Range, NE China: Implications for the amalgamation history of Xing'an and Songliao–Xilinhot blocks. *Geological Journal*, *54*(1), 482-513.

Macouin, M., Besse, J., Ader, M., Gilder, S., Yang, Z., Sun, Z., & Agrinier, P. (2004). Combined paleomagnetic and isotopic data from the Doushantuo carbonates, South China: implications for the “snowball Earth” hypothesis. *Earth and Planetary Science Letters*, *224*(3-4), 387-398.

Mao, Q., Xiao, W., Windley, B. F., Han, C., Qu, J., Ao, S., ... & Guo, Q. (2012). The Liuyuan complex in the Beishan, NW China: a Carboniferous–Permian ophiolitic fore-arc sliver in the southern Altaids. *Geological Magazine*, *149*(3), 483-506.

McElhinny, M. W. (1964). Statistical significance of the fold test in palaeomagnetism. Geophysical Journal International, 8(3), 338-340.

McFadden, P. L. (1990). A new fold test for palaeomagnetic studies. Geophysical Journal International, 103(1), 163-169.

McFadden, P. L., & McElhinny, M. W. (1988). The combined analysis of remagnetization circles and direct observations in palaeomagnetism. *Earth and Planetary Science Letters*, *87*(1-2), 161-172.

McFadden, P. L., & McElhinny, M. W. (1990). Classification of the reversal test in palaeomagnetism. *Geophysical Journal International*, *103*(3), 725-729.

Meert, J. G. (2014). Ediacaran–Early Ordovician paleomagnetism of Baltica: a review. Gondwana Research, 25(1), 159-169.

Meert, J. (2019). Incredible India: High-Resolution Proterozoic Paleogeography through integrated studies of mafic dykes.

Meert, J. G., Pivarunas, A. F., Evans, D. A., Pisarevsky, S. A., Pesonen, L. J., Li, Z. X., ... & Salminen, J. M. (2020). The magnificent seven: a proposal for modest revision of the quality index. *Tectonophysics*, *790*, 228549.

Meert, J. G., & Tamrat, E. (2004). The HOG hypothesis for explaining rapid continental motion in the late Neoproterozoic. *The Precambrian Earth: Tempos and Events. Elsevier*.

Mitchell, R. N., Evans, D. A., & Kilian, T. M. (2010). Rapid early Cambrian rotation of Gondwana. *Geology*, *38*(8), 755-758.

Müller, R. D., Seton, M., Zahirovic, S., Williams, S. E., Matthews, K. J., Wright, N. M., ... & Cannon, J. (2016). Ocean basin evolution and global-scale plate reorganization events since Pangea breakup. *Annual Review of Earth and Planetary Sciences*, *44*, 107-138.

Och, L. M., Cremonese, L., Shields-Zhou, G. A., Poulton, S. W., Struck, U., Ling, H., ... & Zhu, M. (2016). Palaeoceanographic controls on spatial redox distribution over the Yangtze Platform during the Ediacaran–Cambrian transition. *Sedimentology*, *63*(2), 378-410.

Özdemir, Ö., & Dunlop, D. J. (2014). Hysteresis and coercivity of hematite. *Journal of Geophysical Research: Solid Earth*, *119*(4), 2582-2594.

Pan, G., Wang, L., Li, R., Yuan, S., Ji, W., Yin, F., ... & Wang, B. (2012). Tectonic evolution of the Qinghai-Tibet plateau. *Journal of Asian Earth Sciences*, *53*, 3-14.

Pavlov, V.E., Pasenko, A.M., Shatsillo, A.V., Powerman, V.I., Shcherbakova, V.V. & Malyshev, S.V., 2018. Systematics of Early Cambrian paleomagnetic directions from the northern and eastern regions of the Siberian Platform and the problem of an anomalous geomagnetic field in the time vicinity of the Proterozoic–Phanerozoic boundary. *Izvestiya, Physics of the Solid Earth*, *54*(5), 782-805.

Pei, J., Sun, Z., Liu, J., Liu, J., Wang, X., Yang, Z., ... & Li, H. (2011). A paleomagnetic study from the Late Jurassic volcanics (155 Ma), North China: implications for the width of Mongol–Okhotsk Ocean. *Tectonophysics*, *510*(3-4), 370-380.

Ren, Q., Zhang, S., Wu, H., Liang, Z., Miao, X., Zhao, H., ... & Davis, G. A. (2016). Further paleomagnetic results from the~ 155 Ma Tiaojishan Formation, Yanshan Belt, North China, and their implications for the tectonic evolution of the Mongol–Okhotsk suture. *Gondwana Research*, *35*, 180-191.

Ren, Q., Zhang, S., Gao, Y., Zhao, H., Wu, H., Yang, T., & Li, H. (2020). New middle-late Permian paleomagnetic and geochronological results from Inner Mongolia and their paleogeographic implications. *Journal of Geophysical Research: Solid Earth*, *125*(7), e2019JB019114.

Ren, Q., Zhang, S., Sukhbaatar, T., Zhao, H., Wu, H., Yang, T., ... & Jin, X. (2021). Did the Boreal Realm extend into the equatorial region? New paleomagnetic evidence from the Tuva–Mongol and Amuria blocks. *Earth and Planetary Science Letters*, *576*, 117246.

Roberts, A. P., Cui, Y., & Verosub, K. L. (1995). Wasp-waisted hysteresis loops: Mineral magnetic characteristics and discrimination of components in mixed magnetic systems. *Journal of Geophysical Research: Solid Earth*, *100*(B9), 17909-17924.

Şengör, A. C., Natal'in, B. A., Sunal, G., & van der Voo, R. (2018). The tectonics of the Altaids: crustal growth during the construction of the continental lithosphere of Central Asia between~ 750 and~ 130 Ma ago. *Annual Review of Earth and Planetary Sciences*, *46*, 439-494.

Shao, L., Wang, X., Wang, D., Li, M., Wang, S., Li, Y., ... & Gao, D. (2020). Sequence stratigraphy, paleogeography, and coal accumulation regularity of major coal-accumulating periods in China. International Journal of Coal Science & Technology, 7(2), 240-262.

Shatsillo, A.V., Rud'ko, S.V., Latysheva, I.V., Rud'ko, D.V., Fedyukin, I.V., Powerman, V.I. & Kuznetsov, N.B. (2020). A Devious Equatorial Dipole Hypothesis: on the Low-Latitude Glaciations Problem and Geomagnetic Field Configuration in Late Precambrian. *Izvestiya, Physics of the Solid Earth*, *56*(6), 833-853.

Shen B H, Shen S Z, Hou Z S, Wu Q, Zhang S C, Zhang B, Zhang Y C, Yuan D X. 2021. Lithostratigraphic subdivision and correlation of the Permian in China. Journal of Stratigraphy, 45(3): 319-339. DOI: 10.19839/j.cnki.dcxzz. 2021.0027.

Sláma, J., Košler, J., Condon, D. J., Crowley, J. L., Gerdes, A., Hanchar, J. M., ... & Whitehouse, M. J. (2008). Plešovice zircon—a new natural reference material for U–Pb and Hf isotopic microanalysis. *Chemical Geology*, *249*(1-2), 1-35.

Steiner, M., Li, G., Qian, Y., Zhu, M., & Erdtmann, B. D. (2007). Neoproterozoic to early Cambrian small shelly fossil assemblages and a revised biostratigraphic correlation of the Yangtze Platform (China). *Palaeogeography, Palaeoclimatology, Palaeoecology*, *254*(1-2), 67-99.

Tan, X. D., Liu, C., Fang, D. J., & Xu, T. C. (1995). Palaeomagnetic study of Triassic rocks from the Qinshui basin of Shanxi Province. *Sci. China, Ser. B*, *25*, 755-762.

Tauxe, L., & Kent, D. V. (2004). A simplified statistical model for the geomagnetic field and the detection of shallow bias in paleomagnetic inclinations: was the ancient magnetic field dipolar?

Torsvik, T. H., & Cocks, L. R. M. (2013). Gondwana from top to base in space and time. *Gondwana Research*, *24*(3-4), 999-1030.

Torsvik, T. H., Van der Voo, R., Preeden, U., Mac Niocaill, C., Steinberger, B., Doubrovine, P. V., ... & Cocks, L. R. M. (2012). Phanerozoic polar wander, palaeogeography and dynamics. *Earth-Science Reviews*, *114*(3-4), 325-368.

Van der Voo, R. (1990). The reliability of paleomagnetic data. *Tectonophysics*, *184*(1), 1-9.

Van der Voo, R., van Hinsbergen, D. J., Domeier, M., Spakman, W., & Torsvik, T. H. (2015). Latest Jurassic–earliest Cretaceous closure of the Mongol-Okhotsk Ocean: A paleomagnetic and seismological-tomographic analysis. *Geological Society of America Special Papers*, *513*, 589-606.

Vermeesch, P. (2018). IsoplotR: A free and open toolbox for geochronology. *Geoscience Frontiers*, *9*(5), 1479-1493.

Uno, K., & Huang, B. (2003). Constraints on the Jurassic swing of the apparent polar wander path for the North China Block. *Geophysical Journal International*, *154*(3), 801-810.

Wang, H., Zhu, Y., & Li, W. (2010). Shanxi Formation sedimentary environment analysis in Zhangshuanglou mining area [J]. *Journal of Heilongjiang Institute of Science and Technology*, *2*.

Wang, J., & Li, Z. X. (2003). History of Neoproterozoic rift basins in South China: implications for Rodinia break-up. *Precambrian Research*, *122*(1-4), 141-158.

Wang, J., & Pfefferkorn, H. W. (2013). The Carboniferous–Permian transition on the North China microcontinent—oceanic climate in the tropics. *International Journal of Coal Geology*, *119*, 106-113.

Wang, J. X., Zhang, K. X., Windley, B. F., Song, B. W., Kou, X. H., Wang, S. D., & Wang, L. J. (2020). A mid-Palaeozoic ocean–continent transition in the Mazongshan subduction–accretion complex, Beishan, NW China: new structural, chemical and age data constrain the petrogenesis and tectonic evolution. *Geological Magazine*, *157*(11), 1877-1897.

Wang, K. X., Sun, T., Yu, J. H., & Sun, L. Q. (2020). Provenances of the Ediacaran sedimentary rocks in the Zhuguangshan area and their implications for granitoid-related uranium mineralization in South China. *Ore Geology Reviews*, *124*, 103588.

Wang, M., Zhong, Y. T., He, B., Denyszyn, S. W., Wang, J., & Xu, Y. G. (2020). Geochronology and geochemistry of the fossil-flora-bearing Wuda Tuff in North China Craton and its tectonic implications. *Lithos*, *364*, 105485.

Wang, X., Hu, K., Qie, W., Sheng, Q., Chen, B., Lin, W., ... & Song, J. (2019). Carboniferous integrative stratigraphy and timescale of China. *Science China Earth Sciences*, *62*(1), 135-153.

Wei, R., Gao, Y., Xu, S., Santosh, M., Xin, H., Zhang, Z., ... & Liu, Y. (2018). Carboniferous continental arc in the Hegenshan accretionary belt: Constraints from plutonic complex in central Inner Mongolia. *Lithos*, *308*, 242-261.

Wu, L., & Kravchinsky, V.A., 2014. Derivation of paleolongitude from the geometric parametrization of apparent polar wander path: Implication for absolute plate motion reconstruction. *Geophysical Research Letters*, *41*(13), 4503-4511.

Wu, L., Kravchinsky, V. A., & Potter, D. K. (2017). Apparent polar wander paths of the major Chinese blocks since the Late Paleozoic: Toward restoring the amalgamation history of east Eurasia. *Earth-Science Reviews*, *171*, 492-519.

Wu, H. N., Zhu, R. X., Liu, C., & Chang, C. F. (1990). Paleomagnetic observations in North China Block: From Late Paleozoic to Triassic. Acta Geophysica Sinica, 33, 694-701.

Xia, Y., Xu, X., Niu, Y., & Liu, L. (2018). Neoproterozoic amalgamation between Yangtze and Cathaysia blocks: The magmatism in various tectonic settings and continent-arc-continent collision. *Precambrian Research*, *309*, 56-87.

Xiao, W., Windley, B. F., Hao, J., & Zhai, M. (2003). Accretion leading to collision and the Permian Solonker suture, Inner Mongolia, China: Termination of the central Asian orogenic belt. *Tectonics*, *22*(6).

Xiao, W., Windley, B. F., Han, C., Liu, W., Wan, B., Zhang, J. E., ... & Song, D. (2018). Late Paleozoic to early Triassic multiple roll-back and oroclinal bending of the Mongolia collage in Central Asia. *Earth-Science Reviews*, *186*, 94-128.

Xu, W., Sun, Z., Shi, G. R., Lu, J., Yu, L., Niu, Y., ... & Cao, Y. (2019). First report of coupled Early Permian paleomagnetic and geochronologic data from the Dunhuang block (NW China), and implications for the tectonic evolution of the Paleo-Asian ocean. *Gondwana Research*, *67*, 46-63.

Yao, J., Cawood, P. A., Shu, L., & Zhao, G. (2019). Jiangnan orogen, South China: a~ 970–820 Ma Rodinia margin accretionary belt. *Earth-Science Reviews*, *196*, 102872.

Yao, W. H., Li, Z. X., Li, W. X., Su, L., & Yang, J. H. (2015). Detrital provenance evolution of the Ediacaran–Silurian Nanhua foreland basin, South China. *Gondwana Research*, *28*(4), 1449-1465.

Yang, H., Ge, W. C., Ji, Z., Yu, Q., & Tian, D. X. (2019). Late Carboniferous to early Permian subduction-related intrusive rocks from the Huolongmen region in the Xing'an Block, NE China: new insight into the evolution of the Nenjiang–Heihe suture. *International Geology Review*, *61*(9), 1071-1104.

Yang, J., Cawood, P. A., Montañez, I. P., Condon, D. J., Du, Y., Yan, J. X., ... & Yuan, D. (2020). Enhanced continental weathering and large igneous province induced climate warming at the Permo-Carboniferous transition. Earth and Planetary Science Letters, 534, 116074.

Yang, Z., Ma, X., Besse, J., Courtillot, V., Xing, L., Xu, S., & Zhang, J. (1991). Paleomagnetic results from Triassic sections in the Ordos Basin, north China. *Earth and Planetary Science Letters*, *104*(2-4), 258-277.

Yang, Z., Courtillot, V., Besse, J., Ma, X., Xing, L., Xu, S., & Zhang, J. (1992). Jurassic paleomagnetic constraints on the collision of the North and South China blocks. *Geophysical Research Letters*, *19*(6), 577-580.

Yang, Z., Sun, Z., Yang, T., & Pei, J. (2004). A long connection (750–380 Ma) between South China and Australia: paleomagnetic constraints. *Earth and Planetary Science Letters*, *220*(3-4), 423-434.

Young, A., Flament, N., Maloney, K., Williams, S., Matthews, K., Zahirovic, S., & Müller, R. D. (2019). Global kinematics of tectonic plates and subduction zones since the late Paleozoic Era. *Geoscience Frontiers*, *10*(3), 989-1013.

Yu, G., Guo, Y., & Xie, Y. (2005). Fengfeng Formation Aquiferous Features and Its Significance on Mine Water Control in western Liulin, Shanxi [J]. *Coal Geology of China*, *4*.

Yuan, W., & Yang, Z. (2015). The Alashan Terrane did not amalgamate with North China block by the Late Permian: evidence from Carboniferous and Permian paleomagnetic results. *Journal of Asian Earth Sciences*, *104*, 145-159.

Zhang, G., Guo, A., Wang, Y., Li, S., Dong, Y., Liu, S., ... & Yao, A. (2013). Tectonics of South China continent and its implications. *Science China Earth Sciences*, *56*(11), 1804-1828.

Zhang, B., Zhang, J., Zhang, Y., Zhao, H., Wang, Y., & Nie, F. (2016). Tectonic affinity of the Alxa Block, Northwest China: Constrained by detrital zircon U–Pb ages from the early Paleozoic strata on its southern and eastern margins. *Sedimentary Geology*, *339*, 289-303.

Zhang, D., Huang, B., Zhao, J., Meert, J. G., Zhang, Y., Liang, Y., ... & Zhou, T. (2018). Permian paleogeography of the Eastern CAOB: paleomagnetic constraints from volcanic rocks in central eastern inner Mongolia, NE China. *Journal of Geophysical Research: Solid Earth*, *123*(4), 2559-2582.

Zhang, D., Huang, B., Meert, J. G., Zhao, G., Zhao, J., & Zhao, Q. (2021a). Micro-Blocks in NE Asia Amalgamated Into the Unified Amuria Block by∼ 300 Ma: First Paleomagnetic Evidence From the Songliao Block, NE China. *Journal of Geophysical Research: Solid Earth*, *126*(10), p.e2021JB022881.

Zhang, D., Huang, B., Zhao, G., Meert, J. G., Williams, S., Zhao, J., & Zhou, T. (2021b). Quantifying the Extent of the Paleo-Asian Ocean During the Late Carboniferous to Early Permian. *Geophysical Research Letters*, *48*(15), e2021GL094498.

Zhang, J., Jin, C., Xing, L., He, H. T., Zhao, Y., Xin, Y., ... & Sun, P. (2019). Mineralogy and geochemistry of the coal seam of Shanxi Formation in Guotun mine, Juye coalfield, North China. *Energy Exploration & Exploitation*, *37*(6), 1779-1803.

Zhang, J., Qu, J., Zhang, B., Zhao, H., Niu, P., Zhao, S., ... & Wang, Y. (2020). Mesozoic intraplate deformation of the central North China Craton: Mechanism and tectonic setting. *Journal of Asian Earth Sciences*, *192*, 104269.

Zhang, J., Zhang, B., & Zhao, H. (2016). Timing of amalgamation of the Alxa Block and the North China Block: Constraints based on detrital zircon U–Pb ages and sedimentologic and structural evidence. *Tectonophysics*, *668*, 65-81.

Zhang, Q. R., & Piper, J. D. A. (1997). Palaeomagnetic study of Neoproterozoic glacial rocks of the Yangzi Block: palaeolatitude and configuration of South China in the late Proterozoic Supercontinent. *Precambrian Research*, *85*(3-4), 173-199.

Zhang, S., Evans, D. A., Li, H., Wu, H., Jiang, G., Dong, J., ... & Yang, T. (2013). Paleomagnetism of the late Cryogenian Nantuo Formation and paleogeographic implications for the South China Block. *Journal of Asian Earth Sciences*, *72*, 164-177.

Zhang, S., Li, H., Jiang, G., Evans, D. A., Dong, J., Wu, H., ... & Xiao, Q. (2015). New paleomagnetic results from the Ediacaran Doushantuo Formation in South China and their paleogeographic implications. *Precambrian Research*, *259*, 130-142.

Zhang, Y., Yan, D. P., Gao, J. F., Qiu, L., Ren, M., Zhang, Y., ... & Xu, D. (2021). Fluid-rock interaction of the early Cambrian black shale in the South China Block: Implications for low-temperature mineralisation. *Ore Geology Reviews*, *131*, 104030.

Zhao, C., Qin, K. Z., Song, G. X., & Li, G. M. (2019). Switch of geodynamic setting from the Paleo-Asian Ocean to the Mongol-Okhotsk ocean: evidence from granitoids in the Duobaoshan ore field, Heilongjiang province, northeast China. Lithos, 336, 202-220.

Zhao, G. (2015). Jiangnan Orogen in South China: Developing from divergent double subduction. *Gondwana Research*, *27*(3), 1173-1180.

Zhao, G., Wilde, S. A., Cawood, P. A., & Sun, M. (2001). Archean blocks and their boundaries in the North China Craton: lithological, geochemical, structural and P–T path constraints and tectonic evolution. *Precambrian Research*, *107*(1-2), 45-73.

Zhao, G., Sun, M., Wilde, S. A., & Sanzhong, L. (2005). Late Archean to Paleoproterozoic evolution of the North China Craton: key issues revisited. Precambrian Research, 136(2), 177-202.

Zhao, H., Zhang, J., Qu, J., Zhang, B., Yun, L., Li, J., ... & Nie, F. (2020). Nature of the Eastern Boundary of the Mesozoic Ordos Basin and the Formation of the Lüliangshan Anticline. *The Journal of Geology*, *128*(2), 157-187.

Zhao, X., Coe, R. S., Zhou, Y., Wu, H., & Wang, J. (1990). New paleomagnetic results from northern China: collision and suturing with Siberia and Kazakhstan. *Tectonophysics*, *181*(1-4), 43-81.

Zhao, X., Liu, C., Wang, J., Duan, L., Zhao, Y., Zhang, Q., & Luo, W. (2017). Petrology, geochemistry and Zircon U-Pb Geochronology of the Xiangshan group in the Eastern Hexi Corridor Belt: Implications for provenance and tectonic evolution. *Acta Geologica Sinica-English Edition*, *91*(5), 1680-1703.

Zhen, Y. Y., Zhang, Y., Wang, Z., & Percival, I. G. (2016). Huaiyuan Epeirogeny—shaping Ordovician stratigraphy and sedimentation on the North China Platform. *Palaeogeography, Palaeoclimatology, Palaeoecology*, *448*, 363-370.

Zheng, R., Xiao, W., Li, J., Wu, T., & Zhang, W. (2018). A Silurian-early Devonian slab window in the southern Central Asian Orogenic Belt: Evidence from high-Mg diorites, adakites and granitoids in the western Central Beishan region, NW China. *Journal of Asian Earth Sciences*, *153*, 75-99.

Zhu, M., Zhang, J., & Yang, A. (2007). Integrated Ediacaran (Sinian) chronostratigraphy of South China. *Palaeogeography, Palaeoclimatology, Palaeoecology*, *254*(1-2), 7-61.

Zhu, R., Shao, J. A., Pan, Y., Shi, R., Shi, G., & Li, D. (2002). Paleomagnetic data from Early Cretaceous volcanic rocks of West Liaoning: Evidence for intracontinental rotation. *Chinese Science Bulletin*, *47*(21), 1832-1837.

Zhu, R., Lo, C. H., Shi, R., Pan, Y., Shi, G., & Shao, J. (2004). Is there a precursor to the Cretaceous normal superchron? New paleointensity and age determination from Liaoning province, northeastern China. *Physics of the Earth and Planetary Interiors*, *147*(2-3), 117-126.

# Appendix

Table A1. Pb/U zircon results for the Taiyuan and Shanxi Formations.

| Grain ID | $^{207}Pb/^{206}Pb$ | 2 s | $^{207}Pb/^{235}U$ | 2 s | $^{206}Pb/^{238}U$ | 2 s | r | $^{207}Pb/^{206}Pb$ (Ma) | 2 s | $^{207}Pb/^{235}U$ (Ma) | 2 s | $^{206}Pb/^{238}U$ (Ma) | 2 s | Disc. % |
|---|---|---|---|---|---|---|---|---|---|---|---|---|---|---|
| STJ1801-041 | 0.0526 | 0.0033 | 0.34 | 0.02 | 0.047 | 0.001 | 0.291 | 311 | 138 | 298 | 17 | 296 | 6 | 4.8 |
| STJ1801-057 | 0.0529 | 0.0042 | 0.33 | 0.03 | 0.046 | 0.001 | 0.226 | 323 | 172 | 291 | 21 | 287 | 5 | 12.8 |
| STJ1801-071 | 0.0535 | 0.0030 | 0.36 | 0.02 | 0.049 | 0.001 | 0.320 | 349 | 124 | 312 | 16 | 307 | 6 | 13.8 |
| STJ1801-078 | 0.0519 | 0.0030 | 0.32 | 0.02 | 0.045 | 0.001 | 0.286 | 280 | 129 | 284 | 15 | 285 | 5 | -1.6 |
| STJ1802-083 | 0.0553 | 0.0011 | 0.48 | 0.01 | 0.063 | 0.001 | 0.758 | 425 | 45 | 399 | 10 | 394 | 9 | 7.7 |
| STJ1802-087 | 0.0522 | 0.0091 | 0.38 | 0.07 | 0.052 | 0.002 | 0.219 | 293 | 354 | 324 | 48 | 328 | 12 | -10.6 |
| STJ1802-097 | 0.0514 | 0.0014 | 0.32 | 0.01 | 0.045 | 0.002 | 0.774 | 258 | 63 | 282 | 11 | 284 | 9 | -9.4 |
| STJ1802-100 | 0.0512 | 0.0012 | 0.33 | 0.01 | 0.046 | 0.001 | 0.743 | 249 | 51 | 286 | 8 | 290 | 7 | -14.3 |
| STJ1802-113 | 0.0512 | 0.0094 | 0.32 | 0.06 | 0.045 | 0.002 | 0.225 | 249 | 374 | 281 | 45 | 284 | 12 | -12.5 |

| Grain ID | $^{207}Pb/^{206}Pb$ | 2 s | $^{207}Pb/^{235}U$ | 2 s | $^{206}Pb/^{238}U$ | 2 s | r | $^{207}Pb/^{206}Pb$ (Ma) | 2 s | $^{207}Pb/^{235}U$ (Ma) | 2 s | $^{206}Pb/^{238}U$ (Ma) | 2 s | Disc. % |
|---|---|---|---|---|---|---|---|---|---|---|---|---|---|---|
| STJ1804-002 | 0.0536 | 0.0065 | 0.37 | 0.05 | 0.050 | 0.002 | 0.266 | 353 | 254 | 317 | 34 | 312 | 10 | 13.2 |
| STJ1804-006 | 0.0516 | 0.0064 | 0.34 | 0.04 | 0.048 | 0.002 | 0.277 | 267 | 263 | 299 | 33 | 303 | 11 | -11.9 |
| STJ1804-035 | 0.0517 | 0.0030 | 0.34 | 0.02 | 0.048 | 0.001 | 0.401 | 271 | 130 | 301 | 17 | 304 | 8 | -10.9 |
| STJ1804-055 | 0.0532 | 0.0076 | 0.37 | 0.06 | 0.051 | 0.002 | 0.276 | 336 | 296 | 322 | 40 | 320 | 13 | 5.1 |
| STJ1804-067 | 0.0528 | 0.0044 | 0.35 | 0.03 | 0.048 | 0.001 | 0.332 | 319 | 180 | 304 | 23 | 302 | 9 | 5.6 |
| STJ1804-116 | 0.0528 | 0.0061 | 0.35 | 0.04 | 0.048 | 0.002 | 0.295 | 319 | 244 | 306 | 32 | 305 | 11 | 4.8 |
| STJ1804-120 | 0.0528 | 0.0074 | 0.35 | 0.05 | 0.048 | 0.002 | 0.247 | 319 | 291 | 306 | 38 | 305 | 11 | 4.8 |
| STJ1805-009 | 0.0506 | 0.0068 | 0.34 | 0.05 | 0.048 | 0.002 | 0.266 | 222 | 285 | 295 | 35 | 305 | 11 | -27.3 |
| STJ1805-080 | 0.0513 | 0.0007 | 0.34 | 0.02 | 0.049 | 0.002 | 0.963 | 252 | 32 | 300 | 13 | 307 | 15 | -17.8 |
| STJ1805-084 | 0.0519 | 0.0051 | 0.34 | 0.04 | 0.048 | 0.001 | 0.278 | 280 | 212 | 300 | 26 | 302 | 8 | -7.4 |

| Grain ID | $^{207}Pb/^{206}Pb$ | 2 s | $^{207}Pb/^{235}U$ | 2 s | $^{206}Pb/^{238}U$ | 2 s | r | $^{207}Pb/^{206}Pb$ (Ma) | 2 s | $^{207}Pb/^{235}U$ (Ma) | 2 s | $^{206}Pb/^{238}U$ (Ma) | 2 s | Disc. % |
|---|---|---|---|---|---|---|---|---|---|---|---|---|---|---|
| STJ1806-001 | 0.0515 | 0.0036 | 0.34 | 0.03 | 0.049 | 0.001 | 0.350 | 262 | 155 | 301 | 20 | 306 | 8 | -14.3 |
| STJ1806-006 | 0.0523 | 0.0037 | 0.35 | 0.03 | 0.049 | 0.002 | 0.413 | 298 | 152 | 307 | 20 | 308 | 10 | -3.3 |
| STJ1806-008 | 0.0517 | 0.0029 | 0.36 | 0.02 | 0.051 | 0.001 | 0.449 | 271 | 123 | 313 | 17 | 318 | 9 | -14.8 |
| STJ1806-011 | 0.0529 | 0.0040 | 0.35 | 0.03 | 0.048 | 0.001 | 0.371 | 323 | 165 | 303 | 21 | 300 | 9 | 7.7 |
| STJ1806-013 | 0.0526 | 0.0035 | 0.34 | 0.02 | 0.047 | 0.001 | 0.395 | 311 | 143 | 296 | 18 | 295 | 8 | 5.4 |
| STJ1806-016 | 0.0526 | 0.0031 | 0.34 | 0.02 | 0.047 | 0.001 | 0.425 | 311 | 128 | 300 | 17 | 299 | 8 | 3.9 |
| STJ1806-025 | 0.0528 | 0.0049 | 0.34 | 0.03 | 0.046 | 0.001 | 0.295 | 319 | 199 | 294 | 25 | 291 | 8 | 9.7 |
| STJ1806-026 | 0.0516 | 0.0040 | 0.33 | 0.03 | 0.046 | 0.001 | 0.336 | 267 | 170 | 289 | 21 | 292 | 8 | -8.7 |
| STJ1806-027 | 0.0516 | 0.0039 | 0.34 | 0.03 | 0.048 | 0.001 | 0.347 | 267 | 166 | 297 | 21 | 301 | 8 | -11.3 |
| STJ1806-028 | 0.0532 | 0.0067 | 0.35 | 0.04 | 0.047 | 0.002 | 0.249 | 336 | 262 | 302 | 33 | 298 | 9 | 12.9 |
| STJ1806-037 | 0.0515 | 0.0033 | 0.33 | 0.02 | 0.046 | 0.001 | 0.376 | 262 | 139 | 289 | 17 | 292 | 7 | -10.3 |

| Grain ID | $^{207}Pb/^{206}Pb$ | 2 s | $^{207}Pb/^{235}U$ | 2 s | $^{206}Pb/^{238}U$ | 2 s | r | $^{207}Pb/^{206}Pb$ (Ma) | 2 s | $^{207}Pb/^{235}U$ (Ma) | 2 s | $^{206}Pb/^{238}U$ (Ma) | 2 s | Disc. % |
|---|---|---|---|---|---|---|---|---|---|---|---|---|---|---|
| STJ1806-039 | 0.0522 | 0.0075 | 0.34 | 0.05 | 0.047 | 0.002 | 0.256 | 293 | 298 | 294 | 37 | 294 | 11 | -0.4 |
| STJ1806-046 | 0.0530 | 0.0032 | 0.35 | 0.02 | 0.048 | 0.001 | 0.392 | 328 | 131 | 307 | 17 | 304 | 8 | 7.9 |
| STJ1806-049 | 0.0519 | 0.0053 | 0.34 | 0.04 | 0.048 | 0.002 | 0.299 | 280 | 218 | 300 | 27 | 302 | 9 | -7.4 |
| STJ1806-054 | 0.0516 | 0.0048 | 0.33 | 0.03 | 0.047 | 0.001 | 0.315 | 267 | 201 | 291 | 25 | 294 | 9 | -9.2 |
| STJ1806-059 | 0.0527 | 0.0059 | 0.34 | 0.04 | 0.047 | 0.001 | 0.245 | 315 | 236 | 297 | 29 | 295 | 8 | 6.9 |
| STJ1806-064 | 0.0533 | 0.0031 | 0.35 | 0.02 | 0.048 | 0.001 | 0.404 | 341 | 126 | 304 | 17 | 300 | 7 | 13.6 |
| STJ1806-068 | 0.0523 | 0.0057 | 0.34 | 0.04 | 0.047 | 0.001 | 0.273 | 298 | 231 | 295 | 29 | 295 | 9 | 0.9 |
| STJ1806-070 | 0.0514 | 0.0037 | 0.33 | 0.03 | 0.046 | 0.001 | 0.344 | 258 | 159 | 288 | 19 | 291 | 8 | -11.6 |
| STJ1806-071 | 0.0520 | 0.0039 | 0.33 | 0.03 | 0.046 | 0.001 | 0.332 | 284 | 165 | 288 | 20 | 289 | 8 | -1.5 |
| STJ1806-074 | 0.0518 | 0.0030 | 0.33 | 0.02 | 0.046 | 0.001 | 0.381 | 276 | 127 | 288 | 16 | 290 | 7 | -5.0 |
| STJ1806-078 | 0.0513 | 0.0060 | 0.33 | 0.04 | 0.046 | 0.001 | 0.257 | 253 | 248 | 288 | 30 | 292 | 9 | -13.2 |

| Grain ID | $^{207}Pb/^{206}Pb$ | 2 s | $^{207}Pb/^{235}U$ | 2 s | $^{206}Pb/^{238}U$ | 2 s | r | $^{207}Pb/^{206}Pb$ (Ma) | 2 s | $^{207}Pb/^{235}U$ (Ma) | 2 s | $^{206}Pb/^{238}U$ (Ma) | 2 s | Disc. % |
|---|---|---|---|---|---|---|---|---|---|---|---|---|---|---|
| STJ1806-079 | 0.0532 | 0.0034 | 0.36 | 0.02 | 0.049 | 0.001 | 0.365 | 336 | 138 | 311 | 18 | 308 | 7 | 9.2 |
| STJ1806-081 | 0.0531 | 0.0035 | 0.35 | 0.02 | 0.047 | 0.001 | 0.372 | 332 | 142 | 302 | 18 | 298 | 8 | 11.2 |
| STJ1806-086 | 0.0525 | 0.0031 | 0.34 | 0.02 | 0.047 | 0.001 | 0.365 | 306 | 129 | 299 | 16 | 298 | 7 | 2.9 |
| STJ1806-087 | 0.0514 | 0.0067 | 0.33 | 0.04 | 0.047 | 0.002 | 0.267 | 258 | 274 | 290 | 33 | 294 | 10 | -12.4 |
| STJ1806-093 | 0.0533 | 0.0041 | 0.35 | 0.03 | 0.047 | 0.001 | 0.337 | 341 | 167 | 302 | 21 | 297 | 8 | 14.9 |
| STJ1806-094 | 0.0520 | 0.0047 | 0.34 | 0.03 | 0.048 | 0.001 | 0.304 | 284 | 195 | 299 | 24 | 300 | 8 | -5.3 |
| STJ1806-095 | 0.0530 | 0.0032 | 0.34 | 0.02 | 0.047 | 0.001 | 0.387 | 328 | 131 | 299 | 17 | 296 | 7 | 10.9 |
| STJ1806-097 | 0.0526 | 0.0038 | 0.34 | 0.03 | 0.047 | 0.001 | 0.351 | 311 | 158 | 298 | 20 | 297 | 8 | 4.7 |
| STJ1806-102 | 0.0515 | 0.0060 | 0.33 | 0.04 | 0.046 | 0.001 | 0.237 | 262 | 247 | 288 | 30 | 292 | 8 | -10.1 |
| STJ1806-103 | 0.0522 | 0.0027 | 0.34 | 0.02 | 0.047 | 0.001 | 0.426 | 293 | 114 | 296 | 15 | 296 | 7 | -1.0 |
| STJ1806-105 | 0.0521 | 0.0042 | 0.34 | 0.03 | 0.047 | 0.001 | 0.319 | 289 | 176 | 296 | 22 | 297 | 8 | -2.9 |

| Grain ID | $^{207}Pb/^{206}Pb$ | 2 s | $^{207}Pb/^{235}U$ | 2 s | $^{206}Pb/^{238}U$ | 2 s | r | $^{207}Pb/^{206}Pb$ (Ma) | 2 s | $^{207}Pb/^{235}U$ (Ma) | 2 s | $^{206}Pb/^{238}U$ (Ma) | 2 s | Disc. % |
|---|---|---|---|---|---|---|---|---|---|---|---|---|---|---|
| STJ1806-106 | 0.0528 | 0.0045 | 0.34 | 0.03 | 0.047 | 0.001 | 0.338 | 319 | 184 | 299 | 23 | 296 | 9 | 7.8 |
| STJ1806-112 | 0.0532 | 0.0037 | 0.34 | 0.03 | 0.047 | 0.001 | 0.358 | 336 | 149 | 301 | 19 | 296 | 8 | 13.6 |
| STJ1806-117 | 0.0526 | 0.0030 | 0.35 | 0.02 | 0.048 | 0.001 | 0.404 | 311 | 125 | 304 | 16 | 303 | 7 | 2.6 |
| STJ1806-119 | 0.0522 | 0.0040 | 0.35 | 0.03 | 0.048 | 0.002 | 0.398 | 293 | 168 | 302 | 22 | 303 | 10 | -3.4 |
| STJ1806-129 | 0.0516 | 0.0036 | 0.34 | 0.03 | 0.048 | 0.001 | 0.352 | 267 | 155 | 296 | 19 | 299 | 8 | -10.9 |
| STJ1807-003 | 0.0528 | 0.0033 | 0.35 | 0.02 | 0.048 | 0.001 | 0.417 | 319 | 137 | 306 | 18 | 305 | 9 | 4.8 |
| STJ1807-061 | 0.0536 | 0.0042 | 0.35 | 0.03 | 0.048 | 0.001 | 0.336 | 353 | 167 | 307 | 22 | 301 | 8 | 17.3 |
| STJ1807-087 | 0.0535 | 0.0050 | 0.35 | 0.03 | 0.048 | 0.001 | 0.309 | 349 | 200 | 305 | 26 | 300 | 9 | 16.4 |
| STJ1807-002 | 0.0512 | 0.0031 | 0.34 | 0.02 | 0.048 | 0.001 | 0.429 | 249 | 134 | 297 | 17 | 303 | 9 | -17.8 |
| STJ1808-003 | 0.0524 | 0.0040 | 0.33 | 0.03 | 0.045 | 0.001 | 0.331 | 302 | 163 | 286 | 20 | 284 | 7 | 6.3 |

| Grain ID | $^{207}Pb/^{206}Pb$ | 2 s | $^{207}Pb/^{235}U$ | 2 s | $^{206}Pb/^{238}U$ | 2 s | r | $^{207}Pb/^{206}Pb$ (Ma) | 2 s | $^{207}Pb/^{235}U$ (Ma) | 2 s | $^{206}Pb/^{238}U$ (Ma) | 2 s | Disc. % |
|---|---|---|---|---|---|---|---|---|---|---|---|---|---|---|
| STJ1808-026 | 0.0522 | 0.0039 | 0.31 | 0.03 | 0.043 | 0.001 | 0.361 | 293 | 164 | 273 | 19 | 271 | 8 | 8.3 |
| STJ1808-045 | 0.0522 | 0.0034 | 0.32 | 0.02 | 0.044 | 0.001 | 0.389 | 293 | 141 | 282 | 17 | 280 | 7 | 4.6 |
| STJ1808-054 | 0.0525 | 0.0062 | 0.31 | 0.04 | 0.043 | 0.001 | 0.265 | 306 | 250 | 273 | 29 | 269 | 9 | 13.9 |
| STJ1808-062 | 0.0515 | 0.0027 | 0.32 | 0.02 | 0.044 | 0.001 | 0.481 | 262 | 115 | 278 | 14 | 280 | 8 | -6.4 |
| STJ1808-064 | 0.0524 | 0.0028 | 0.33 | 0.02 | 0.045 | 0.001 | 0.402 | 302 | 116 | 286 | 14 | 284 | 6 | 6.2 |
| STJ1808-083 | 0.0527 | 0.0025 | 0.32 | 0.02 | 0.044 | 0.001 | 0.443 | 315 | 104 | 280 | 13 | 276 | 6 | 14.1 |
| STJ1808-096 | 0.0523 | 0.0027 | 0.32 | 0.02 | 0.045 | 0.001 | 0.415 | 298 | 113 | 284 | 14 | 283 | 6 | 5.3 |
| STJ1808-110 | 0.0518 | 0.0037 | 0.31 | 0.02 | 0.044 | 0.001 | 0.345 | 276 | 154 | 278 | 18 | 278 | 7 | -0.9 |
| STJ1808-120 | 0.0526 | 0.0039 | 0.32 | 0.03 | 0.045 | 0.001 | 0.344 | 311 | 159 | 285 | 19 | 281 | 7 | 10.4 |
| STJ1808-129 | 0.0523 | 0.0040 | 0.33 | 0.03 | 0.045 | 0.001 | 0.338 | 298 | 164 | 288 | 20 | 286 | 8 | 3.9 |
| STJ1809-035 | 0.0520 | 0.0046 | 0.37 | 0.03 | 0.052 | 0.001 | 0.303 | 284 | 189 | 320 | 25 | 324 | 9 | -12.3 |

| Grain ID | $^{207}Pb/^{206}Pb$ | 2 s | $^{207}Pb/^{235}U$ | 2 s | $^{206}Pb/^{238}U$ | 2 s | r | $^{207}Pb/^{206}Pb$ (Ma) | 2 s | $^{207}Pb/^{235}U$ (Ma) | 2 s | $^{206}Pb/^{238}U$ (Ma) | 2 s | Disc. % |
|---|---|---|---|---|---|---|---|---|---|---|---|---|---|---|
| STJ1809-043 | 0.0528 | 0.0041 | 0.32 | 0.03 | 0.045 | 0.001 | 0.362 | 319 | 167 | 285 | 20 | 281 | 8 | 13.5 |
| STJ1809-068 | 0.0524 | 0.0032 | 0.31 | 0.02 | 0.043 | 0.001 | 0.380 | 302 | 135 | 275 | 16 | 272 | 7 | 11.0 |
| STJ1809-080 | 0.0531 | 0.0041 | 0.38 | 0.03 | 0.052 | 0.002 | 0.432 | 332 | 166 | 325 | 23 | 324 | 12 | 2.4 |